Validation of Breathing Modes in Wind Turbine Blade Finite Element Models

D. Foulds

MSc Thesis

Validation of Breathing Modes in Wind Turbine Blade Finite Element Models

by

D. Foulds

to obtain the degree of Master of Science
at the Delft University of Technology,
to be defended publicly on Friday August 20, 2021 at 9:00 AM.

Student number:	4298152	
Project duration:	February 10, 2020 – August 20, 2021	
Participating institution:	DLR Institute of Aeroelasticity	
Thesis committee:	Prof. Dr. Christos Kassapoglou,	TU Delft
	Dr. ir. John-Alan Pascoe,	TU Delft
	Dr.-Ing. Saullo G. P. Castro,	TU Delft, supervisor
	Dipl.-Ing. Janto Gundlach,	DLR, supervisor
	Dipl.-Ing. Johannes Knebusch,	DLR, supervisor

An electronic version of this thesis is available at `http://repository.tudelft.nl/`.

Preface

This thesis project was conducted with the DLR Institute of Aeroelasticity within the Structural Dynamics and System Identification department as part of my Master's degree program at Delft University of Technology. I would like to thank my supervisors at DLR, Dipl.-Ing. Janto Gundlach and Dipl.-Ing. Johannes Knebusch for their guidance and patience, in addition to the entire department. I would also like to extend my gratitude towards my thesis supervisor Dr.-Ing. Saullo G. P. Castro for his support and valuable insight throughout the project. Finally, to my family and friends thanks for your unconditional support and encouragement during my studies.

D. Foulds
Göttingen, August 2021

Abstract

Wind energy is a growing industry, and in an effort to reduce costs and increase turbine efficiency, rotor blades are becoming increasingly large in size. To facilitate this effort, the SmartBlades2 research project has designed, built, and tested a set of prototype research blades. As part of the SmartBlades2 project, high sensor density modal testing has been conducted on the research blades. The analysis of the modal tests showed good agreement of the global vibration modes with the finite element model predictions. However, the test analysis also identified low frequency vibration modes, referred to as breathing modes, which were not predicted by the finite element models. These vibration modes were found on all of the blades and are characterised by out-of-plane trailing edge panel motion. The objective of this thesis is to identify and predict the aforementioned breathing modes using finite element analysis. To achieve this, three model characteristics are analysed to determine their influence on the breathing mode prediction, namely, model topology, shell element configuration, and material properties.

To characterise the affect of model topology, a cut section from the SmartBlades2 prototype blade is modelled with shell elements and continuum element glue joints. To validate the blade section model, a modal test is conducted which identifies breathing modes analogous to the full blade. Various topology features are investigated with the focus on the shell glue joints and spar web joints of the blade section. The analysis shows that while these changes significantly effect the mode shapes and frequencies, none of them predict the experimentally identified breathing modes.

To investigate the source of this discrepancy, the modal behaviour of a sample plate structure with the same materials is used to remove the variability of topology. The effects of shell element size and configuration are analysed with mutual comparisons. The analysis shows that higher fidelity element configurations offer no advantage over linear shell elements for prediction of modal behaviour, while the element size shows higher sensitivity. Furthermore, the effects of material properties are examined using the sample plate, subject to modal and flexural tests. It is found that the specified properties are stiffer than measured, and new predictions of the properties are made which better fit the plates experimental results.

Finally, the topology, element, and material investigations are then applied to an improved finite element model of the complete blade and correlated with the experimental modal tests. It is found that the improved blade model has closer correlation with the experimental modal tests for global modes, however is unable to predict the identified breathing modes for the blade. It is hypothesised that cause of this may relate to the connection of the spar web with the glue flanges.

Contents

Abstract v

List of Figures ix

List of Tables xiii

Nomenclature xv

1 Introduction 1
  - 1.1 Research Questions and Objectives . . . 2
  - 1.2 Report Layout . . . 2

2 Literature Study 3
  - 2.1 Wind Turbine Blades . . . 3
    - 2.1.1 SmartBlades2 Design . . . 4
    - 2.1.2 Materials . . . 5
    - 2.1.3 Manufacturing . . . 6
    - 2.1.4 Blade Modal Testing . . . 7
    - 2.1.5 Breathing Modes . . . 10
    - 2.1.6 Reference Blade Model . . . 10
  - 2.2 Blade Finite Element Modelling . . . 13
    - 2.2.1 Blade Beam Models . . . 14
    - 2.2.2 Blade Shell Models . . . 14
    - 2.2.3 Glue Joint Models . . . 16
  - 2.3 Experimental Modal Analysis . . . 16
    - 2.3.1 Vibration Testing . . . 16
    - 2.3.2 Modal Parameter Identification . . . 18

3 Model Topology Effects 21
  - 3.1 Blade Section Tests . . . 21
    - 3.1.1 Modal Testing . . . 21
    - 3.1.2 Modal Results . . . 23
  - 3.2 Blade Section Topology . . . 26
    - 3.2.1 Reference Finite Element Model . . . 26
    - 3.2.2 Trailing Edge Core Taper . . . 27
    - 3.2.3 Mesh Refinement . . . 29
    - 3.2.4 Spar Glue Joint Mesh . . . 30
    - 3.2.5 Updated Geometry . . . 32
    - 3.2.6 Boundary Condition Approximation . . . 34
    - 3.2.7 Leading Edge Joint . . . 35
    - 3.2.8 Trailing Edge Joint Length . . . 36
    - 3.2.9 Suction Side Glue Joint . . . 38
    - 3.2.10 Spar Cap Balsa Flanks . . . 39
    - 3.2.11 Spar Web Cable Mass . . . 40
    - 3.2.12 Pressure Side Glue Joint . . . 42
  - 3.3 Blade Section Conclusion . . . 43

4 Model Element and Material Effects 47
  - 4.1 Sample Plate Testing . . . 47
    - 4.1.1 Geometry and Design . . . 47
    - 4.1.2 Modal Tests . . . 49
    - 4.1.3 Modal Results . . . 50

4.1.4 Flexural Stiffness Tests . . . 52
4.1.5 Flexural Stiffness Results . . . 54
4.2 Sample Plate Models . . . 56
4.2.1 Reference Plate Model . . . 56
4.2.2 Shell Element Size . . . 57
4.2.3 Model Element Configuration . . . 59
4.2.4 Adjusted Core Density . . . 61
4.2.5 Rule of Mixtures Properties . . . 63
4.2.6 Flexural Test Model . . . 64
4.2.7 Blade Section Estimated Materials . . . 66
4.2.8 Material Sensitivity Analysis . . . 68
4.2.9 Converged Properties . . . 72

5 Full Blade Analysis 75
5.1 Blade Model Improvements . . . 75
5.1.1 Reference Model Corrections . . . 75
5.1.2 Topology Improvements . . . 76
5.1.3 Material and Element Improvements . . . 78
5.2 Improved Blade Model Analysis . . . 79
5.2.1 Modal Behaviour . . . 79
5.2.2 Breathing Modes . . . 83

6 Conclusions and Recommendations 85

A Composite Laminate Theory 87

Bibliography 89

List of Figures

1.1 Measured 'Breathing' Mode from Clamped-Free Modal Testing 1

2.1 Evolution of Wind Turbine Blade Design [32] 3
2.2 SmartBlades2 Prototype Blade Typical Cross Section [28] 4
2.3 SmartBlades2 Prototype Blade Cross Section 4
2.4 SmartBlades2 Manufacturing Photos 6
2.5 SmartBlades2 Experimental Modal Test Setup 7
2.6 SmartBlades2 Blade Clamped-Free Test Mode Shapes 1-9 8
2.7 SmartBlades2 Modal Test Auto Correlation Plots 9
2.8 SmartBlades2 Blade Free-Free Test Elastic Mode Shapes 1-9 9
2.9 SmartBlades2 Blade Breathing Modes 10
2.10 Full Blade Reference Finite Element Model Features 11
2.11 Full Blade Reference Model Mode Shape Correlation 12
2.12 Full Blade Reference Model Free-Free Eigenmode Frequency Comparison 13
2.13 Full Blade Reference Model Clamped Eigenmode Frequency Comparison 13
2.14 Shear Correction Factors for Isotropic Sandwich Plate [45] 15
2.15 Linear time-invariant system with input $x(t)$, output $y(t)$, impulse response $h(t)$ and frequency response function $H(f)$ [9] 17

3.1 SmartBlades2 Test Section Experiment Setup 22
3.2 Sensor Position and Orientation Diagrams for Blade Section Modal Tests 22
3.3 Blade Section Bungee Test Modal Model Stabilisation Diagram 23
3.4 Blade Section Auto Modal Correlation Plots 23
3.5 Blade Section Shaker Test Modal Model Stabilisation Diagram 24
3.6 Blade Section Shaker Test Identified Mode Shapes 1-9 24
3.7 Blade Section Shaker Test - Bungee Hammer Test MAC Plot 25
3.8 Blade Section Test Article and Finite Element Model Comparison 26
3.9 Blade Section and Finite Element Model Cross-Section View Comparison 26
3.10 Blade Section Reference FE Model Modal Parameter Comparison 27
3.11 Blade Section Trailing Edge Core Taper Comparison 28
3.12 Blade Section Trailing Edge Taper Model Modal Parameter Comparison 28
3.13 Blade Section TE-Taper FE Model - Reference FE Model MAC Matrix 29
3.14 Blade Section Refined Mesh FE Model Comparison (coloured by property) 29
3.15 Blade Section Trailing Edge Taper Model Modal Comparison 30
3.16 Blade Section Refined Mesh - TE-Taper FE Model Modal Correlation 30
3.17 Blade Section Spar Glue Joint Mesh Models 31
3.18 Blade Section Spar Glue Joint Mesh FE Models Shaker Test Mode Shape Correlation 31
3.19 Blade Section Spar Glue Joint Mesh FE Models Eigenmode Frequency Comparison 32
3.20 Blade Section Updated Geometry Model Mesh Comparison 32
3.21 Blade Section Reference and Updated Mesh Geometry Mode Shape Correlation 33
3.22 Blade Section Updated Mesh Geometry Model Comparison 33
3.23 Blade Section 3D scanned surface and updated geometry model 33
3.24 Blade Section Boundary Condition 34
3.25 Blade Section Boundary Condition Model Comparison 34
3.26 Blade Section Leading Edge Joint Comparison 35
3.27 Blade Section Leading Edge Joint FE Model Modal Comparison 35
3.28 Leading Edge Joint FE Model Eigenmode Frequency Comparison 36
3.29 Blade Section Trailing Edge Glue Joint Comparison 36
3.30 Blade Section Trailing Edge Glue Joint Modal Correlation 37

3.31 Trailing Edge Glue Joint FE Model Eigenmode Frequency Comparison . . . 37
3.32 Blade Section Spar Web Suction Side Glue Joint Comparison . . . 38
3.33 Blade Section Suction Side Spar Joint Merge Modal Comparison . . . 38
3.34 Suction Side Spar Joint FE Model Mode Frequency Comparison . . . 39
3.35 Blade Section Spar Cap Balsa Flank Area Comparison . . . 39
3.36 Blade Section Balsa Spar Flanks FE Model Modal Comparison . . . 40
3.37 Balsa Spar Flanks FE Model Eigenmode Frequency Comparison . . . 40
3.38 Blade Section Spar Web Cable Model Comparison . . . 41
3.39 Blade Section Spar Web Cable FE Model Modal Comparison . . . 41
3.40 Spar Web Cable FE Model Eigenmode Frequency Comparison . . . 42
3.41 Blade Section Pressure Side Glue Joint Model Comparison . . . 42
3.42 Blade Section Pressure Side Glue Joint FE Model Modal Comparison . . . 43
3.43 Pressure Side Glue Joint FE Model Eigenmode Frequency Comparison . . . 43
3.44 Blade Section Tip Ballast Chamber (Circled in Red) . . . 44

4.1 Sample Plate Roving Hammer Test Setups . . . 50
4.2 Sample Plate Hammer Tests Auto Modal Correlation . . . 51
4.3 Sample Plate Hammer Tests MAC Matrix . . . 51
4.4 Sample Plate Bungee Hammer Test Identified Mode Shapes 1-9 . . . 52
4.5 Sample Plate Flexural Bending Test Diagrams . . . 53
4.6 Sample Plate Test Coupon with DIC measurement system in three point bending test machine . 54
4.7 Sample Plate Test Coupon Flexural Stiffness Test Force - Displacement Plot . . . 54
4.8 Test Coupon '0 DIR - TS 2' DIC strain fields at maximum load (~237 N) . . . 55
4.9 Sample Plate and Reference FE Model Comparison . . . 56
4.10 Sample Plate Reference FE Model Modal Comparison . . . 56
4.11 Sample Plate *CQUAD4* Finite Element Models for Varying Element Size . . . 57
4.12 Sample Plate *CQUAD4* Element Size Models Mode Frequency Comparison . . . 58
4.13 Sample Plate Mode Shape Correlation for Element Size Models with 10 mm Model . . . 58
4.14 Sample Plate Element Configuration Models . . . 59
4.15 Sample Plate 10 mm Element Configuration Models Mode Frequency Comparison . . . 60
4.16 Sample Plate Mode Shape Correlation for Element Configuration Models with *CQUAD4* 10 mm Model . . . 61
4.17 Sample Plate Adjusted Materials Model Mode Frequency Comparison . . . 62
4.18 Sample Plate Adjusted Materials Model Modal Correlation . . . 62
4.19 Sample Plate Rule of Mixtures Estimate Materials Model Mode Frequency Comparison . . . 63
4.20 Sample Plate Rule of Mixtures Estimated Materials Model Modal Correlation . . . 64
4.21 Three Point Bending Test Finite Element Model . . . 65
4.22 Blade Section Estimated Materials Experimental Correlation Comparison . . . 67
4.23 Blade Section Estimated Materials FE Model Modal Comparison . . . 67
4.24 Sample Plate Bungee Hammer Test Identified Mode Shapes 1-3 . . . 68
4.25 Modal Sensitivity Plot Lamina Moduli Collective Scaling . . . 69
4.26 Modal Sensitivity Plot Independent Lamina Moduli Scaling . . . 69
4.27 Modal Sensitivity Plot Material Coupling Parameter Scaling . . . 70
4.28 Modal Sensitivity Plot Core Shear and Plate Mass . . . 71
4.29 Modal Sensitivity Plot Lamination Parameters . . . 71
4.30 Sample Plate *CQUAD4* 10 mm Converged Materials Mode Frequency Comparison . . . 73
4.31 Sample Plate *CQUAD4* 10 mm Converged Material Model Modal Correlation . . . 73

5.1 Full Blade Finite Element Model Trailing Edge Glue Zones . . . 76
5.2 Full Blade Improved Finite Element Model Features . . . 77
5.3 Improved Blade Model Concentrated Masses for Free-Free and Clamped Modal Tests . . . 78
5.4 Improved Blade Model with Reference Materials - Blade Modal Tests Modal Correlation MAC Matrices . . . 79
5.5 Blade Reference Model - Improved Blade Model with Reference Materials Modal Correlation MAC Matrices . . . 79
5.6 Comparison of Free-Free Test Second Breathing Mode Shape with Improved Model Mode 5 . . . 80

5.7 Comparison of Clamped Test First Breathing Mode Shape with Improved Model Mode 17 81
5.8 Improved Blade Model with Estimated Materials - Blade Modal Tests Modal Correlation MAC Matrices 81
5.9 Improved Blade Model Estimated Materials Variant - Reference Materials Variant Modal Correlation MAC Matrices 82
5.10 Full Blade Identified Eigenmode Frequency Comparison for Free-Free Test Configuration 82
5.11 Full Blade Identified Eigenmode Frequency Comparison for Clamped Test Configuration 82
5.12 Spar Web to Shell Connection Comparison 84

List of Tables

2.1 Material Properties for Glass, Resin, and Adhesive Systems 5
2.2 Non-crimp Glass Fibre Fabric Properties [29] 5
2.3 Blade Reference Data Sheet Laminate Properties [29] 5
2.4 Mass and Centre of Gravity Summary for Prototype Blade [24, 34] 6
2.5 Mass and Centre of Gravity for Prototype Blade from Sections Measurements 7
2.6 Blade Reference Model Laminate Properties [56] 11

3.1 Mass and Centre of Gravity for the SmartBlades2 Blade Section 21
3.2 Mass and Centre of Gravity for Prototype Blade Section 44
3.3 Blade Section Topology Change and Effect Summary 45

4.1 Sample Plate Measured Properties 48
4.2 Sample Plate Mass Properties 48
4.3 Sample Plate Estimated Properties 48
4.4 Sample Plate Rule of Mixtures Estimated Laminate Properties 49
4.5 Sample Plate Foam Hammer Test Modal Parameters 50
4.6 Sample Plate Bungee Hammer Test Modal Parameters 50
4.7 Flexural Stiffness Test Results 54
4.8 Test Coupon ’0 DIR - TS 2’ Measured Strains at maximum load (~237 N) 55
4.9 Sample Plate and Reference Model Mass Comparison 61
4.10 Sample Plate Adjusted Core Density Material Laminate Properties [29] 62
4.11 ’2AX45’ Estimated Material Laminate Property Comparison 64
4.12 ’UD’ Estimated Material Laminate Property Comparison 64
4.13 Experimental Flexural Stiffness Comparison 65
4.14 Experimental Flexural Stiffness Values from 3-Point Bending Test 66
4.15 Blade Rule of Mixtures Estimated Materials Laminate Properties 66
4.16 Sample Plate Converged Material Properties Comparison 72
4.17 Experimental Flexural Stiffness from 3-Point Bending Test Material Model Comparison 74

5.1 Mass and Centre of Gravity Comparison for SmartBlades 2 Prototype Blade Models 78

Nomenclature

Abbreviations

FRF	Frequency Response Function
MAC	Modal Assurance Criterion
SS	Suction Side
PS	Pressure Side
LE	Leading Edge
TE	Trailing Edge
SB2	SmartBlades2
UD	Unidirectional
LSCF	Lest Squares Complex Frequency
FE	Finite Element
ISO	International Organization for Standardization
ERA	Eigensystem realization algorithm
SG	Strain Gauge
DIC	Digital Image Correlation
CLT	Composite Laminate Theory

1

Introduction

Wind power is a growing industry within the European energy market, and in the year 2019 contributed a total of 15% of the EU's total electricity demand [35]. To drive growth in renewable energy production the EU and member state governments are investing into research programs to characterise and develop technologies to build ever larger turbine blades for longer lifespan and higher power output. Among these research projects is the SmartBlades2 project, made up of DLR and a consortium of Universities and Fraunhofer Institute, funded by the Federal Ministry for Economic Affairs and Energy of Germany [1]. One of the major objectives of this project was to design and create a set of prototype blades to investigate the effects of bending/twist coupling. Primarily for the purposes of gust load reduction measured with active monitoring equipment for operational modal identification [1].

To facilitate these objectives of the research project a testing campaign for certification of the blades was performed, consisting of static and fatigue tests as per the GL certification guidelines [17]. Additionally, modal vibration tests were also performed for research purposes. These modal tests were performed with an extensive density of acceleration sensors to obtain high fidelity modal data from the blades for the purposes of model validation [34]. The subsequent analysis of these modal results found several so called 'breathing modes' which were not predicted in either shape or frequency in the corresponding finite element model [34]. The first breathing mode identified during a clamped-free test is shown in Figure 1.1.

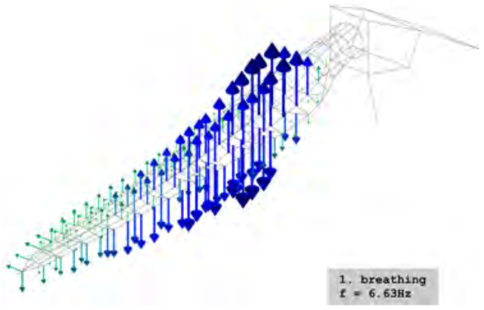

Figure 1.1: Measured 'Breathing' Mode from Clamped-Free Modal Testing

This breathing vibration mode occurs mostly in the trailing edge area of the rotor blade, an area prone to failure in rotor blades [10]. The potential excitation of these breathing modes in operation could have negative effects on the performance of the blade. If excited the shape of the vibration mode could cause cyclic mode 1 type opening stresses on the trailing edge adhesive joint. This may have an effect on fatigue life an warrants further understanding. Furthermore, the excitation of breathing modes in operation may also effect the airfoil shape and thereby reduce the blade efficiency and also cause increased acoustic emissions. To be able to evaluate the impact these vibration modes could have on operational and structural considerations of wind turbine blade design, it must be predicted accurately in rotor blade finite element models. To answer these question within the thesis, research questions and objectives are formulated in Section 1.1.

1.1. Research Questions and Objectives

As shown the discovered breathing modes of the SmartBlades2 rotor blades, may have implications on the performance of the blade and therefore this phenomena needs to be better understood and modelled. Accordingly, the objective of this thesis project is to provide a set of experimentally validated practices to be used in the finite element modelling of wind turbine blades which can accurately predict the breathing eigenmodes. To facilitate this objective a main research question is formulated:

> *How and to what accuracy can 'Breathing', 'Pumping', or 'Panel' type eigenmodes of Wind Turbine Blade Structures be predicted in finite element simulation?*

To answer this research question it is separated into more detailed sub-questions which are individually discussed in the chapters of the thesis:

- What previous research has been conducted on breathing eigenmodes in wind turbine blades?
- What topological features of a wind turbine rotor blade are influential in predicting of breathing eigenmodes?
- What fidelity of finite element structural model is necessary to predict breathing eigenmodes?
- How sensitive are breathing eigenmodes to the materials used laminates used in the wind turbine blade?

1.2. Report Layout

To answer these research questions the thesis is split into several chapters, where each one is addressed:

An examination of previous literature and its relevance to the modelling of wind turbine blade breathing modes is made in Chapter 2. In Section 2.1, the design aspects of wind turbine blades are discussed, focussing on the design of the SmartBlades2 rotor blades. The results and conditions of the modal tests for the SmartBlades2 project are analysed. Previous literature regarding breathing, panel, or pumping type eigenmodes is examined. The reference finite element model used to model the SmartBlades2 research blade is also presented. In Section 2.2 finite element methods and practices used to model wind turbine blades are examined to facilitate model improvement and prediction for the breathing modes. Lastly, in Section 2.3 the methods used for the modal testing of the wind turbine blades are explained. This focusses on test methods and the extraction of frequency response functions. The tools used to extract and identify the eigenmodes from the test data of the structure is explained.

To determine which features of the wind turbine blade effect the prediction of breathing modes a study is undertaken in Chapter 3 where a section of the wind turbine blade is analysed. In Section 3.1 the section of the blade is subject to modal testing such that the effects of the finite element model can be more closely examined at a smaller scale than the full blade. In Section 3.2 the finite element model of the blade section is subject to an iterative improvement process such that the model topology more closely approximates that of the structure. This improvement process focusses on specific features of the blade and how they are implemented into the model and their resulting influence is on the modal behaviour. The results of this analysis is concluded in Section 3.3.

Chapter 4 investigates the influence that finite element configurations and materials properties have on the modal behaviour of shell structure. A fundamental approach is undertaken where a sample plate constructed from the same materials used in the blade is studied. Section 4.1 examines the modal and flexural tests that were made on the plate. Section 4.2 examines the effects of element size and type on the sample plate as well as how the material parameters effect the modal behaviour and how they compare to the experimental testing.

Chapter 5 covers the creation of an improved finite element model of the complete blade using the information and analysis made in Chapters 3 and 4. The exact features used in the model and how they are implemented is explained inSection 5.1. Lastly in Section 5.2 the improved blade model is analysed and compared with the experimental modal test data to identify the probable cause for the breathing modes and their prediction.

Finally, the conclusions of the thesis and recommendations for future work are presented in Chapter 6.

2

Literature Study

In this chapter a literature study is made to examine the relevant topics for modal analysis of wind turbine blade models. First a review of wind turbine blades is made, discussing their evolution, the design of the SmartBlades2 research blades, modal testing of the blades, previous research of breathing modes, and the reference finite element model used for the blade in section 2.1. Strategies for finite element modelling of wind turbine blades are outlined in section 2.2. Lastly methods used for experimental modal analysis, and modal identification are discussed in section 2.3.

2.1. Wind Turbine Blades

Wind turbine blades are an essential part of the wind turbine system facing very demanding requirements as part of government and industry targets to increase the share of renewable energy. This means increasing the span of the blades to improve power output, and increased structural efficiency of the blade to reduce investment cost. An overview of some important design features in wind turbine blade design is presented here to serve as context for the current project.

These strict requirements necessitate advanced light structures with high fatigue life due to the highly cyclic nature of the loading of wind turbine blades. The material most used for this purpose is glass fibre composite due its low cost, high specific stiffness, high fatigue strength, and ease of manufacturing.

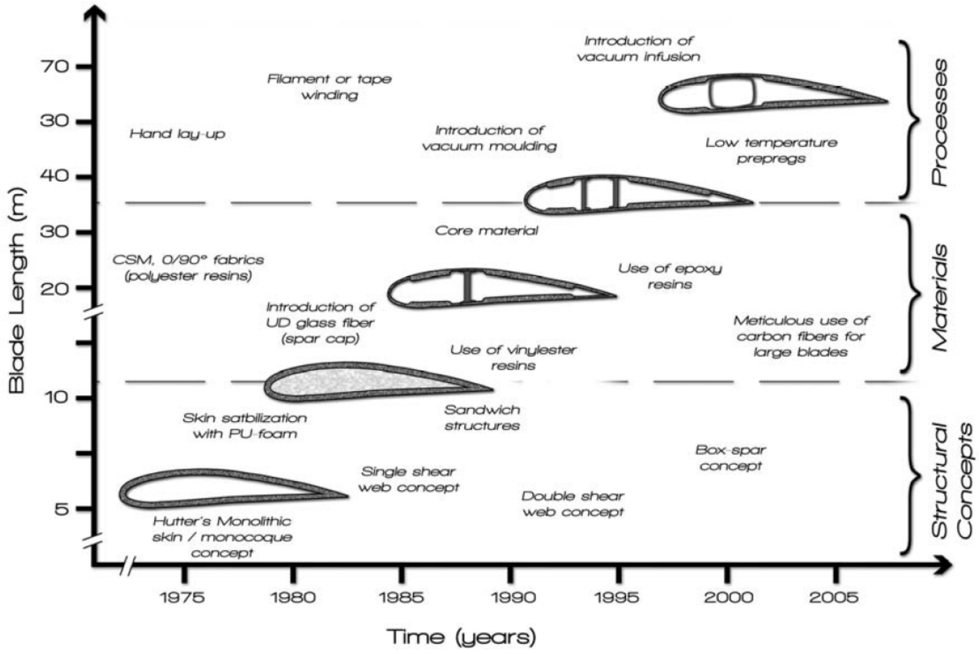
Blade Length (m)
70
30
40
30
20
10
5
Introduction of vacuum infusion
Filament or tape winding
Hand lay-up
Introduction of vacuum moulding
Low temperature prepregs
Processes
Core material
CSM, 0/90° fabrics (polyester resins)
Use of epoxy resins
Introduction of UD glass fiber (spar cap)
Use of vinylester resins
Meticulous use of carbon fibers for large blades
Materials
Skin satbilization with PU-foam
Sandwich structures
Box-spar concept
Single shear web concept
Double shear web concept
Hutter's Monolithic skin / monocoque concept
Structural Concepts
1975
1980
1985
1990
1995
2000
2005
Time (years)

Figure 2.1: Evolution of Wind Turbine Blade Design [32]

In the beginning of modern energy wind turbines, metallic and wood designs were popular based upon aircraft wing designs, however as wind power began to scale in the 1960s and 1970s composite materials were quickly adopted. The evolution of composite wind turbine blades starts from the 1970's using monocoque skin designs stabilised with foam in the internal volume. As blades began to increase in length in the 80s and tip deflection requirements necessitated higher stiffness, single shear web designs with sandwich core panels were adopted. Eventually leading to modern double box spar designs, and most recently incorporating glass and carbon fibre hybrid designs. The design evolution of composite blades is pictured in chart form in Figure 2.1.

2.1.1. SmartBlades2 Design

The focus of this thesis is on the SmartBlades2 project turbine blades created by DLR and a consortium of Academic, and Industry partners. A set of 4 blades were manufactured, a prototype and three for in operation testing. The blade was designed with new technologies, namely a bend-twist coupling to reduce gust loading [28].

The blade is 20 m in span and uses a single spar construction with sandwich panels on the leading and trailing edge. The shells are composed of a leading edge panel, a spar cap, and a trailing edge panel. The spar caps are manufactured from Unidirectional E-glass fibres adjacent to balsa wood flanks to taper thickness to the cores of the panels. The panels are constructed from a combination of balsa wood core near the root and PVC foam core else where with multiple face layers of bi-axial and tri-axial non-crimp E-glass fabric on the panel section. A typical cross section of the blade is depicted in Figure 2.2.

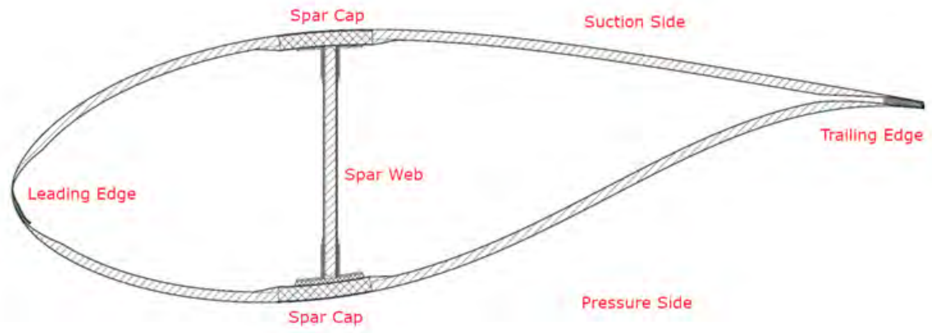

Figure 2.2: SmartBlades2 Prototype Blade Typical Cross Section [28]

The structure is assembled from 3 primary components adhered together, a suction side shell, a pressure side shell, and the spar. The two shells and spar are manufactured via a vacuum infusion process on large moulds of the blade shape. To adhere the components together a combination of adhesive and hand laminated patches are used. The final cross section is visible in Figure 2.3.

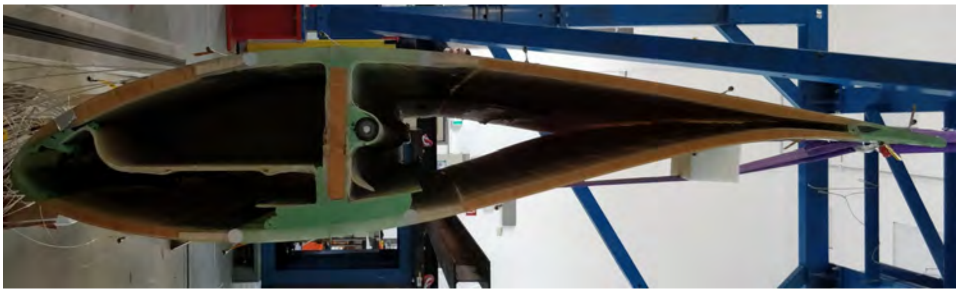

Figure 2.3: SmartBlades2 Prototype Blade Cross Section

It can be seen in Figure 2.3 that there is a thick glue joint at the spar connection of the pressure side. This is due to a manufacturing error in which the mould was manufactured with a deeper shape than design resulting in the spar web being too short. This resulted in an asymmetric glue joint at the spar for the prototype blade with much larger amounts of adhesive.

2.1.2. Materials

The laminates were manufactured from non-crimp fabric sheets of SE 1500 Glass Fibers and Olin AIRSTONE 88x Infusion System (Epoxy resin 880E/ Hardener 886H). The assembly and bonding of the blade sections was made with Sikadur WTG-1280 Adhesive Epoxy System. These comprise the base materials of the blade and their properties are shown in Table 2.1.

Table 2.1: Material Properties for Glass, Resin, and Adhesive Systems

Material	E [MPa]	G [MPa]	ν_{12} [−/−]	ρ [kg/m^3]
SE 1500 Glass Fiber [2]	82000	33750	0.2	2620
AIRSTONE 880E/886H Inf. Resin [46]	3100	1192	0.3	1100
Sikadur WTG-1280/1050 Adhesive [51]	3500	1316	0.33	1300

Four different non-crimp fabric types were used in the blades, mostly in quasi isotropic layups apart from the highly unidirectional spar cap sections. To estimate the mechanical properties if the laminates Chapter 4 each glass fabric's relevant directional and areal masses are listed in Table 2.2.

Table 2.2: Non-crimp Glass Fibre Fabric Properties [29]

Fabric	0° [g/m^2]	90° [g/m^2]	−45° [g/m^2]	+45° [g/m^2]	Thread [g/m^2]	m' [g/m^2]
UD [48]	1134	36	-	-	12	1182
2AX45 [49]	2	-	401	401	6	810
2AX90 [47]	402	432	-	-	6	840
3AX [50]	709	-	242	242	6	1199

The mechanical properties used for finite element simulations are based from the consultant manufacturer estimates and testing [29, 46]. The unidirectional laminates underwent extensive coupon testing as they comprise the majority of the stiffness of the blade, however they were the only laminate to be mechanically tested a priori to the thesis. The consultant manufacturer made estimates of the stiffness properties based upon assumed fibre volume content ratios and the data sheet values using classical laminate theory, although this was never able to be replicated. The properties of the core materials are also estimated from their respective data sheets with resin infused density adjustments for each thickness class. The properties for each of the base laminas are shown in Table 2.3.

Table 2.3: Blade Reference Data Sheet Laminate Properties [29]

Material	Angle	E_1 [MPa]	E_2 [MPa]	G_{12} [MPa]	ν_{12}	V_f	t[mm]	ρ[kg/m^3]
UD	0°	44151	14526	3699	0.3	55%	0.827	1948
2AX45	±45°	11316	11316	11978	0.633	50%	0.625	1875
2AX90	0°/90°	26430	27520	3464	0.124	50%	0.651	1875
3AX	0°/±45°	29873	13377	6918	0.466	50%	0.922	1875
Baltek SB.100 [4]	-	2526	2526	187	0.3	-	19.4	291
C70-55 (dry) [3]	-	-	-	-	-	-	-	60
C70-55-5 mm [3]	-	55	55	22	0.3	-	5	596
C70-55-10 mm	-	55	55	22	0.3	-	10	384
C70-55-15 mm	-	55	55	22	0.3	-	15	314
C70-55-20 mm	-	55	55	22	0.3	-	20	279
C70-55-20 mm (Spar)	-	55	55	22	0.3	-	20	180

2.1.3. Manufacturing

The SmartBlades2 rotor blades used the industry standard methods for manufacturing. A vacuum assisted resin transfer moulding process was performed on the suction and pressure side shells in their moulds. This process is a series of individual infusions where the UD spar cap, base plug, access panels, shell, and bonding edge areas are progressively made into a consolidated component. A similar process is performed on the spar web after which the components can then be assembled.

The assembly process of the web to the shell is complex but is similar to that of the shells. The spar web is progressively laminated onto the inner suction side of the spar cap with laminate enforcement to be consolidated into a single component. It is then prepared for assembly of the two shells via adhesive, the suction side consolidated part is shown in Figure 2.4a. The fitment of the blades showed a large bondline thickness for the shear web. The shells were then assembled in a large bonding operation across the leading and trailing edge as well ass the spar web, the interior of the bonded shells is shown in Figure 2.4b.

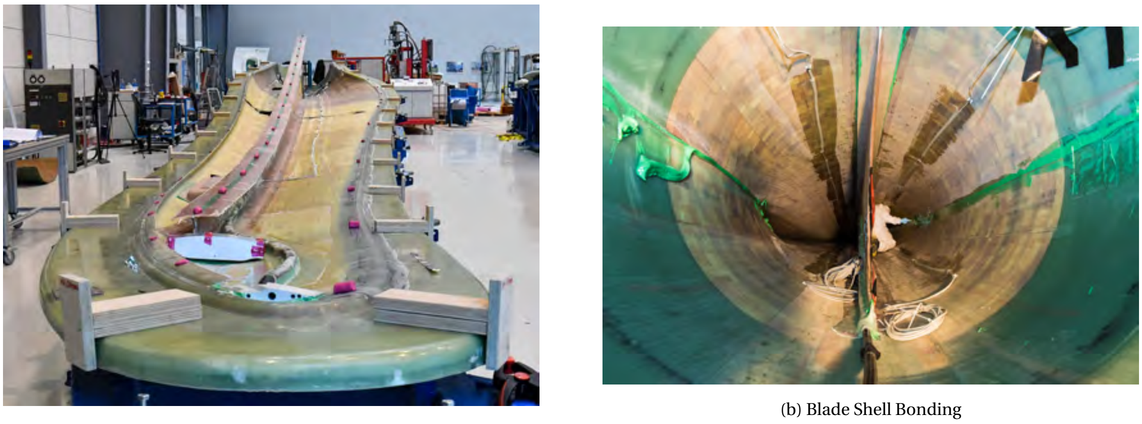

(a) Blade Suction Side Fitment

(b) Blade Shell Bonding

Figure 2.4: SmartBlades2 Manufacturing Photos

After bonding operations the final processing of the blade was performed where excess laminate from the moulds were removed along the parting line. The final step in the manufacturing process is the application of the measurement equipment, rotor hub bolts, and surface coating.

The prototype blade was measured for its mass and centre of gravity in an unfinished state where the excess laminate from the mould had not been removed and the retaining bolts, patch laminates, and coatings had not been applied. The blade was tested experimentally in the free-free condition in this unfinished state. The blade was also tested later in the fixed-free condition where the cross-bolts, and additional hand laminates were applied, with test sensor masses estimated to be 108 kg [24, 34]. The blade mass and centre of gravity was measured in the unfinished state, and the final mass and centre of gravity is estimated for the finished state and fixed-free test conditions. A summary of the mass and centre of gravity for these three configurations is shown in Table 2.4.

Table 2.4: Mass and Centre of Gravity Summary for Prototype Blade [24, 34]

Blade Configuration	Mass [kg]	CoG X [mm]
Blade 1 (Unfinished)	1745.4	6759.0
Blade 1 (Finished)	1793	6580
Blade 1 (w/ Test Sensors)	1901	6960

After testing the prototype blade was cut into multiple sections along the span to verify the shape and span wise mass. These section measurements were used to estimate the centre of gravity with a higher accuracy, however one section of blade from 16.5 m to 17.0 m was unable to be accounted for and thus the mass is less than originally measured. The estimated mass and centre of gravity of complete blade from the section data is shown in Table 2.5.

Table 2.5: Mass and Centre of Gravity for Prototype Blade from Sections Measurements

Mass [kg]	CoG X [mm]	CoG Y [mm]	CoG Z [mm]
1696.9	6278.4	-56.4	142.8

2.1.4. Blade Modal Testing

Following the blade manufacturing, an initial campaign of vibration testing was made on the prototype blade with high sensor density to determine the modal parameters. Two different configurations of the blade were tested, one in a semi-finished state in a free-free condition and one in a clamped condition attached to a test fixture at the root. The clamped test was completed with very high sensor density while the free-free test conducted with fewer sensors. The test procedure followed the general aerospace modal test process detailed by Lubrina et al[36].

Multiple sources of excitations were used, namely both shaker and hammer excitation. Multiple runs of each excitation at different locations were performed to make sure to excite all of the desired modes. From these data sets of frequency response functions the modal parameters were estimated (via. PolyMax method) for each run and the best modes from all runs were compiled into a master modal model. A master modal model for both free-free and clamped conditions was created. The exact parameters of these tests are documented in [24], for the purposes of this thesis only the resulting modal models are examined.

The free-free test was conducted on the manufactured blade in a semi-finished state, where the internal parts had been added but the attachment bolts were not attached. This semi- finished blade was suspended via bungee cable to the gantry above to decouple the rigid body modes of the blade from the elastic modes. The sensor cabling was routed directly off of the blade onto the ground therefore the sensor masses didn't contribute significantly to any added mass effects. The test setup for the free-free configuration is shown in Figure 2.5a.

The clamped test was conducted also in a semi-finished state of the blade with the main difference being that the attachment bolts were included and the mould line trimmings were removed. A key difference with the clamped test was extensive use of cabling for the accelerometers along the blade span, this cabling was estimated to be an additional 108 kg in [24, 34]. To simulate the clamped configuration the blade was bolted into a stiff supporting structure. The clamped configuration test setup is shown in Figure 2.5b.

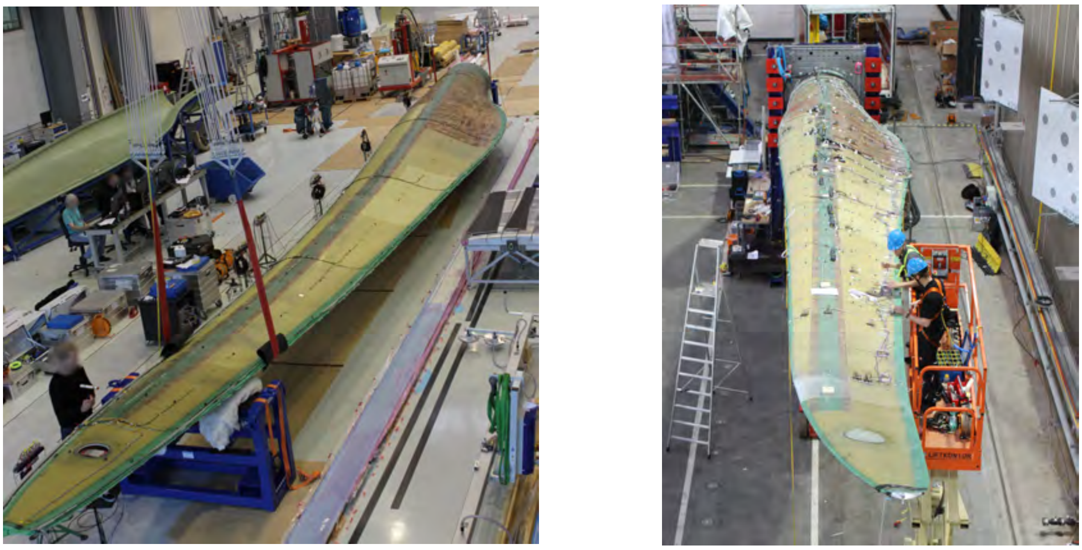

(a) Free-Free Test Configuration

(b) Clamped Test Configuration

Figure 2.5: SmartBlades2 Experimental Modal Test Setup

To assess the quality of the experiment modal models the auto modal correlation plot is examined to identify if the modes are of high quality. First the clamped-free configuration is examined and its autocorrelation plot is shown in Figure 2.7a. The clamped modal model shows a good autocorrelation result with very high mac values along the diagonal. There are some high off diagonal values showing similarity between modes 3-6, 7-8, 11-12, and 13-14. The shapes for the first 9 modes is shown in Figure 2.6. Mode 6 shows a coupled first breathing and second edgewise bending mode resulting in the high off diagonal MAC value. Similarly mode 8 is also coupled mode with second bending edge-wise of mode 7 and second breathing of mode 10. Modes 11-12 are also a result of coupling between first torsion and second breathing, and modes 13-14 between fourth bending flap-wise and a fixture mode. From examination of the modal model for the clamped configuration no spurious modes exist from the testing. However for further comparison with the finite element models, the modes related to the fixture are omitted in the analysis namely modes 5, 14, and 19.

The highest frequency rigid body mode of the free-free test was found to be 1.0 Hz, this is a ratio 1 : 4.8 less than the first elastic mode. [11, 57] state that ideally rigid body modes should be a tenth of the first elastic modes, but in practice a ratio of 1 : 5 is used which matches the conditions for this test. The rigid body modes are not included in the modal model for analysis, the autocorrelation for the free-free test is shown in Figure 2.7a. The autocorrelation shows an identity matrix with only one significant off diagonal correlation for the modes 12-13. These are actually duplicated modes for the fourth bending flap-wise from a testing artefact so do not significantly affect the test results. A notable difference between the free-free and the clamped tests is the reduced amount of mode coupling with the breathing nodes.

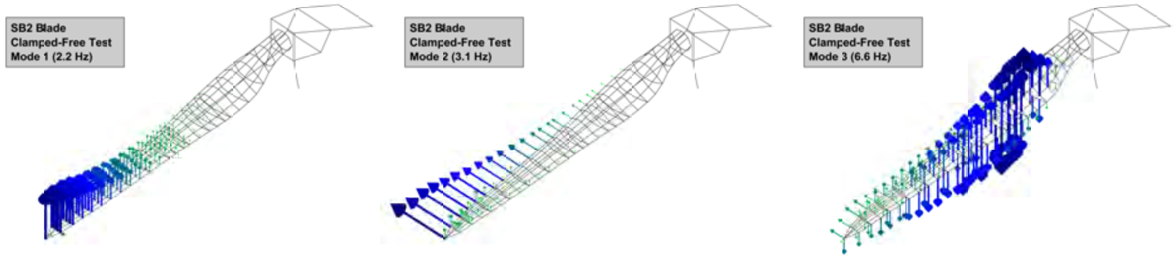
SB2 Blade
Clamped-Free Test
Mode 1 (2.2 Hz)
SB2 Blade
Clamped-Free Test
Mode 2 (3.1 Hz)
SB2 Blade
Clamped-Free Test
Mode 3 (6.6 Hz)

(a) Mode 1: Bending Flap-wise

(b) Mode 2: Bending Edge-wise

(c) Mode 3: First Breathing

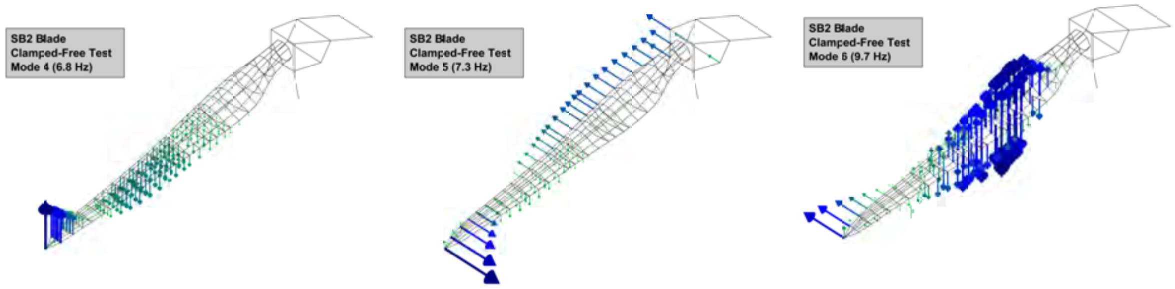
SB2 Blade
Clamped-Free Test
Mode 4 (6.8 Hz)
SB2 Blade
Clamped-Free Test
Mode 5 (7.3 Hz)
SB2 Blade
Clamped-Free Test
Mode 6 (9.7 Hz)

(d) Mode 4: Second Bending Flap-wise

(e) Mode 5: Fixture Edgewise

(f) Mode 6: Second Bending Edge-wise with First Breathing

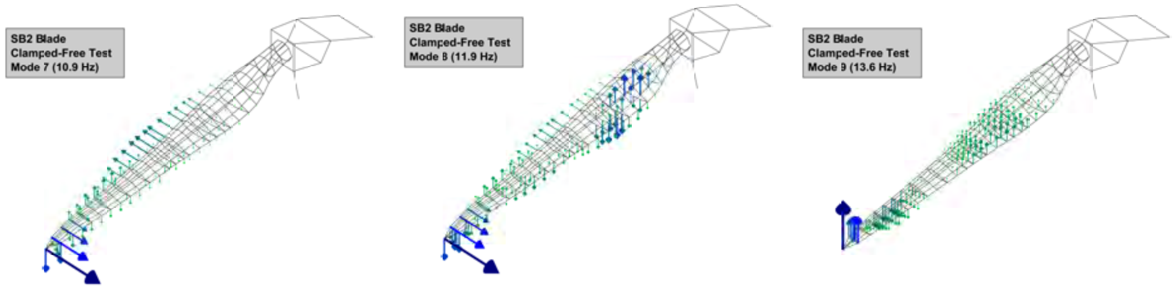
SB2 Blade
Clamped-Free Test
Mode 7 (10.9 Hz)
SB2 Blade
Clamped-Free Test
Mode 8 (11.9 Hz)
SB2 Blade
Clamped-Free Test
Mode 9 (13.6 Hz)

(g) Mode 7: Second Bending Edge-wise

(h) Mode 8: Second Bending Edge-wise with Second Breathing

(i) Mode 9: Third Bending Flap-wise

Figure 2.6: SmartBlades2 Blade Clamped-Free Test Mode Shapes 1-9

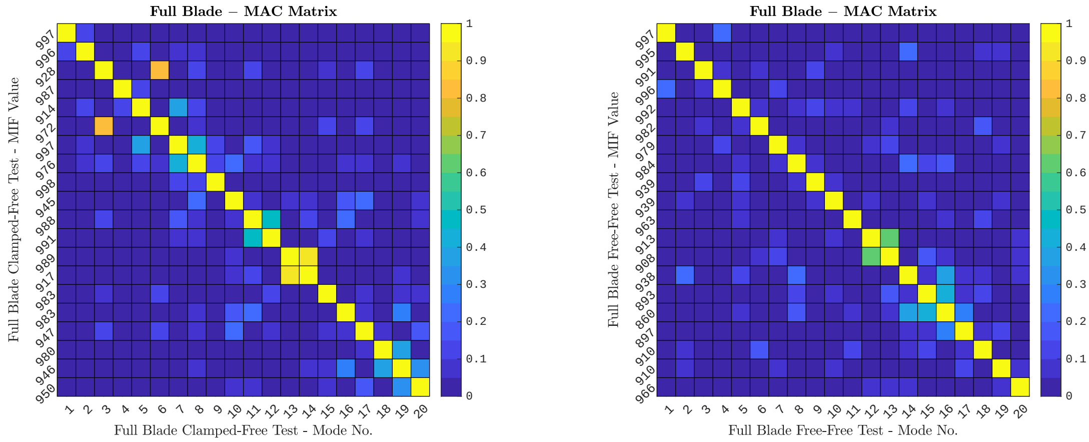

(a) Clamped-Free Modal Model Auto MAC Plot

(b) Free-Free Modal Model Auto MAC Plot

Figure 2.7: SmartBlades2 Modal Test Auto Correlation Plots

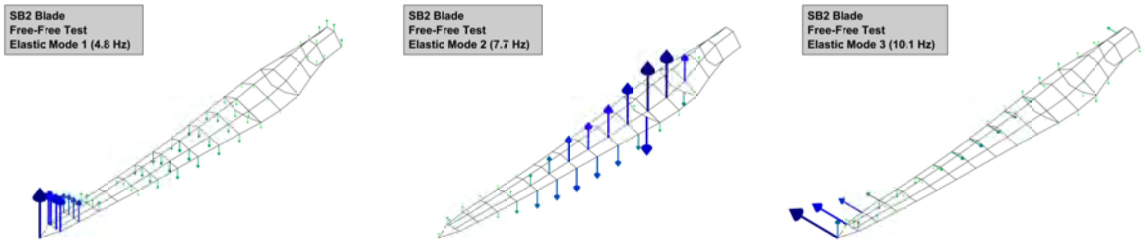
SB2 Blade
Free-Free Test
Elastic Mode 1 (4.8 Hz)
SB2 Blade
Free-Free Test
Elastic Mode 2 (7.7 Hz)
SB2 Blade
Free-Free Test
Elastic Mode 3 (10.1 Hz)

(a) Mode 1: First Bending Flap-wise

(b) Mode 2: First Breathing

(c) Mode 3: First Bending Edge-wise

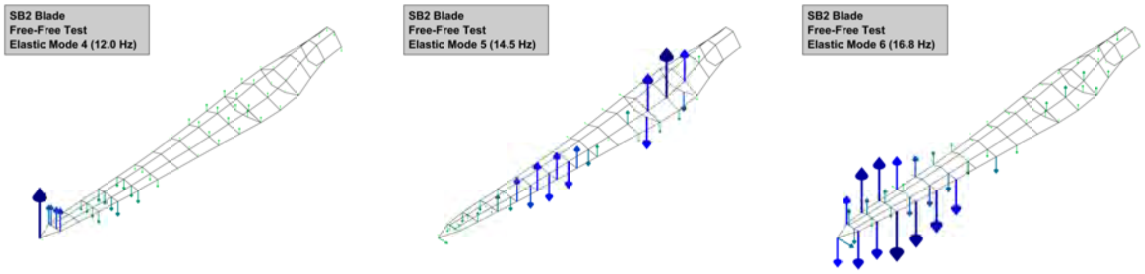
SB2 Blade
Free-Free Test
Elastic Mode 4 (12.0 Hz)
SB2 Blade
Free-Free Test
Elastic Mode 5 (14.5 Hz)
SB2 Blade
Free-Free Test
Elastic Mode 6 (16.8 Hz)

(d) Mode 4: Second Bending Flap-wise

(e) Mode 5: Second Breathing

(f) Mode 6: First Torsion

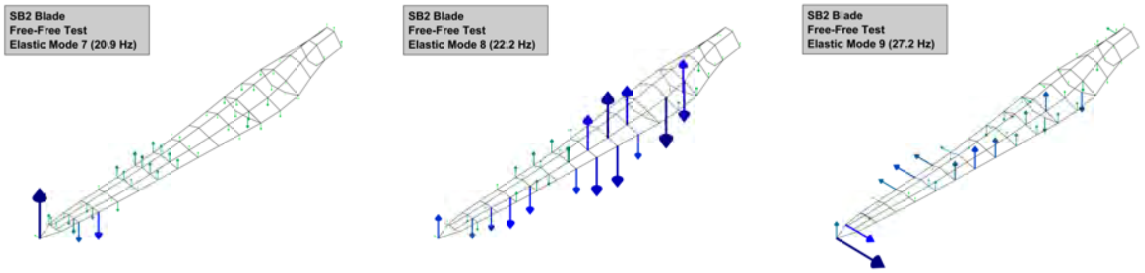
SB2 Blade
Free-Free Test
Elastic Mode 7 (20.9 Hz)
SB2 Blade
Free-Free Test
Elastic Mode 8 (22.2 Hz)
SB2 Blade
Free-Free Test
Elastic Mode 9 (27.2 Hz)

(g) Mode 7: Third Bending Flap-wise

(h) Mode 8: Third Breathing

(i) Mode 9: Second Bending Edge-wise

Figure 2.8: SmartBlades2 Blade Free-Free Test Elastic Mode Shapes 1-9

2.1.5. Breathing Modes

From the modal tests several breathing vibrations modes were observed in both the free-free and clamped configurations. In addition to the testing of the SmartBlades2 prototype blade covered here, further free-free tests were conducted on the other 3 blades and in all three breathing modes were also found [24]. These breathing modes are also known as 'panel' or 'pumping' type modes in wind turbine blades, and they are characterised by out of plane motion of the blade shells on the suction and pressure sides. The modes appear all along the span of the blade but are most dominant in the areas of maximum chord on the trailing edge panels. The first three Breathing modes identified in both the clamped and free-free tests are shown in Figure 2.9.

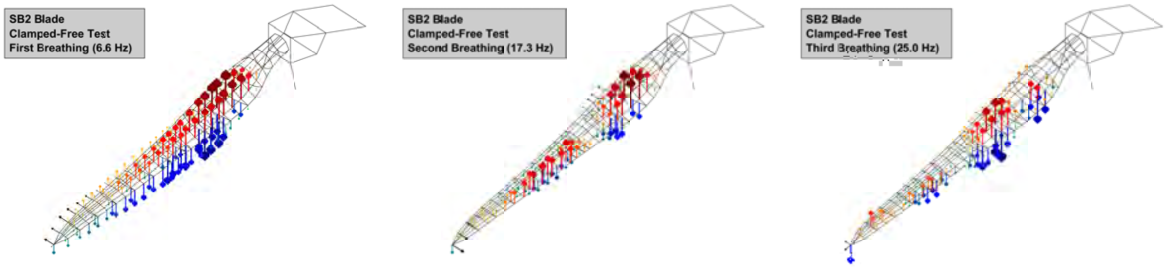

(a) Clamped-Free Test: First Breathing (b) Clamped-Free Test: Second Breathing (c) Clamped-Free Test: Third Breathing

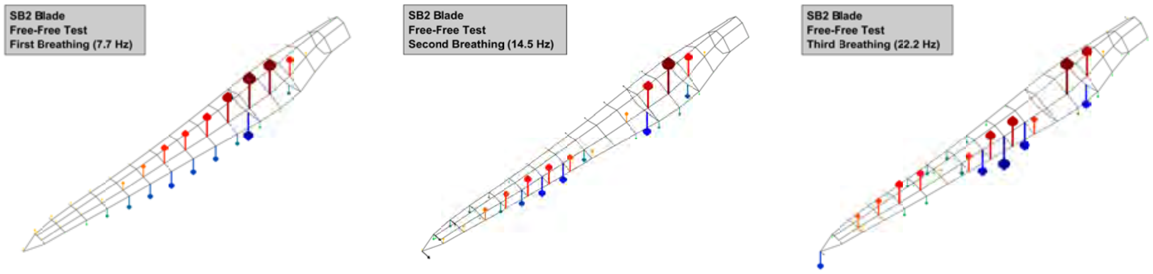

(d) Free-Free Test: First Breathing (e) Free-Free Test: Second Breathing (f) Free-Free Test: Third Breathing

Figure 2.9: SmartBlades2 Blade Breathing Modes

The literature surrounding breathing modes of wind turbines is very scarce as they are only detectable from high fidelity modal testing as shown in the SmartBlades2 test data. Some mention of this phenomena has been made generally in texts [31] stating that at the root transition area out of plane pumping motion can cause excess fatigue at the bonded joints and is a critical area. Fatigue damage to the trailing edge bonded joint is an area of high interest [26, 27]. There is therefore a need to understand better the out of plane breathing motion as it could result in damage to the blades bond lines over time.

Breathing modes have been identified in past experimental research for a smaller scale blade of 8.325 m length at Sandia National Laboratories [21]. Following this they were also able to generate a finite element model and show the panel mode shapes although further details were not provided [19]. This shows that it should be possible to model panel type modes in finite element. However in their research no direct correlations in mode shape or frequency were made between the measurements and the finite element model. Therefore a gap exists in the knowledge which aims to be explored in this thesis. To present a baseline with which to evaluate the model performance in the thesis a reference finite element was made available and is described in Section 2.1.6.

2.1.6. Reference Blade Model

The reference finite element model for the SmartBlades2 research blade was taken from the published model of [56]. This model was created by modelling the blade shells along the wet surface design geometry. The blade was constructed with *CQUAD4* linear type shell elements with inward facing normals and an offset of half the shell thickness. The shell elements were used to model the composite laminates with *PCOMP* properties. The average size of the shell elements across the model is approximately 100 mm. A the full blade reference model is shown in Figure 2.10a.

Three glue joints of the blade were included in the reference full blade model, the spar to shell glue joints on the suction and pressure side shells as well as the trailing edge glue joint. These glue joints are modelled via continuum elements in NASTRAN utilising *CHEXA8* linear elements. For the reference model only 1 element through the glue thickness is used to model these solid joints. The glue joints can be seen in a cross-section of the reference blade model shown in Figure 2.10b.

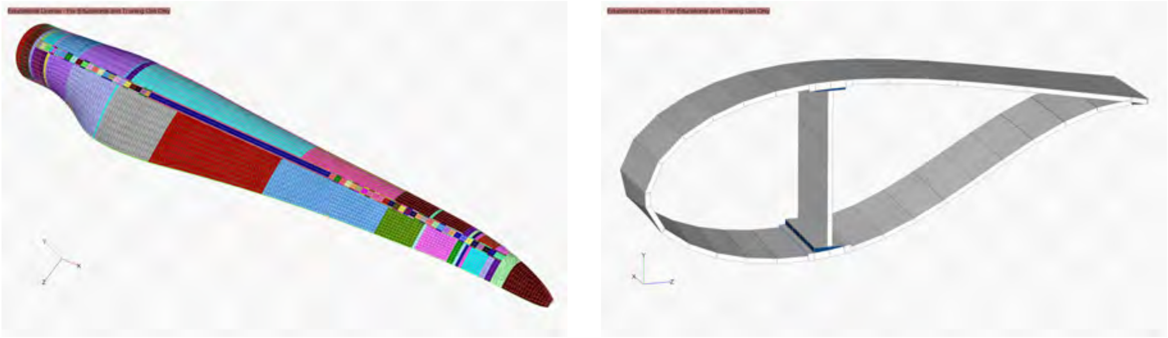
(a) Model Mesh Coloured by Property

(b) Model Cross Section Glue Joints

Figure 2.10: Full Blade Reference Finite Element Model Features

The reference finite element mode does not include any core thickness tapering at the transition zones present in the design. It should also be noted some inconsistencies were present between the published reference model and the reference data sheet material properties in Table 2.3. The material properties used in the reference finite element model are shown in Table 2.6.

Table 2.6: Blade Reference Model Laminate Properties [56]

Material	Angle	E_1 [MPa]	E_2 [MPa]	G_{12} [MPa]	ν_{12}	V_f	t [mm]	ρ [kg/m^3]
UD	0°	44151	14526	3699	0.3	55%	0.88	1948
2AX45	±45°	11316	11316	11978	0.633	50%	0.63	1875
2AX90	0°/90°	26430	27520	3464	0.124	50%	0.66	1875
3AX	0°/±45°	29873	13377	6918	0.466	50%	0.933	1875
Baltek SB.100	-	35	35	110	0.3	-	19.4	291
C70-55-5 mm	-	55	55	18	0.3	-	5	596
C70-55-10 mm	-	55	55	18	0.3	-	10	384
C70-55-15 mm	-	55	55	18	0.3	-	15	314
C70-55-20 mm	-	55	55	18	0.3	-	20	279
C70-55-20 mm (Spar)	-	55	55	18	0.3	-	20	180

If the tables of materials are examined the reference model the laminates have the same material stiffness, however the thickness in the model is slightly higher than the specified values from the data sheet. The other major difference is the stiffness of the balsa core material 'Baltek SB.100' where the model shows significantly lower values than the data sheet. These lower properties are consistent with the minimum balsa stiffness for certification in [17]. These properties are conventionally used during load deflection or buckling analysis to predict the worst case, however for the purpose of a modal analysis it considerably underestimates the stiffness. The foam core shear stiffness is also slightly lower with the densities of all materials the same. However for the purposes of a reference comparison these inconsistencies are left unchanged.

The reference blade model is subjected to a modal analysis to compare with the experimentally determined modal parameters. Two configurations of the blade are examined, a Free-Free test to compare with the first modal test of the blade where no boundary conditions are applied. The second configuration consists of the clamped condition to replicate the second modal test, all degrees of freedom at the blade root are fixed.

To quantify the differences in mode shape between the experimentally determined modal models and the results of the finite element model the Modal Assurance Criterion (MAC) is used. This is calculated by identifying the finite element nodes closest to the experimental geometry measurement points and selecting the similar degree(s) of freedom between them. To ensure the measurement and model degrees of freedom are similar, they must be defined within the same reference system or be rotated to match in post processing. Using this common set of nodes and measurement points, the eigenmode vectors are then assembled from the two modal models and compared using a normalised dot product to calculate the MAC value between two specific mode vectors. The MAC calculation from the eigenmode vectors is shown in Equation (2.1) taken from [39], where ϕ_1 represents an eigenvector of the reference set, and ϕ_2 represents an eigenvector of the comparison set.

$$MAC(\phi_1, \phi_2) = \frac{\left|{\phi_1}^T \cdot \phi_2\right|^2}{\left({\phi_1}^T \cdot \phi_1\right)\left({\phi_2}^T \cdot \phi_2\right)} \tag{2.1}$$

A modal assurance criterion value of unity represents identical eigenmode shape vectors, alternatively a value of zero represents orthogonality of the eigenmode shapes. To correlate the mode shapes between the experimental and finite element modal models the MAC values are calculated for every sets of modes. This takes the form a MAC Matrix where the MAC values for every mode pair are correlated and identified to allow for comparison. The mode shapes are correlated between the experiment and reference finite element model for both clamped and free-free configurations, the MAC matrix plots are shown in Figures 2.11a and 2.11b respectively.

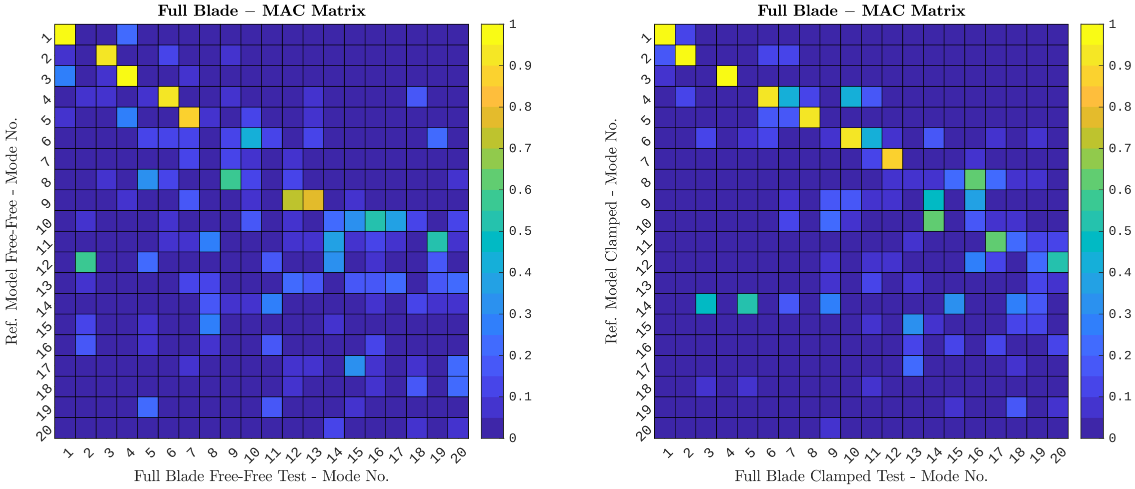

(a) Free-Free Model Configuration with Free-Free Modal Test

(b) Clamped Model Configuration with Clamped Modal Test

Figure 2.11: Full Blade Reference Model Mode Shape Correlation

Examining the free-free mode shape correlation results the first experimental modes $(1,3,4,6,7)$ show a very high MAC value and can be matched with the experimental results easily. The modes $(2,5,8\ldots)$ did not have clear identifications with the experiment, modes 2 and 5 represented the first and second breathing modes consisting of the characteristic out of plane motion of the trailing edge panels as seen in Figures 2.8b and 2.8e.

The results of the clamped experimental results also show similar results where experimental modes $(1,2,4,6,8,10,12)$ showed very high MAC values and correlated well with the predicted modes of the reference finite element model. These modes corresponded with the global behaviour of the blade namely bending, edgewise bending, and torsion modes. However clamped experimental modes $(3,5,7,9,11,13\ldots)$ did not yield a clear identification with the reference blade model.

These unidentified modes consist of breathing modes, as well some of the global modes coupled with the characteristic breathing behaviour with out of plane trailing edge panel motion. This points to a clear deficiency in the provided reference model's ability to predict the behaviour of the trailing edge panels in terms of their mode shape and frequency. To evaluate the models efficacy to predict the global modes behaviour for both test conditions the identified mode frequencies are compared in Figures 2.12 and 2.13.

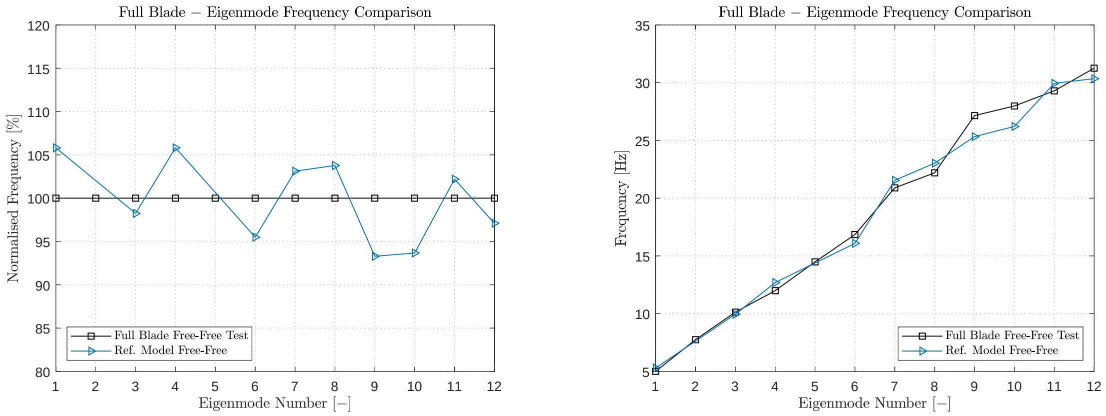

(a) Identified Mode Comparison Normalised to Experimental Modes

(b) Identified Mode Frequency Comparison

Figure 2.12: Full Blade Reference Model Free-Free Eigenmode Frequency Comparison

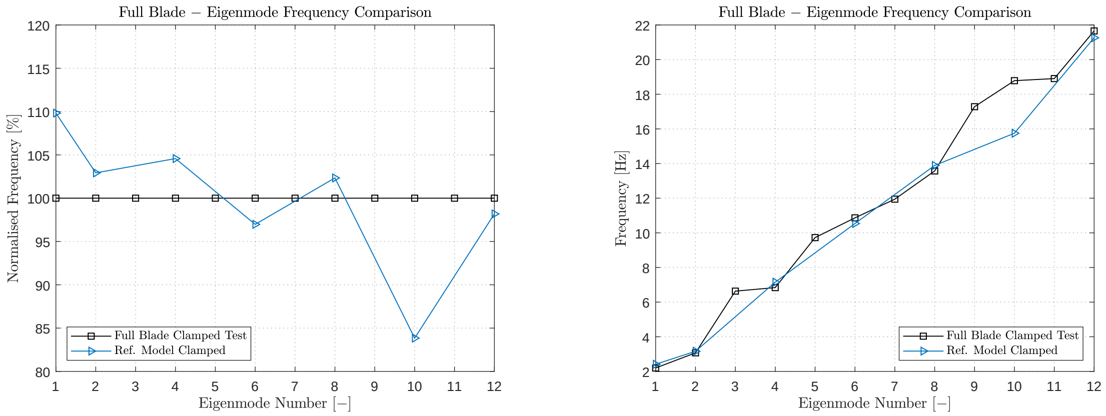

(a) Identified Mode Comparison Normalised to Experimental Modes

(b) Identified Mode Frequency Comparison

Figure 2.13: Full Blade Reference Model Clamped Eigenmode Frequency Comparison

Examining the identified global modes of the Free-Free configuration these modes match very closely within a ±7% margin of the experimental mode frequencies. Conversely the clamped configuration frequencies match less closely to the experimentally identified modes with first bending overestimated by 10% and the first torsion under estimated by 16%. There are some differences to consider though, namely the test fixture for the clamped blade is not rigid which may result in lower frequency bending modes, particularly edgewise bending (Modes of the test fixture motion were removed from the modal model). However the discrepancy in the first torsion mode is significant and likely points to a problem with the finite element model.

The modal results for both the free-free and clamped configurations were in mostly close agreement with the global modes of the blade and suggest at least a roughly accurate model. Despite the global level accuracy the reference model was unable to identify the measured 'Breathing Modes' in terms of their shape or frequency, suggesting also and underlying inaccuracy in the model.

2.2. Blade Finite Element Modelling

There are multiple different strategies to model wind turbine blades with the finite element method, each facilitating a different purpose. They are broadly categorised into beam type models [30] and shell based models [52]. The beam type models are suited to low degree freedom models used in loads analysis in multi-body simulation, and estimation of aeroelastic behaviour. Shell based models are much higher fidelity models looking at buckling, fatigue, detailed stress analysis.

2.2.1. Blade Beam Models

The traditional method for design of a wind turbine blade is to idealise it as a beam in a finite element model. This a very simple approach which is used to examine the global behaviour and allow for preliminary design of the shape and stiffness. This low degree of freedom model permits very fast computation which allows for effective optimisation techniques for the design parameters. These beam models serve as the fundamental input for the loading analysis and aeroelastic simulation programs such as FLEX, Bladed, Phatas, FAST, and HAWC2 [5].

Load analysis programs for wind turbines are often derived from the Blade-Element and Momentum Theory [5] for horizontal axis wind turbines. This theory discretises the wind turbine blade into span-wise annular elements of the swept area of the turbine. Knowing the taper, twist, and lift/drag coefficients along the span of the blade in addition to the operating conditions like rotor speed, and wind speed the torque and thrust load distribution on the blades can be solved for iteratively from the sets of equations. Additionally lift and drag coefficients of the airfoil need to be determined from CFD or experiment which plays a key role in the design of the blade features. This theory is aerodynamic in nature and covers static operational loads, the certification regulations specify the operating conditions which the wind turbine blades must be designed for [17].

Dynamic aeroelastic analysis of wind turbine blades also centres around idealisation of the blade as beam. The basis of dynamics of the turbine blades are the eigenmodes and damping, these define and dictate the response of the blade to an excitation. Typically the wind turbine blade will be designed such that it is always in a stable aeroelastic behaviour, that is the damping of its principal eigenmodes is positive. A common example of an unstable or negative damping condition of wind turbine blades is when the turbine is operating near stall speed where the buffeting can excite the first flap-wise eigenmode of the blade structure [30] or classical bending torsion flutter at higher velocities. Excitation of these low or negatively damped modes in operation can induce high frequency loads into the structure and reduce the fatigue life or even cause structural failure. To simulate these conditions the structure is idealised as a beam with undeformed cross section, as the aerodynamic behaviour is modelled in 2D space. Furthermore it is much simpler as aeroelasticity is considering global vibration behaviour only and the local or high frequency modes of the structure are not considered in these simulations. This however is only considering the blade, when including all of the other aspects of the system such as the tower, drivetrain, and all 3 blades together the behaviour of the system becomes much more complex. Necessarily, advanced aeroelastic software extends the blade element momentum theory with unsteady aerodynamics are used to determine aeroelastic behaviour and load spectra for a variety of operating conditions of the entire wind turbine system.

Beam based models are very useful for global level analysis of the blade useful for load analysis and initial design however there are limitations imposed by the simplicity of a beam based model. They cannot model panel buckling often a critical failure mode for the static load cases [14]. This can extrapolated for non-linear panel movement under loading from geometric imperfections which can result inaccurate stresses in the panels [7]. Additionally any kind of local concentrated loading cannot be modelled with beam elements.

In terms of estimation of modal parameters for aeroelastic analysis, beam models tend to have close agreement with shell based models for these global vibration modes [7, 14]. However beam models only capture global behaviour, and are not able to predict these breathing modes found in Section 2.1.4. Therefore higher fidelity shell models are typically used for these more detailed applications.

2.2.2. Blade Shell Models

Shell based finite element models of wind turbine blades are particularly useful to obtain high fidelity results for detailed design and verification. Due do the full detail modelling of all panels and joints this allows for more accurate stress results in non-linear static analysis, and prediction of panel buckling. Additionally shell based models allow modelling of panel vibration modes, which have been measured in Section 2.1.4. An important aspect of these analysis is how the shell based models are constructed, with which element types and connections.

Shell models are usually constructed from the wet surface geometry with offsets to the mid-plane of panels set into the element stiffness formulation. This makes the geometry of the blade accurate to the moulds and is easily constructed from CAD data. In this thesis MSC NASTRAN models of the blade structures are used, with the models built from an Abaqus CAE database of geometry.

In wet surface shell models there are two methods for mid-plane offset of the shell, direct inclusion of the offset into the classical laminate theory calculations and virtual offsetting of the element nodes. Both have a similar effect on the global stiffness but can produce different results in regards to laminates stresses, nodal loads, and buckling [38]. For the analyses made in this work the model uses composite property offsets into the classical laminate theory calculations, thereby affecting the B matrix.

All shell elements in NASTRAN are based on mindlin plate theory and incorporate membrane, flexural, and transverse shear into the element stiffness. For laminated composites with varying transverse stiffness, particularly sandwich core laminates, a correction to the transverse shear is needed. The transverse shear distribution in a laminate is zero at the faces and varies parabolically to a maximum in the mid-plane. Mindlin plate theory assumes a constant distribution, and requires a stiffness correction such that the transverse strain energy in the mindlin plate is equivalent to that of the true case. It is not possible to make correction for all loading cases therefore the laminate strain energy is compared for a special case of cylindrical bending between where a shear correction factor is defined in Equation 2.2. [6, 45, 54]

$$K = \frac{H}{\bar{H}} \tag{2.2}$$

Where H is the laminate transverse shear stiffness matrix taken from an equilibrium approach defined in [45], and $\bar{H}$ is the transverse shear stiffness matrix for a constant strain approach consistent with Mindlin plates. For a fully isotropic plate the trivial solution is $K = 5/6$, however for laminates with anisotropy and core materials the shear correction factor can vary considerably. This is of particular importance as sandwich structures are heavily affected by this correction factor due to the very low stiffness of the core material. The shear correction factor plotted for varying ratios of core to face thickness and stiffness is shown in Figure 2.14.

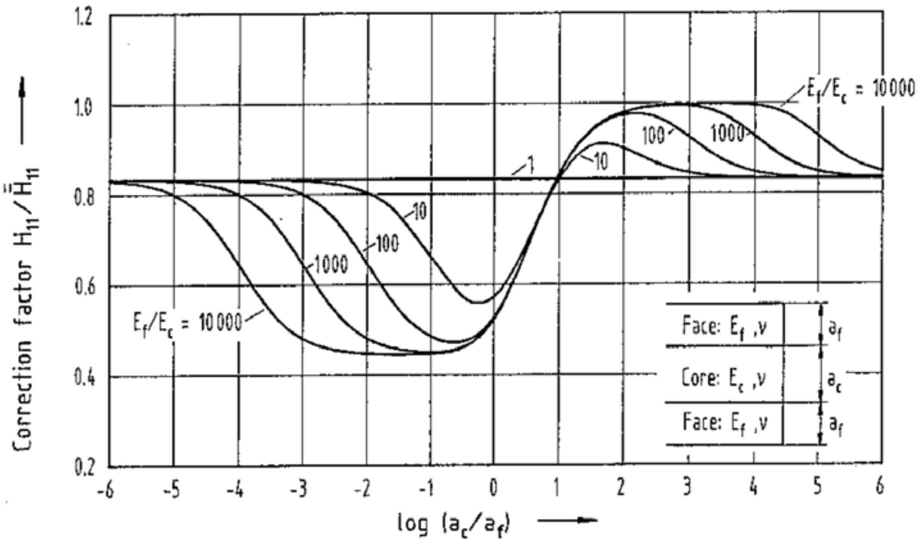

Figure 2.14: Shear Correction Factors for Isotropic Sandwich Plate [45]

Fortunately most finite element software make this correction automatically in the property determination composite laminates, including NASTRAN which is used in this study.

Regarding choice of element, for flat low single curved panels it is more accurate to use quadrilateral elements as triangular elements are constant strain and behave overly stiff in areas of changing strain such as a spar. For wind turbine blades this is the predominant type of panel used to shape the airfoil, and therefore it is most desirable, and triangular elements should only be used where mesh transitions are required.

For stress, buckling, and fatigue analysis quadratic type elements are more desirable as the strain is approximated more accurately by the shape functions. However for global level behaviour as seen in modal analysis linear type elements are also suitable and they tend to converge in behaviour with quadratic type elements. The mindlin based shell elements are similar in that they only have 5 degrees of freedom as out of plane torsion, i.e. drilling torque, is not modelled. Developments made have seen its inclusion into NASTRAN as a separate quadrilateral and triangular element type *CQUADR*, and offers improved membrane behaviour over its basic linear counterpart.

As examined in Section 2.1 low frequency panels modes have been observed experimentally and the reference finite element model has been unable to predict this. So while these shell models are highly detailed, they are only as good as how the structure is modelled in terms of the topology, materials, and conditions applied to them.

2.2.3. Glue Joint Models

Part of using a shell based finite element model for a wind turbine blade is how the joints are modelled connecting the substructures of the blade together. In a wind turbine blade there are several adhesive joints which run along the span-wise direction connecting the shells and spar web together. In the case for SmartBlades2, there is a leading and trailing edge joint connected via adhesive, as well as adhesive joints for the spar web to the pressure and suction side shells.

One approach to modelling adhesive joints is omitting the glue joint effect all together and connecting the shells with a laminate. This is only applicable to the trailing edge joints where they more closely resemble a lap joint. This is a commonly used approach when examination of bonding joints or panel behaviour is not the primary interest, for example in optimisation problems [33]. This approach poorly constrains the panels and results in underestimated buckling modes [26].

Another approach is to use multi point constraints to connect the the modes of the joint substrates together, for example using cohesive connections with a specified stiffness. This captures the stiffening effects of the glue joints but does not model the glue itself having reduced degrees of freedom.

When examining the behaviour of the glue specifically, modelling the adhesive zone using solid continuum elements in usually preferred and offers the highest accuracy results compared to other methods [26]. This allows to capture the precise geometry of the glue joint. The solid glue elements are either connected directly using merged nodes where the element size is consistent across the glue and shells. Alternatively the glue elements can have a much higher element density and be connected connected via multi point constraints to the substrates, this approach is usually taken when wanting to model stresses within the glue joint though its thickness for example in fatigue analysis [12].

2.3. Experimental Modal Analysis

A major aspect of this thesis is to interpret experimental vibration test data to build modal models of the test objects. This serves as a basis for comparison with finite element analysis and therefore the process by which these modal models are made must be understood to put their comparison into context.

2.3.1. Vibration Testing

To conduct a classical vibration test one needs 3 major elements, firstly a well defined structure with known or approximate boundary conditions. This should contain specific excitation and response locations to facilitate consistent measurements as well as proper comparisons with other tests and finite element models. The boundary conditions should also be well defined as these can often be difficult to replicate well in finite element based models. Free-free conditions are used as they are the simplest to replicate by hanging the structure on low stiffness bungee cords and have the most consistent results [9]. Clamped conditions are also often used to simulate operations but can lead to worse comparison with finite element models if the connections are not sufficiently rigid.

The second major element of a vibration test is the measurement of the excitation of the structure. The most common excitation methods are vibration shakers or impulse hammers. A vibration shaker has many options with respect to the input spectra and can offer better results as the input energy is higher and is often used for large or high damping structures. The impulse hammer is also very versatile allowing for multiple ranges of input energies and spectra based on hammer mass and hardness of the hammer tip.

The third major element of a vibration test is the measurement of the response of the structure. Most commonly this is measured by means of accelerometers of the piezoelectric type although there are many others.

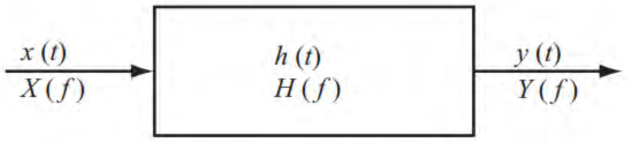

Figure 2.15: Linear time-invariant system with input $x(t)$, output $y(t)$, impulse response $h(t)$ and frequency response function $H(f)$ [9]

To obtain modal parameters from the vibration test, the structure is idealised as a linear system depicted in Figure 2.15, with input $x(t)$ as the excitation, and output $y(t)$ as the response related by a transfer function $h(t)$ show in Equation (2.3). For convenience this can also be imagined in the frequency domain by applying the Fourier transform as shown in Equation (2.4), where $X(f)$ is the input spectra, $Y(f)$ is the output spectra, and $H(f)$ is the transfer function, also called the Frequency Response Function or FRF. The formulations made in this section are based upon those found in [9, 43].

$$y(t) = x(t) * h(t) = \int_{-\infty}^{\infty} x(u)h(t-u)\mathrm{d}u \tag{2.3}$$

$$Y(f) = X(f) \bullet H(f) \tag{2.4}$$

For the purposes of simplicity the influence of noise is neglected in this formulation. To understand the derivation of the frequency response function first the power spectral density is defined. The power spectral density of a signal(s) $G_{ij(f)}$ is defined as the Fourier transform of the correlation function of the signal(s) $R_{ij}(t)$, shown in Equation (2.5). The correlation function is defined as the expected value E of time signal(s) $i(t), j(t)$, as shown in Equation (2.6).

$$G_{ij}(f) = \mathcal{F}\{R_{ij}(t)\} = J^*(f)I(f) \tag{2.5}$$

$$R_{ij}(\tau) = E\left[i(t)j(t-\tau)\right] = \frac{1}{T-|\tau|}\int_{-T/2}^{T/2} i(t)j(t-\tau)\mathrm{d}t = \mathcal{F}\{G_{ij}(f)\} \tag{2.6}$$

Calculating the power spectral density directly from the time domain is impractical. The PSD is much simpler to calculate using the signal spectra(s) $I(f), J(f)$ which can be quickly transformed to frequency domain spectra's using discrete fourier transforms. The calculations in frequency domain are also shown in Equations (2.5) and (2.6).

If a signal is correlated with itself it is called an auto-power and is a real valued function, and if a signal is correlated with a different one this is called the cross-power and it is a complex valued function. This is also defined in the frequency domain as the product of the complex conjugate of one spectra with another.

To obtain the frequency response function Equation (2.4) is multiplied with the complex conjugate of the input $X^*(f)$, which allows to insert the definition for the power spectral density as shown in Equation (2.7).

$$\begin{gathered} X^*(f)Y(f) = X^*(f)X(f)H(f) \\ G_{yx}(f) = G_{xx}(f)H_1(f) \end{gathered} \tag{2.7}$$

This equation for the frequency response function (FRF) is known as the H_1 estimator. The H_1 estimator assumes no noise on the input signal and an uncorrelated output noise. Alternatively there are also the H_2 and H_c estimators. The H_2 estimator assumes an uncorrelated input noise and clean output signal. The H_c estimator assumes noise on both input and output however an additional channel is needed to measure a signal without noise such as the output of the signal generator to a shaker. In hammer testing Welch's method of averaging is used where averages of the power spectral density from multiple runs are used which reduces the presence of noise in the resulting FRFs [9]. Multiple averages used in conjunction with the H_1 estimator is a very common technique, and is the method used in the testing of the structures in this work.

When working with experimental data these are not continuous time and frequency signals but discrete and therefore the elimination of the influence of Noise is required. This done by making an average of the Frequency Response Function from multiple excitation and response signals shown in Equation (2.8).

$$\hat{H}_1(f) = \frac{\hat{G}_{xx}}{\hat{G}_{yx}} \tag{2.8}$$

This can also be extended for multiple input multiple output systems. The thesis contains multiple modal tests where several output signals are used so the MIMO system definition is also shown here.

For a MIMO system the estimates for the Frequency Response Functions should be expressed in a matrix form. Where input vector $[X]$ is of length q shown in Equation (2.10), output vector $[Y]$ is of length p shown in Equation (2.9), and the Frequency Response Function Matrix $[H]$ is in the shape (p,q) shown in Equation (2.11).

$$[Y] = \left[Y_1(f), Y_2(f), Y_3(f) \cdots Y_p(f)\right]^T \tag{2.9}$$

$$[X] = \left[X_1(f), X_2(f), X_3(f) \cdots X_q(f)\right]^T \tag{2.10}$$

$$[H] = \begin{bmatrix} H_{11}(f) & H_{12}(f) & \cdots & H_{1q}(f) \\ H_{21}(f) & H_{22}(f) & \cdots & H_{2q}(f) \\ \vdots & \vdots & \ddots & \vdots \\ H_{p1}(f) & H_{p2}(f) & \cdots & H_{pq}(f) \end{bmatrix} \tag{2.11}$$

The linear system can then be expressed in matrix terms in Equation 2.12. Applying the same methodology as for SISO system Equation 2.12 is multiplied with the Hermitian transpose shown in Equation 2.13. This results in Equation 2.14 relating the frequency response function matrix with the input auto-power spectral density and input-output cross-power spectral density matrices.

$$[Y] = [H]\,[X] \tag{2.12}$$

$$[Y]\left[X^H\right] = [H]\,[X]\left[X^H\right] \tag{2.13}$$

$$\left[G_{yx}\right] = [H_1]\,[G_{xx}] \tag{2.14}$$

To complete the calculation of the $[H_1]$ estimator for MIMO systems shown in Equation 2.15, it must be possible to invert the $[G_{xx}]$ matrix thus for it to be non singular. In physical terms this means that the coherence between any two different inputs is non unity for the whole frequency spectrum, essentially the input channels are independent. For testing of larger structures with multiple input signals the single virtual driving point method is often used. This is where correlated input signal sine sweeps are used either in phase or 180° out of phase, this violates the invertability requirement for the H_1 estimator and different techniques are required to calculate the FRFs detailed in [16]. The SVDP method was used in part of the testing for the SmartBlades2 prototype blade.

$$\left[\hat{H_1}\right] = \left[\hat{G_{yx}}\right]\left[\hat{G_{xx}}\right]^{-1} \tag{2.15}$$

2.3.2. Modal Parameter Identification

Assuming a valid set of frequency response functions are obtained from the initial vibration testing the next step is to find the modal properties from these data. This comprises the large field of modal parameter identification. There are many different methods used to synthesise modal parameters from the FRFs, for sake of brevity only the category of the least squared complex frequency (LSCF) methods are overviewed here [22, 23, 40].

The modal parameters of main interest in modal identification are the natural frequency f_r, damping ζ_r, and mode shapes $[\psi]_r$. The LSCF method applies rational function approximation of arbitrary order to the frequency response functions from the vibration testing. The synthesised transfer function between output $o(o = 1,\ldots,N_o)$ and input $i(i = 1,\ldots,N_i)$ is defined as $\tilde{H}_k$ where $(k = 1,\ldots,N_i N_o)$, it is shown in Equation (2.16).

$$\tilde{H}_k(\omega_f) = \frac{N_k(\omega_f)}{D(\omega_f)} \tag{2.16}$$

$$N_k(\omega_f) = \sum_{j=0}^{n} \Omega_j(\omega_f) B_{kj} \tag{2.17}$$

$$D(\omega_f) = \sum_{j=0}^{n} \Omega_j(\omega_f) A_j \tag{2.18}$$

$$\Omega_j(\omega_f) = e^{-i\omega_f \Delta t_s \bullet j} \tag{2.19}$$

Where $N_k(\omega_f)$ are the numerator polynomial functions between input i and output o, and $D(\omega_f)$ are the common denominator functions. The common denominator functions are the same for all the FRFs of the system and define the poles, this is shown in Equation (2.18). The Numerator functions define the participation factors for each FRF for every pole, shown in Equation (2.17). Both of these use the polynomial basis function Equation (2.19) of arbitrary order n with discrete frequency ω_f and discrete time interval from the sampled data Δt_s. The coefficients of these two functions A_j and B_{kj} are unknown and must be estimated, for convenience they are grouped into a column vector θ, shown in Equations (2.20) to (2.22).

$$\theta = \left[\beta_1^T, \ldots, \beta_k^T, \alpha^T\right]^T \tag{2.20}$$

$$\beta_k = \begin{bmatrix} B_{k0} \\ B_{k1} \\ \vdots \\ B_{kn} \end{bmatrix} \tag{2.21}$$

$$\alpha = \begin{bmatrix} A_0 \\ A_1 \\ \vdots \\ A_n \end{bmatrix} \tag{2.22}$$

The objective is to then formulate a solution to identify the best coefficients for each model order, this is often done using a variation of least square based methods. This is where the similarities between the LSCF methods end, most use different strategies with the PolyMAX and pLSCF methods being the most popular, with pLSCF being the method used in this thesis[23, 40]. These methods estimate the poles directly allowing for calculation of the eigenfrequency and damping parameters for varying model order. The numerator values are then calculated for a particular mode/pole from the estimated values in the previous step. To extract the mode-shapes from a particular pole the so called Least Square Frequency Domain Estimator (LSFD) method is used [22, 23, 40].

The estimated poles are then plotted in a so called stabilization diagram where the poles are shown for increasing model order, on top of the measured FRFs. For the best results the LSCF estimators are typically run over multiple small frequency bands where only 3-5 poles are present in each. The poles from all of the excitation runs are organised into families where they are grouped by mode number. The estimated poles from these families are evaluated with quality criteria such as the Mode Indicator Function and Mean Phase Deviation. The poles which best represent the dynamic behaviour from each family are chosen and synthesised together to create a modal model with the measured systems estimated natural frequencies f_r, damping ζ_r, and mode shapes $[\psi]_r$. The modal model can then be used for simulation input, comparison with different tests, and verification of finite element simulations.

3

Model Topology Effects

To determine the source of the breathing mode discrepancy from the reference finite element model and the modal tests a focussed approach is applied. A span-wise section of the blade, referred to as the blade section, has been cut away from the original blade and subject to modal tests. This smaller section of blade allows for a detailed study of the model topology effects on the modal response of the blade section. Examination of the topology on this smaller section of blade concerns increasing the fidelity of the modelled features to match that of the manufactured blade section.

First an explanation of the modal tests made on the blade section is described in Section 3.1. Here the test conditions are detailed, and the modal model used for subsequent comparison is established. Following this an iterative improvement process is applied to the the topology of the blade section finite element model in Section 3.2. The effects of the topology changes and conclusions are explained in Section 3.3.

3.1. Blade Section Tests

To understand the effects that different finite element topology configurations have on the modal behaviour, a small span-wise section of the blade was selected for testing to facilitate faster model iteration. The used section of the prototype blade is 3.5 m long and was cut from 12.5 m to 16.0 m span. The blade section includes the most important topological features present on the full blade model allowing for a suitable comparison to the full scale. The mass properties of the Blade Section were measured and transformed in the blade's global reference frame for comparison purposes with the finite element models, this is presented in Table 3.1.

Table 3.1: Mass and Centre of Gravity for the SmartBlades2 Blade Section

Mass [kg]	CoG X [mm]	CoG Y [mm]	CoG Z [mm]
187	14087	-210.12	109.02

3.1.1. Modal Testing

The Blade Section was subjected to two different tests approximating the Free-Free condition. In the first test the blade section was suspended via two load straps slung chord-wise along the exterior and directly attached the supporting gantry as shown in Figure 3.1a. This first test used both a shaker and impulse hammer as excitation sources with a very high sensor density. The sensors were arranged with 9 sections along the span with each section containing 14 accelerometers. These accelerometers were pre-oriented into the global reference frame primarily in the Y and Z axes, this is illustrated in the sensor diagram of Figure 3.2a.

The second modal test was conducted on the Blade Section using a different suspension method attempting to better replicate the Free-Free condition. The first test hung the blade section directly to the support gantry however this did not enforce low frequency rigid body modes which may have had a negative affect on the extracted modal parameters. The potential effects of the suspension method from the first modal test are explored in Section 3.2.6. As a result of this analysis it was necessary to validate the original test with a second modal test.

The second modal test was conducted using bungee suspension from the leading edge compartment to eliminate the influence of rigid body modes on the elastic behaviour, the test setup is shown in Figure 3.1b. For this second modal test, impulse hammer excitation was used with a lower sensor density of 5 sections and 7 sensors at each section. Similar to the first test the accelerometers were pre-oriented into the out of plane directions, primarily the Y and Z axes of the global reference frame. A diagram of the sensor placement and orientations are shown in Figure 3.2b.

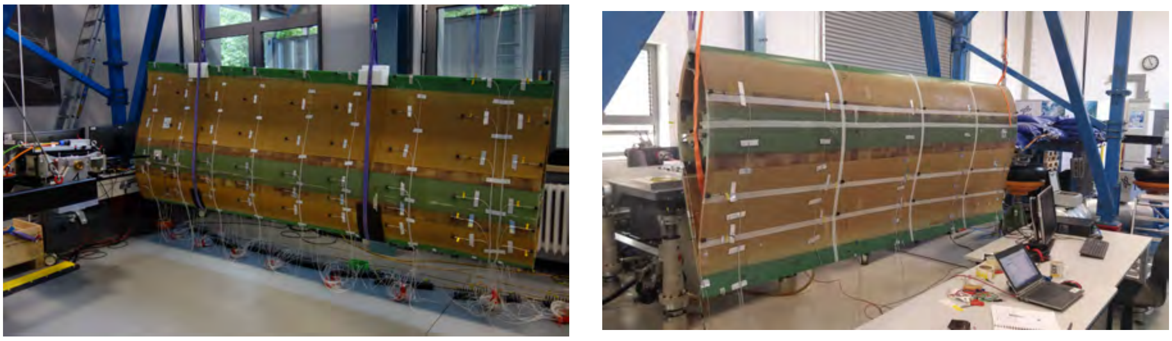

(a) Blade Section Modal Shaker Test Setup

(b) Blade Section Modal Hammer Test Setup with Bungee Suspension

Figure 3.1: SmartBlades2 Test Section Experiment Setup

In both tests the sensors were pre-oriented in the global reference frame of the blade (ie: not normal to the surface), this was done to reduce the amount of required post-processing. The shaker test used both sine-sweep signals and random signals at varying levels of intensity to excite the structure. For the hammer excitations multiple different excitation points were used particularly excitation points around the trailing edge panels were chosen to excite breathing motion. Following testing the frequency response functions for all excitations were processed, after which the pLSCF modal identification method was applied to find the best modes via the usage of stabilisation diagrams, this process is described in Section 2.3.2.

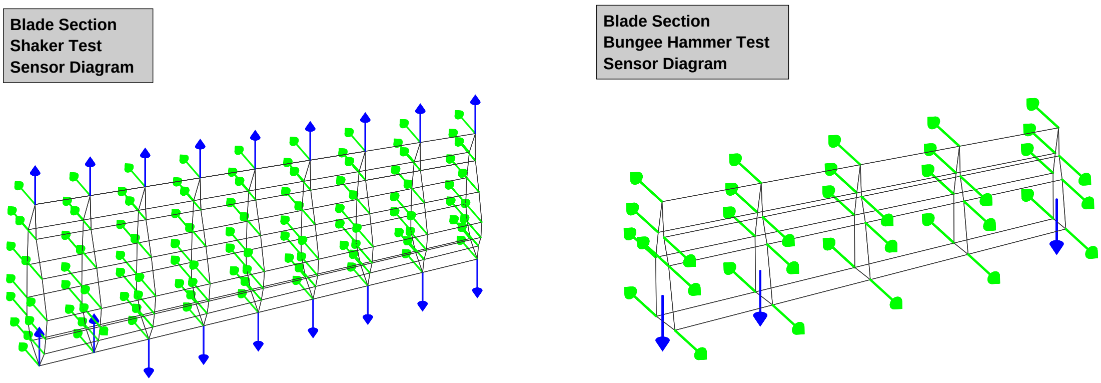

(a) Blade Section Shaker Test Sensor Diagram

(b) Blade Section Bungee Hammer Test Sensor Diagram

Figure 3.2: Sensor Position and Orientation Diagrams for Blade Section Modal Tests

For both tests the different excitation runs were examined and the best modes from each were collated into a modal model to represent the experiments dynamics model. This modal model represents a synthesised dynamic model of the experiment, this is illustrated in stabilisation diagram for the bungee test modal model shown in Figure 3.3.

The stabilisation diagram shows the summed frequency response function from one hammer excitation run in dotted orange as well as the synthesised frequency response function in dotted blue generated from the modal model. Each of the modes is represented by a vertical black line and box corresponding to the order of the approximation with the pLSCF method. For each of these modes the mode indicator function value, damping ratio, and frequency are written for from top to bottom respectively. Lastly the mode indicator function value is plotted in the background in solid blue showing the expected locations of modes from the measured response.

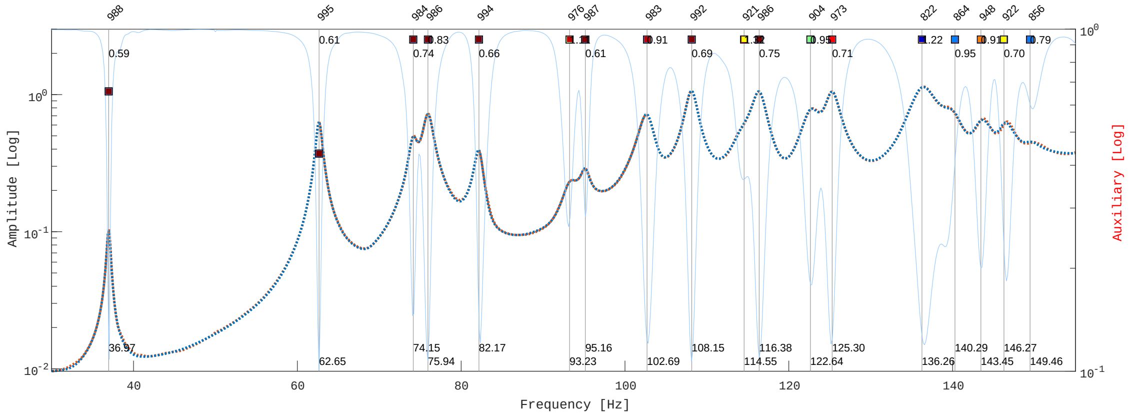

Figure 3.3: Blade Section Bungee Test Modal Model Stabilisation Diagram

3.1.2. Modal Results

For the shaker test and the bungee test the modal models were generated and their results are examined here. Both tests used slightly different geometry and boundary conditions however the results were fairly consistent between both tests. The auto correlation of the two extracted modal models is shown in Figure 3.4.

The shaker test modal model autocorrelation shown in Figure 3.4a for the mode shapes is very good with only one off significant off-diagonal value between modes 2 and 3. The mode shapes of the shaker test modal model shown in Figure 3.6, reveals that these modes have extremely similar shapes however slightly differ in frequency with mode 2 at 56.9 Hz and mode 3 at 63.6 Hz. These evidently are very closely related modes, however the stabilisation diagram for the random excitation a prominent peak was observed shown in Figure 3.5.

The peak found in the frequency response functions was only found for shaker excitations, therefore it could be a spurious testing artefact but conversely the higher excitation levels of shaker may have shown a different mode here but the modal identification algorithm was unable to decouple it from mode 3. For this reason mode 2 of the modal model will be kept for further comparison however it should be noted for the blade section results that this second mode may be spurious.

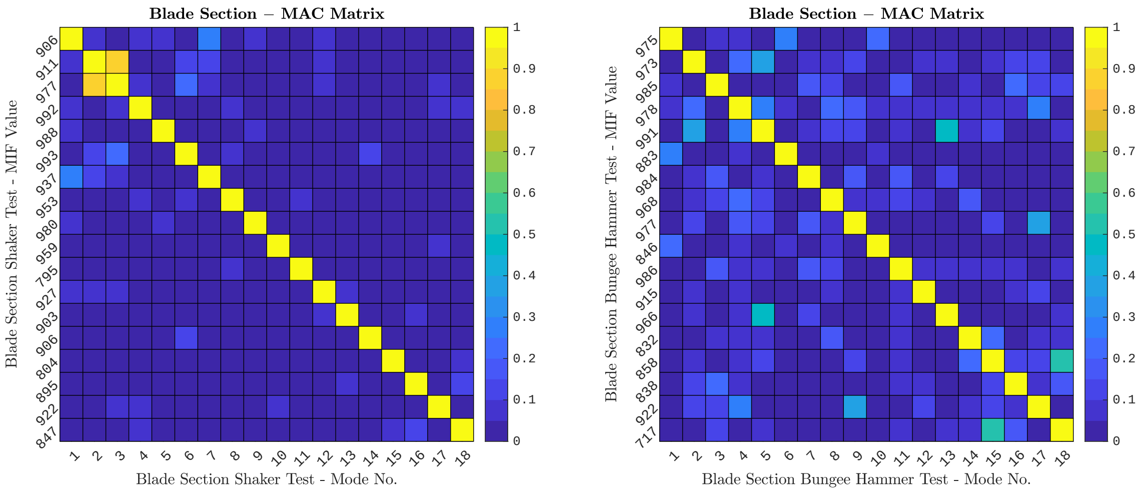

(a) Blade Section Shaker Test Auto MAC Plot

(b) Blade Section Bungee Hammer Test Auto MAC Plot

Figure 3.4: Blade Section Auto Modal Correlation Plots

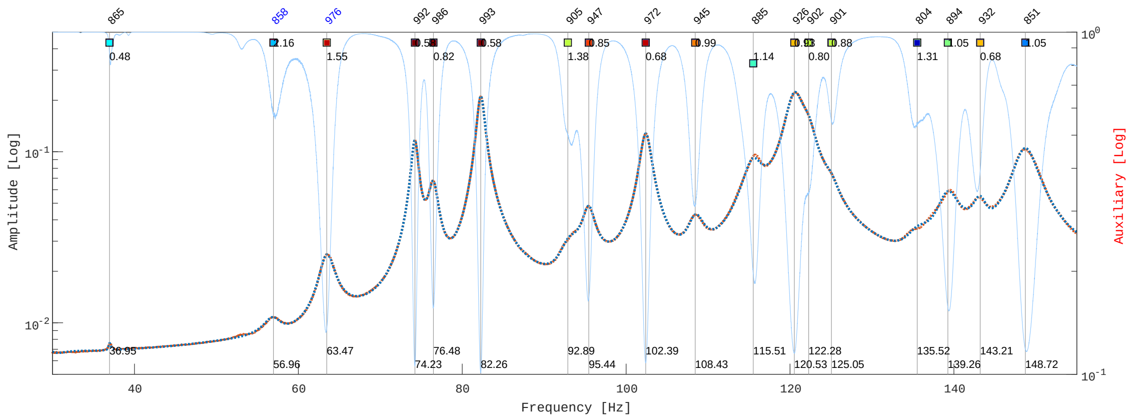

Figure 3.5: Blade Section Shaker Test Modal Model Stabilisation Diagram

The second test conducted on the blade section using bungee suspension was effective in separating the rigid body modes from the elastic modes. During the experiment the structure was excited by hand to excite the rigid body modes. Taking the frequency spectra of the accelerometer measurements the highest rigid body frequency was found to be < 2.5 Hz, this provides a ratio of 1 : 14.7 to the first identified elastic mode well above the ideal ratio of 1 : 10 [11, 57].

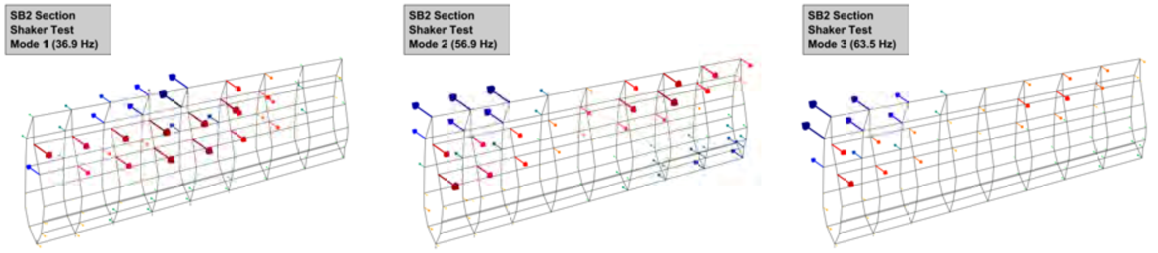
SB2 Section
Shaker Test
Mode 1 (36.9 Hz)
SB2 Section
Shaker Test
Mode 2 (56.9 Hz)
SB2 Section
Shaker Test
Mode 3 (63.5 Hz)

(a) Mode 1: First Breathing (b) Mode 2: Second Breathing (c) Mode 3: Second Breathing (Validated)

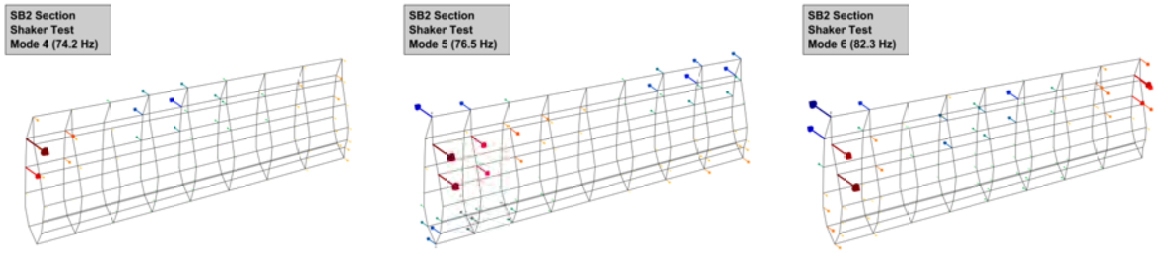
SB2 Section
Shaker Test
Mode 4 (74.2 Hz)
SB2 Section
Shaker Test
Mode 5 (76.5 Hz)
SB2 Section
Shaker Test
Mode 6 (82.3 Hz)

(d) Mode 4: First Bending (e) Mode 5 (f) Mode 6

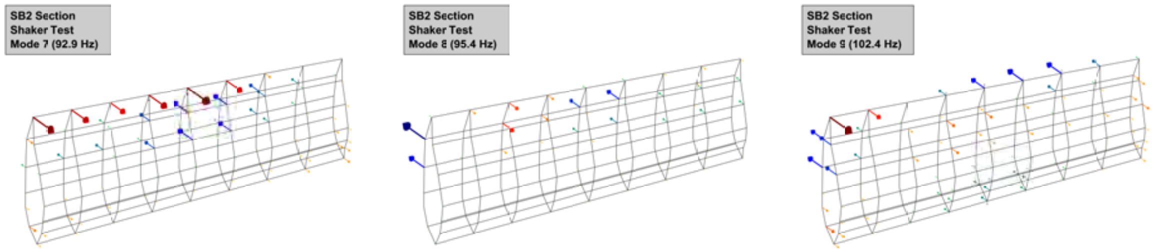
SB2 Section
Shaker Test
Mode 7 (92.9 Hz)
SB2 Section
Shaker Test
Mode 8 (95.4 Hz)
SB2 Section
Shaker Test
Mode 9 (102.4 Hz)

(g) Mode 7 (h) Mode 8 (i) Mode 9

Figure 3.6: Blade Section Shaker Test Identified Mode Shapes 1-9

The Bungee test modal model autocorrelation is shown in Figure 3.4b. The auto correlation showed a less clean result than the shaker test with higher noise in the off diagonals however this is primarily for the reduced number of sensors. Most notably not significant off diagonal values showed no coupling or artefacts from the extracted modal models.

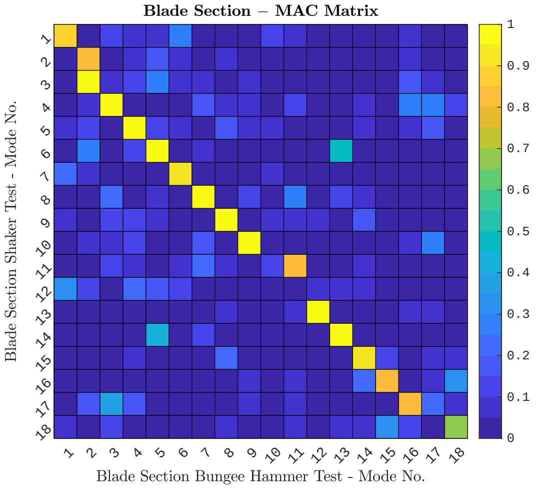

Figure 3.7: Blade Section Shaker Test - Bungee Hammer Test MAC Plot

Most of the sensors for the Bungee test were in the same positions as during the Shaker test, this allowed both modal models to be correlated to verify the effect of the boundary conditions, this is shown in Figure 3.7. The correlations shows very close agreement between the two tests with the exception of Shaker modes 2 and 12 as well as Hammer test mode 10. Shaker mode 2 has already been explained as possibly spurious, with respect to the two higher frequency modes not identified it is possible they were not sufficiently excited during the tests to be identified reliably. However these modes are not the primary interest of the analysis in this thesis as mostly the first blade section modes with Breathing Modes effects are of interest. Therefore these modes are not considered important for our purposes.

With those considerations in mind it can be stated that the the bungee test has verified the results of the higher fidelity Shaker test. Therefore it was shown that the rigid body modes of the suspension straps did not greatly affect the low frequency panel modes being measured. The modal model of the shaker test also indicated better orthogonality between mode shapes and more measurement points are available for comparison with the finite element models which provides for a better baseline of comparison. For these reasons the higher fidelity results of the shaker test are primarily used for comparison with the finite element models in Section 3.2.

3.2. Blade Section Topology

To study the effects of finite element model topology on the prediction of breathing modes the blade section is used as a small scale model to test changes. The reference finite element model of SmartBlades2 introduced in Section 2.1.6, is used a baseline model to apply iterative topology improvements. To prepare this model to match the Blade Section the reference model is cut along planes at 12.5 m and 16.0 m in span-wise position to match the test article. The reference model was originally built in an Abaqus CAE database, and translated to a NASTRAN input deck, this NASTRAN file served as the reference finite element model. As a result of this model translation and license restrictions, the raw finite element input deck was only available to be modified. The Blade Section finite element model is shown compared with the test article in Figure 3.8.

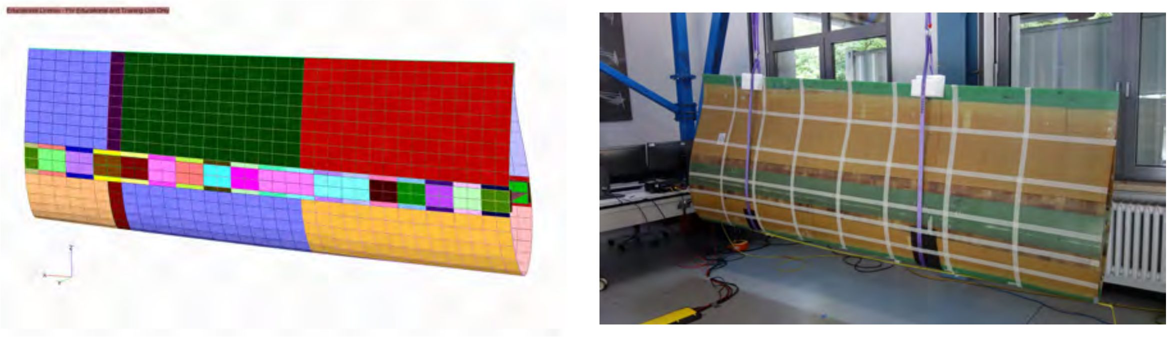
(a) Blade Section Reference Finite Element Model (Coloured by Property)

(b) Blade Section Test Article in Shaker Test Suspension

Figure 3.8: Blade Section Test Article and Finite Element Model Comparison

3.2.1. Reference Finite Element Model

The Blade Section reference model is meshed with 100 mm size elements in the span-wise and chord-wise directions. The model uses linear shell elements, NASTRAN *CQUAD4* and *CTRIA3* to model the panels and spar webs. The NASTRAN *PCOMP* composite properties are used to prescribe the shell element properties, these are based upon Composite Laminate Theory with a modified Mindlin Plate Theory [37, 38]. These shell elements are modelled on the design wet surface geometry of the blade with an inward offset applied to the composite properties. The solid glue joints are modelled using linear hexahedral continuum elements, NASTRAN *CHEXA* with 8 nodes. A cross-section of the reference model is compared with the blade section in Figure 3.9.

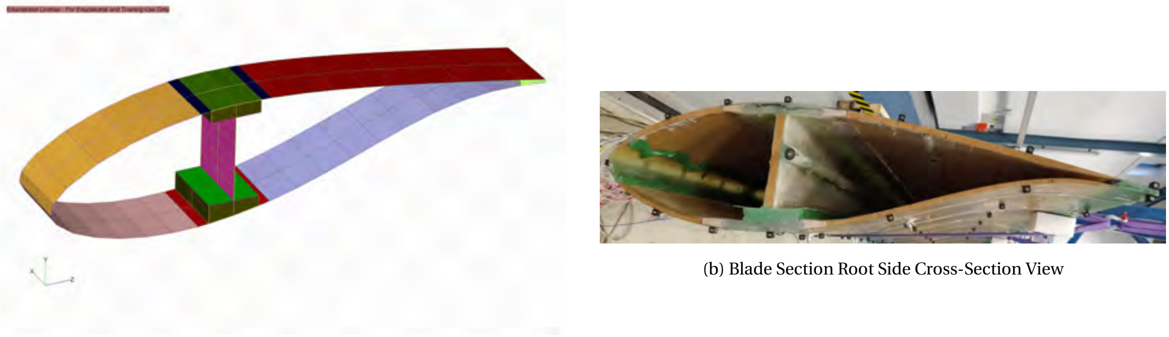
(b) Blade Section Root Side Cross-Section View

(a) Blade Section Reference Finite Element Model Cross-Section View

Figure 3.9: Blade Section and Finite Element Model Cross-Section View Comparison

The blade section reference model contains solid glue joints from the spar web to the suction and pressure side shell, as well as the solid glue joint for the trailing edge. The model does not include any implementation of the leading edge glue joint, or core taper at the trailing or leading edge. The ballast chamber on the tip side of the blade section is also not included in the reference model, as well as the lightning grounding cable on the spar web. As with the reference model of the full blade there are small inconsistencies in the laminate thicknesses between the specified material properties in the data sheets shown in Table 2.3 and the properties included in the reference model shown in Table 2.6. For the blade section the same properties used as for the reference model in Table 2.6 are used, as this chapter focuses exclusively on the affects of model topology. The blade section reference model is herein referred to as *’Reference FE Model’*.

To make the comparison with the experimental modal model of the blade section described in Section 3.1, the finite element model is subject to a free-free modal analysis where the elastic modes are compared. The modal correlation plot for the first 18 elastic modes of the reference model and shaker test modal model are shown in Figure 3.10a.

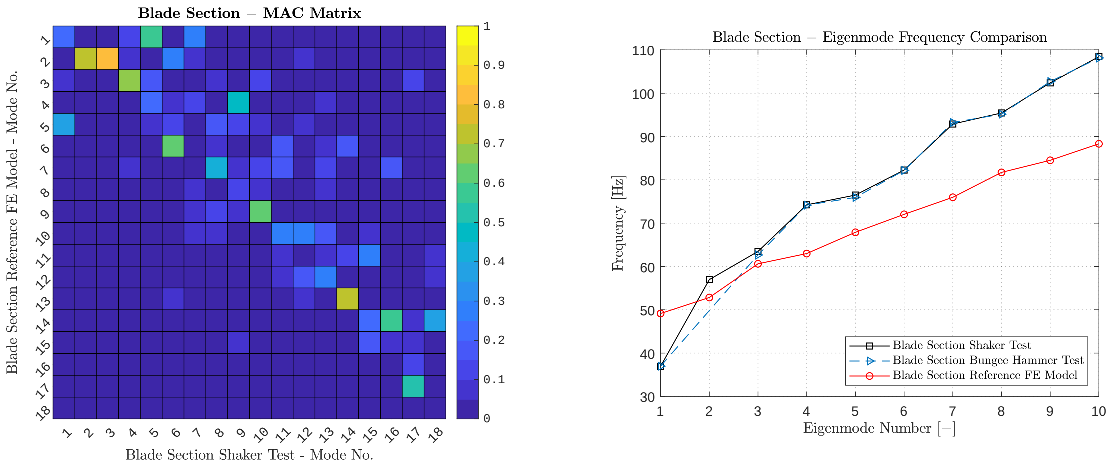

(a) Blade Section Reference FE Model - Shaker Test MAC Matrix

(b) Eigenmode Frequency Comparison Reference FE Model

Figure 3.10: Blade Section Reference FE Model Modal Parameter Comparison

The results show that the finite element model is able to correlate the first 3 FE modes with experimental modes 2 through 4. Mode 1 of the experiment, ’First Breathing’ shown in Figure 3.6a does not appear to have any significant correlation with the finite element model. This lack of this ’First Breathing’ mode is consistent with the behaviour of the full blade reference FE model. Examining the mode shape shows the largest motion at the centre of the trailing edge panels. This indicates the panels may be overly stiff, constrained, or have lower density than the test article.

Examining the frequency differences in Figure 3.10b, it is evident the finite element model under predicts the frequency of the experimentally derived modes particularly for higher frequencies. This is with exception of the first measured ’Breathing Mode’ where its frequency is significantly lower than the first predicted mode.

In linear modal analysis three main factors drive the modal behaviour: topology, mass, and stiffness. Mass and stiffness are primarily a factor of the designated material properties, whose specific effects on the modal behaviour are considered in Chapter 4. Topology differences concern that of the FE model configuration, and how this replicates the test article.

3.2.2. Trailing Edge Core Taper

The experiment found for the first three modes some ’Breathing’ like motion was observed on the trailing edge panels. Particularly the first identified mode showed a maxima of movement in the center of the panel consistent with the first breathing mode of the full blade. This ’First Breathing’ of the blade section was not identified in terms of mode shape or frequency in the reference finite element model, however it showed a lower frequency than all of the predicted modes.

This may suggest that the breathing, primarily involving motion of the trailing edge panels, may be overly constrained. A probable cause of this may be the trailing edge joint core material taper. In the reference FE model the core material thickness is constant through the whole trailing edge joint, this is shown in Figure 3.11a. This provides a local increased bending stiffness at the joint which may contribute to overly constrained panel behaviour.

To better reflect the test article a taper of the core material at the joint is implemented. The core is removed at the glue interface area and a 100 mm (1 element width) taper zone is created with half the local core thickness. The generated trailing edge taper model is shown in Figure 3.11b, which better reflects the test article joint shown in Figure 3.11c.

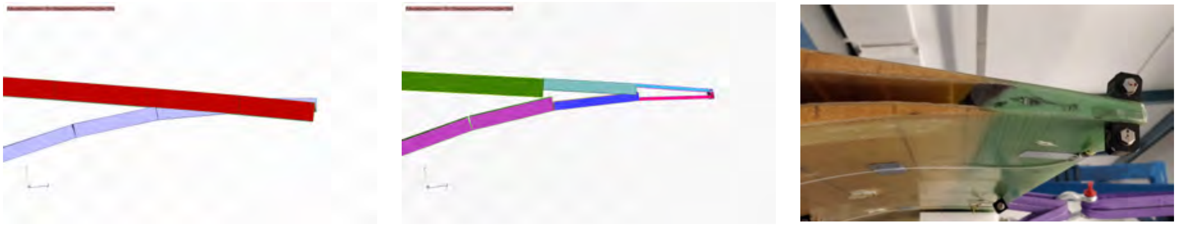

(a) Reference FE Model Shell Thickness (b) Trailing Edge Taper FE Model Shell Thickness (c) Blade Section Trailing Edge

Figure 3.11: Blade Section Trailing Edge Core Taper Comparison

This model incorporating the trailing edge taper, herein referred to as *'TE-Taper FE Model'*, is subject to a free-free modal analysis and similarly compared with the shaker test modal model. The mode shape correlation of the trailing edge model with the shaker test is shown in Figure 3.12a, and the mode frequency comparison is plotted in Figure 3.12b. Compared to the reference model mode shape correlation, the MAC values for the first three FE modes are relatively unchanged apart from what appears to be a significant change in mode order. However the experimental mode 1 first breathing still show no significant MAC value with any experimental modes. Examining the mode frequencies, the trailing edge taper model showed lower frequency compared to the reference model. This is expected and likely a results of the reduced bending stiffness of the trailing edge panels at the glue joint.

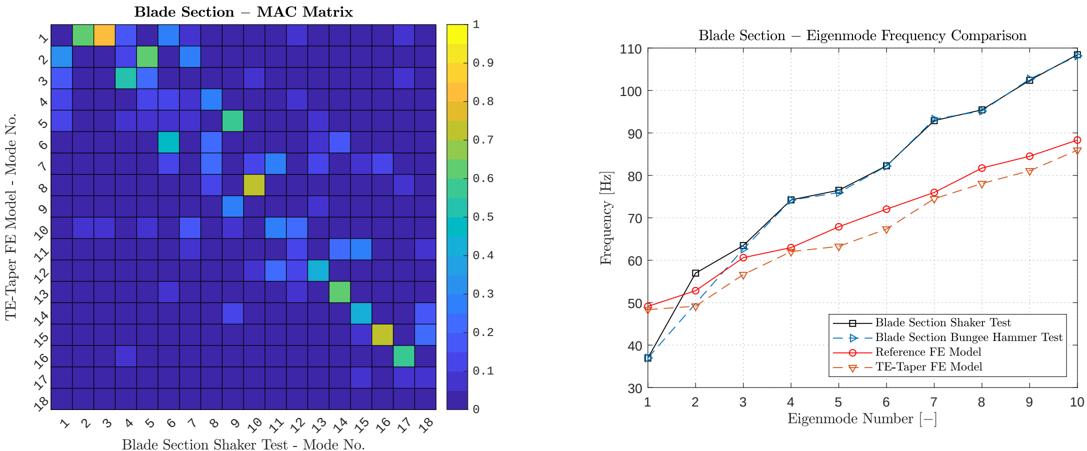

(a) Blade Section TE-Taper FE Model - Shaker Test MAC Matrix (b) Eigenmode Frequency Comparison TE-Taper FE Model

Figure 3.12: Blade Section Trailing Edge Taper Model Modal Parameter Comparison

To better illustrate the change in modal behaviour from the reference model to the trailing edge taper model, these two finite element models can also be correlated for mode shape using the same MAC value calculation procedure of Equation (2.1). Similar to correlating with an experimental modal model, the closest nodes (in this case all nodes considering the matching meshes) are matched and the similar degrees of freedom are assembled into eigenmode vectors. It should be noted when calculating the MAC matrix between two finite element models that all similar degrees of freedom are compared, that is both translations and rotations in the reference system if applicable. The blade section reference model and the trailing edge taper model are correlated in Figure 3.13.

In comparison to the reference model there are significant changes in the mode order for almost every of the first 18 modes compared. However the mode shapes generally correlate well between the models where after the model change mode MAC values remain over a value of 0.7. The obvious exception to this being reference modes 10-11 and 16-17, however these are much more complex shapes and not the primary interest.

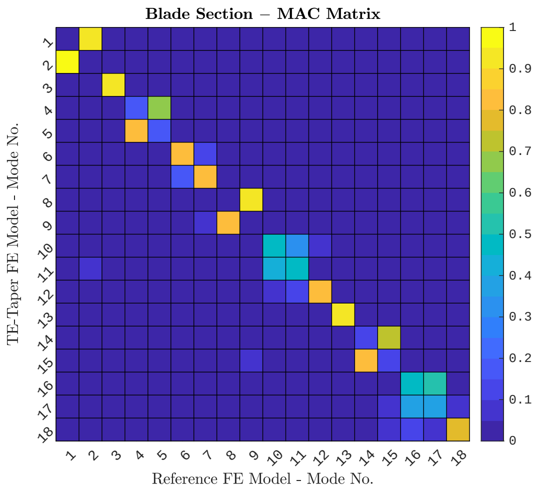

Figure 3.13: Blade Section TE-Taper FE Model - Reference FE Model MAC Matrix

The implementation of the trailing edge core taper improved the representation of the test article in comparison to the physical test article. Ultimately however, this did not actually improve the correlation with the experiment significantly and failed to predict the first breathing mode identified in the shaker and hammer tests.

3.2.3. Mesh Refinement

The blade section Reference and TE-Taper FE models, have a course mesh of 100 mm average element size in addition to some large mesh distortions on the leading edge shell tip side. It is hypothesised that this course mesh may contribute to an overly stiff out of plane behaviour, perhaps resulting in a first breathing mode which is too high in frequency and in the mode order. Therefore to mitigate this possible affect the mesh was repaired in the leading edge area and the elements were split in the chord-wise direction to have an approximate 50 mm width while maintaining the 100 mm size in the span-wise direction. This finite element model incorporates the TE-Taper feature with the refined mesh and is referred to as *'Refined Mesh FE Model'*. Figure 3.14 illustrates the differences between the meshes of the reference FE model and the refined mesh model.

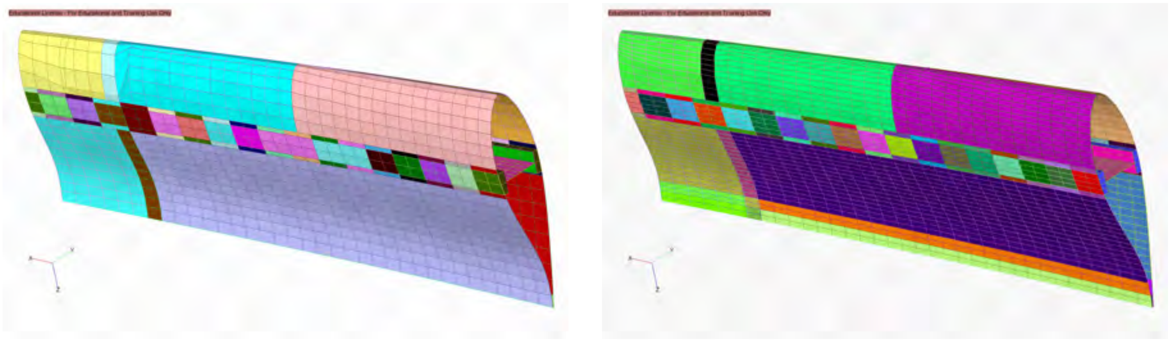

(a) Reference FE Model Pressure Side Mesh

(b) Refined Mesh FE Model Pressure Side Mesh

Figure 3.14: Blade Section Refined Mesh FE Model Comparison (coloured by property)

The blade section refined mesh FE model is compared with the shaker experiment mode shapes in Figure 3.15, and the mode frequencies are also compared in Figure 3.15b. It appears that mode correlation with the shaker test does is worse that the previous model iteration of the TE-Taper with the reference 100 mm mesh. This is particularly evident for shaker test mode 3 where the correlation dropped from 0.8 to 0.65. Examining the mode frequencies of the refined mesh FE model shows a small increase across the first 10 modes, likely representing an increase in the shell stiffness.

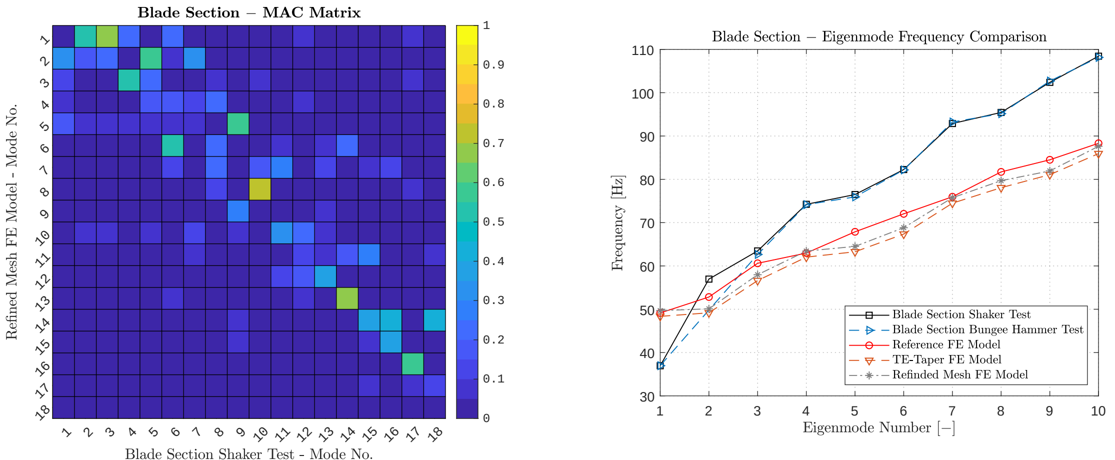

(a) Blade Section Refined Mesh - Shaker Test Modal Correlation

(b) Eigenmode Frequency Comparison Refined Mesh FE Model

Figure 3.15: Blade Section Trailing Edge Taper Model Modal Comparison

To show exactly the significance of the change in mode shape relative the previous model iteration the MAC matrix between the Refined Mesh and TE-Taper models is plotted in Figure 3.16. The correlation shows almost no affect to the mode order however, modes 1 and 2 of the model do appear to have had a change in mode shape. This is consistent with the reduced shape correlation with shaker test modes 2 and 3.

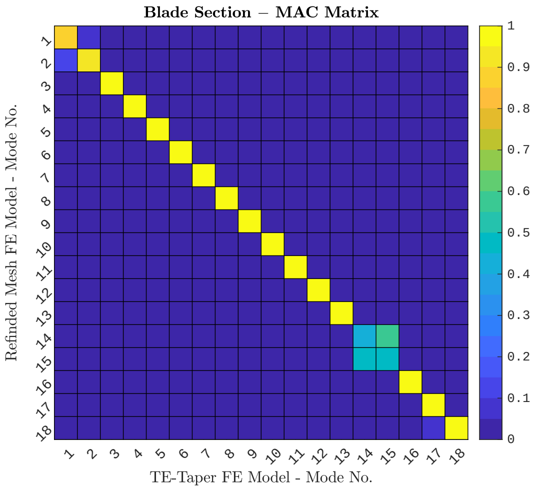

Figure 3.16: Blade Section Refined Mesh - TE-Taper FE Model Modal Correlation

It is therefore evident the refined mesh mostly affected the frequency of the FE modes, and also had a specific affect on the shape of FE modes 1 and 2, corresponding to the second breathing mode of the shaker test. This result was unexpected as the reduced element size was believed to have reduced the shell stiffness according to typical convention. The confounding variable of this is mesh distortion of the leading edge shell in the reference FE model previously shown in Figure 3.14a. As a result its unclear if the cause of the FE mode 1 shape change is result of mesh size, or the removal of the mesh distortion. Considering this, the refined mesh ultimately better reflects the structure due to the improved mesh uniformity, however it is likely the increased element aspect ratio resulted the small increase in the stiffness. Ultimately this refinement of the mesh failed to precipitate out the first breathing mode of the blade section.

3.2.4. Spar Glue Joint Mesh

Analogous to how the trailing edge core taper locally affected the bending stiffness around the panel boundary, the spar glue joint mesh is examined for its effect on the panel boundary stiffness. The reference model spar glue joints use a single element through the thickness to connect the spar web to the pressure and suction side shells. This coarseness of the glue mesh may have a stiffening affect on the panel boundary. Therefore to determine the effect of the element density on the modal behaviour of the blade section, the number of *CHEXA* elements in the spar glue joint is varied. Starting from one element as present in the reference model, up to four elements in the thickness where each model is evaluated and compared with each other. The generated meshes of the spar glue joint FE models are depicted in Figure 3.17.

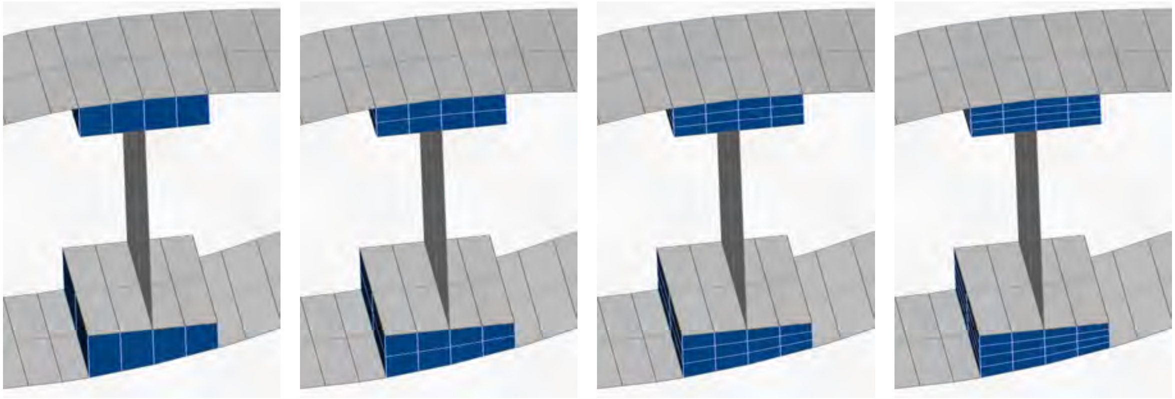

(a) Spar Glue Joint 1 Thickness Element

(b) Spar Glue Joint 2 Thickness Elements

(c) Spar Glue Joint 3 Thickness Elements

(d) Spar Glue Joint 4 Thickness Elements

Figure 3.17: Blade Section Spar Glue Joint Mesh Models

These four models are subject to a free-free modal analysis and the MAC matrix for each model with the shaker test modal model are plotted in Figure 3.18. Comparing the different spar glue mesh thickness element models relative the shaker test shows no measurable difference in mode shape or order between them.

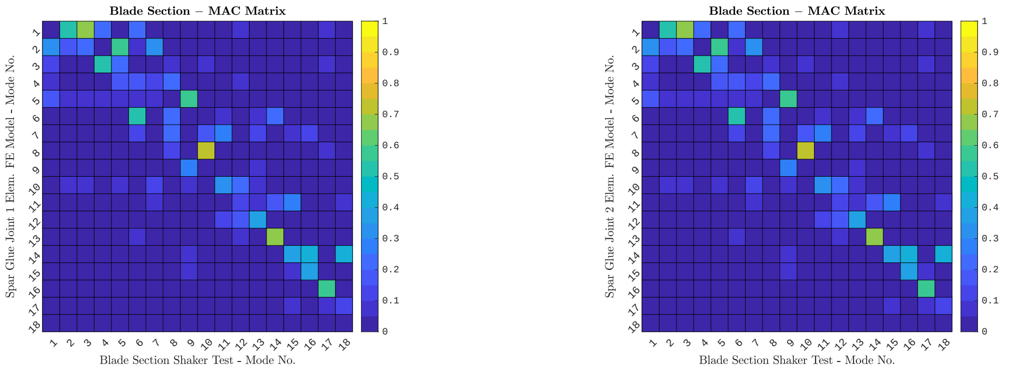

(a) Spar Glue Joint 1 Thickness Elements - Shaker Test Correlation

(b) Spar Glue Joint 2 Thickness Elements - Shaker Test MAC Matrix

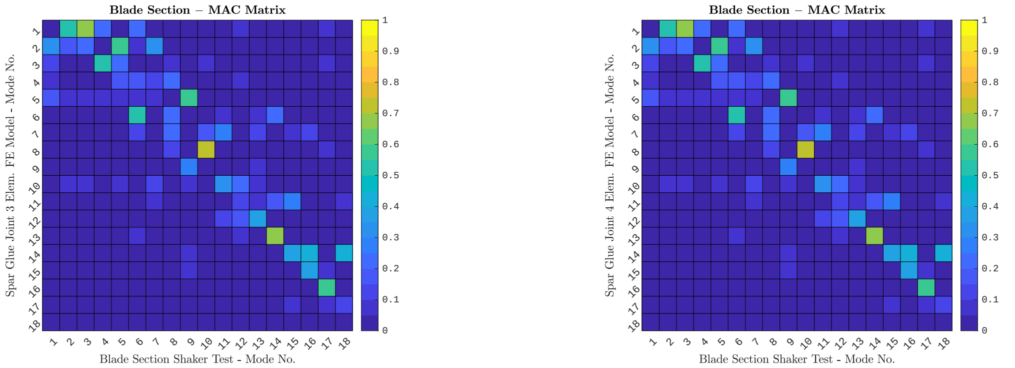

(c) Spar Glue Joint 3 Thickness Elements - Shaker Test MAC Matrix

(d) Spar Glue Joint 4 Thickness Elements - Shaker Test MAC Matrix

Figure 3.18: Blade Section Spar Glue Joint Mesh FE Models Shaker Test Mode Shape Correlation

The determine the affect on mode frequency the four spar glue joint mesh models are compared with each other in Figure 3.19. Similarly to the results of the mode shapes there is no difference in the mode frequencies between the models. It is then evident that the element size on the glue joints has little relation to the numerical stiffness in the context of the finite element model modal behaviour. For this reason additional elements here provide no improvement, therefore for other models of the blade section 2 elements in the thickness are used as they have the most ideal aspect ratios.

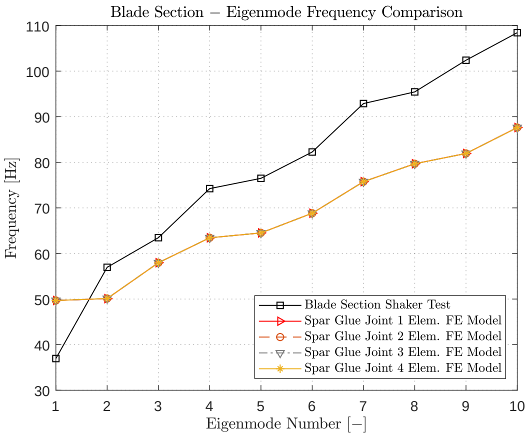

Figure 3.19: Blade Section Spar Glue Joint Mesh FE Models Eigenmode Frequency Comparison

3.2.5. Updated Geometry

The refined mesh model of Section 3.2.3 was generated by splitting elements along their chord-wise direction because no model geometry was available to make more extensive changes to the mesh. As a result of this the refined mesh still reflected the same geometry points of the reference model. To ensure the curvature in the panels was reflected in the mesh nodes, an interpolated surface geometry was generated using tools in FEMAP from the finite element nodes of the reference model. The split nodes of the refined mesh were then projected onto this surface for an improved approximation of the shell geometry. A comparison of reference and updated finite element mesh geometry is shown in Figure 3.20.

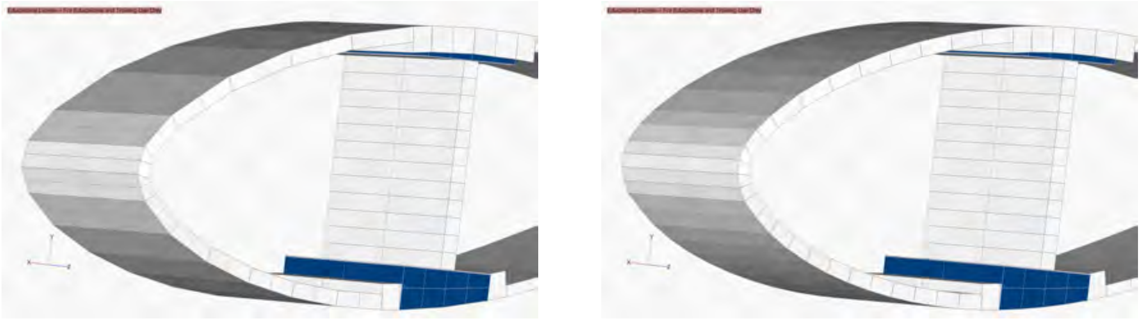

(a) Reference Mesh Geometry

(b) Updated Mesh Geometry using Interpolated Surface

Figure 3.20: Blade Section Updated Geometry Model Mesh Comparison

To determine the affect of the updated geometry on the model the original and updated geometries are correlated with the shaker experiment and the MAC Matrix is plotted in Figure 3.21. The mode shape correlation with the shaker test for the two models shows no noticeable differences between them either in MAC value or mode order.

To better quantify the affect of the changed changed geometry the reference and updated mesh geometries are compared directly with a MAC matrix plotted in Figure 3.22a. The correlation between the two models is nearly identity, illustrating the change of the refined mesh node positions to match the interpolated surface showed no change to mode order to mode shape. The mode frequencies are also compared with each other for the reference and updated geometry FE Models in Figure 3.22b. Similar to the mode shape and order, the frequencies for the updated geometry are almost unchanged relative the reference geometry.

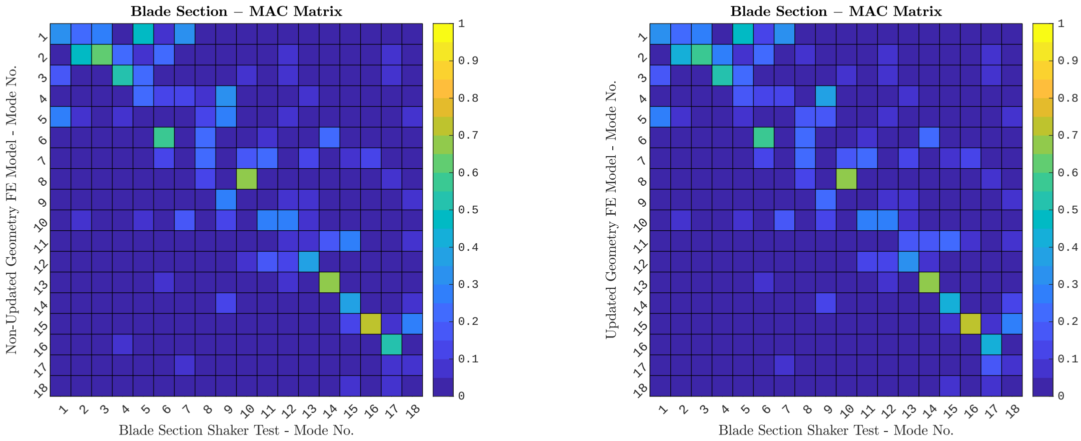

(a) Reference Mesh Geometry - Shaker Test MAC Matrix

(b) Updated Mesh Geometry - Shaker Test MAC Matrix

Figure 3.21: Blade Section Reference and Updated Mesh Geometry Mode Shape Correlation

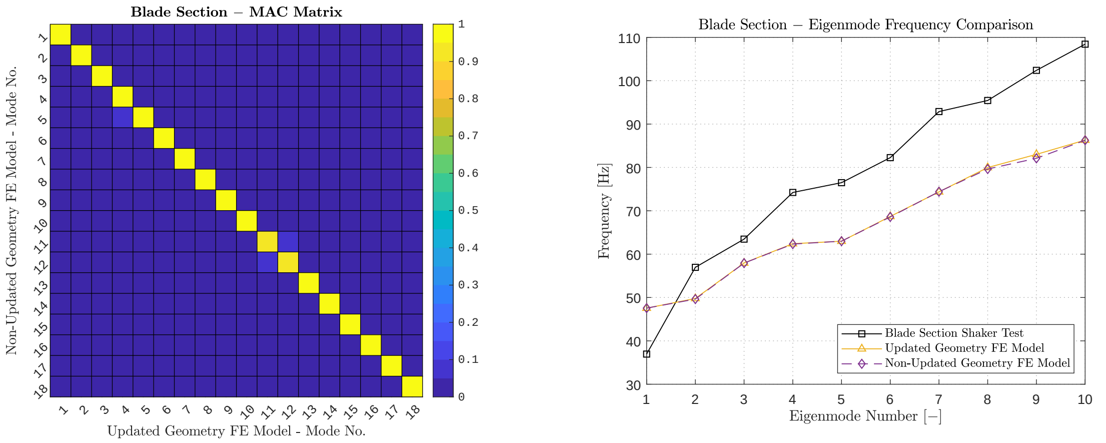

(a) Updated and Reference Mesh Geometry MAC Matrix

(b) Updated Mesh Geometry Eigenmode Frequency Comparison

Figure 3.22: Blade Section Updated Mesh Geometry Model Comparison

In addition to the interpolated geometry a true 3D scanned shape of the blade is also available. The scanned surface is shown compared with the updated finite element geometry in Figure 3.23. The wet surface shapes are extremely close, and considering the negligible change of result with the interpolated geometry it can be concluded that the shape of the panels is not a factor for predicting the first breathing mode of the blade section.

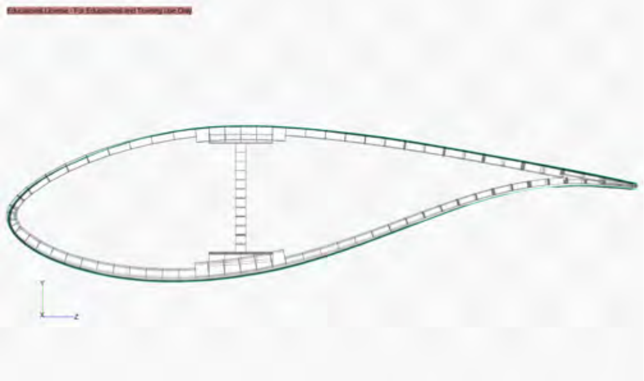

Figure 3.23: Blade Section 3D scanned surface and updated geometry model

3.2.6. Boundary Condition Approximation

The shaker modal test was connected directly with load straps to the testing gantry along the wet surface as shown in Figure 3.24b. As discussed in Section 3.1.1, it was considered that the strap suspension may have an effect on the modal results due to interference with the rigid body modes. The subsequent test using bungee cable suspension to validate the original test is discussed in Section 3.1.2.

A study was made to try and replicate the boundary conditions of the load straps of the shaker test in finite element to understand if it may have contributed to the presence of the first breathing mode. This was accomplished by using *CBUSH* elements which are generalised spring and damper elements [37]. The elements were oriented orthogonally to the surface of the panels along the approximate contact surface of the strap in the experiment, this is shown in Figure 3.24a. These elements were then given a stiffness along the surface orthogonal direction to approximate the behaviour the strap has on the out of plane motion of the panels.

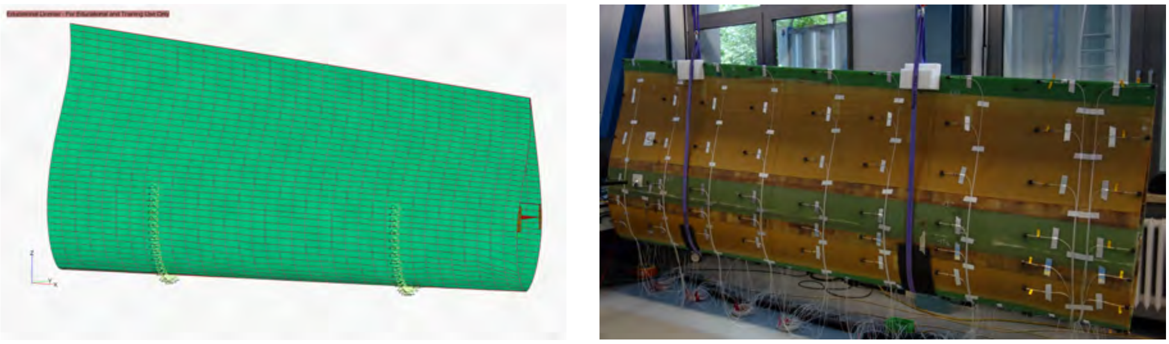

(a) Reference FE Model Pressure Side Mesh

(b) Blade Section Shaker Test Suspension

Figure 3.24: Blade Section Boundary Condition

Several models were made generated with increasing stiffness from 0 N/mm up to 250 N/mm, beyond this stiffness the rigid body modes began to couple with the elastic modes and were not comparable. The elastic mode frequencies of the models are compared in Figure 3.25b.

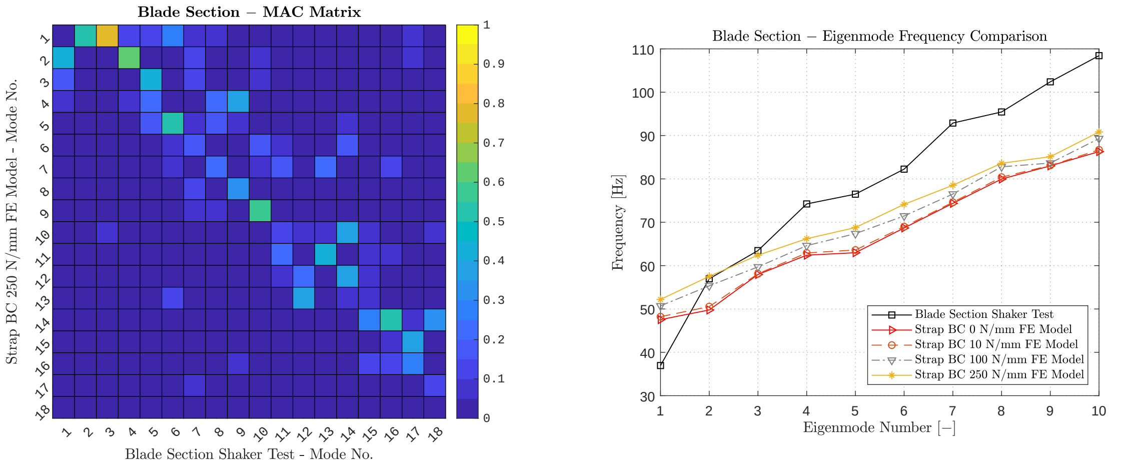

(a) 250 N/mm Stiffness Strap Model - Shaker Test Correlation

(b) Shaker Strap Stiffness Models Eigenmode Frequency Comparison

Figure 3.25: Blade Section Boundary Condition Model Comparison

For increasing stiffness of the *CBUSH* elements the mode frequencies of the model increased significantly. The higher stiffness models actually match closely the measured mode frequencies of the shaker test.

The highest stiffness model of 250 N/mm was correlated with the shaker test modal model in Figure 3.25a. Interesting is that the FE elastic modes 1 and 2 improved in correlation with the shaker test modes 3 and 4. However no significant correlation with the first breathing mode is achieved with the inclusion of the strap stiffness approximation.

This result served as justification for the blade section bungee hammer test, to validate the shaker test results by removing the influence of strap contact on the trailing edge panels. The bungee test is discussed in Section 3.1, and the result strongly validated the original shaker test modes. Therefore, the imposed boundary condition of the strap, approximated with *CBUSH* elements, artificially improved results and did not reflect the true behaviour of the blade section.

3.2.7. Leading Edge Joint

One major component of the blade section which was omitted in the reference model was the leading edge glue joint. To understand its potential effect on the modal results a variation of the joint is implemented into the finite element model of the blade section. This finite element model is built over the updated geometry model discussed in Section 3.2.5. Unlike the other glue joints no natural break in the geometry exists at the leading edge making it more difficult to create a glue joint using continuum elements. Therefore the it is implemented using an alternative method where the shell elements are updated with properties to approximate the laminates in joint.

To achieve the approximation of the leading edge joint, it is split into 4 distinct property regions. The suction side and pressure side core taper regions, the suction side region with no core material, and the lap joint area. The taper property regions approximate taper with half thickness, the no core region is a small area before the lap joint on the suction side with no core material. The lap joint consists of the suction and pressure side laminates with a 5 mm glue laminate layer between them. The 5 mm glue thickness is based upon measurements of the blade section test article. A comparison of the original, updated, and blade section leading edge joints are depicted in Figure 3.26.

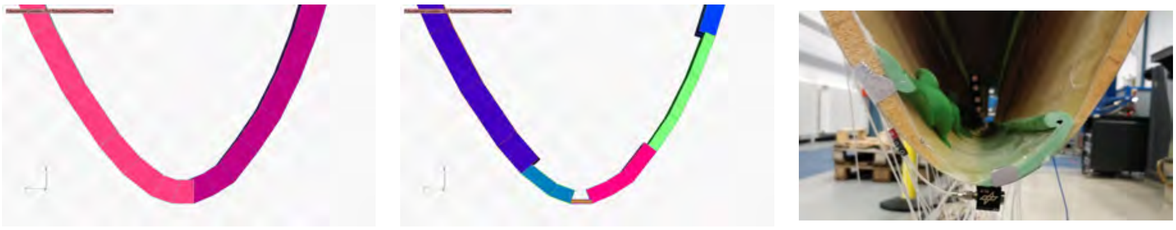

(a) Reference FE Model Leading Edge Joint

(b) Leading Edge Joint FE Model

(c) Blade Section Leading Edge Joint

Figure 3.26: Blade Section Leading Edge Joint Comparison

The new model, referred to as *Leading Edge Joint FE Model*, is subject to a free-free modal analysis and is compared with the shaker test modal model in the MAC Matrix plotted in Figure 3.27a. There is no significant difference in the modal correlation or mode order for the lower frequency modes relative the updated geometry model of Figure 3.21b.

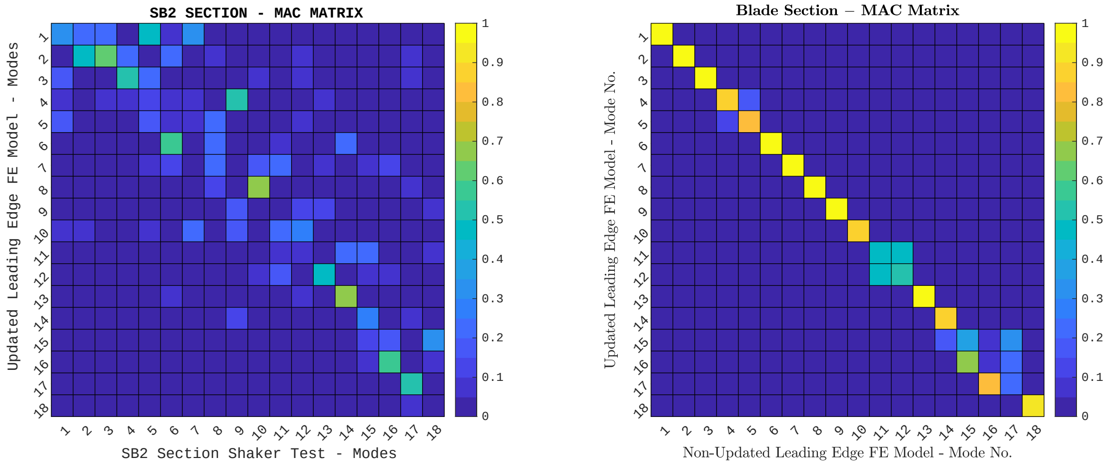

(a) Blade Section Leading Edge Joint FE Model - Shaker Test MAC Matrix

(b) Updated and Non-Updated Leading Edge Joint FE Model MAC Matrix

Figure 3.27: Blade Section Leading Edge Joint FE Model Modal Comparison

To better show the difference between the model with and without the updated leading edge joint the two FE models are correlated with each other in the MAC matrix in Figure 3.27b. The MAC values are consistent with the previous observation of insignificant change in the low frequency mode shapes and order. The higher frequency modes of the leading edge model are significantly different in shape and order which signifies observable changes in the model however, there remains no significant correlation for the first breathing mode.

The mode frequencies for the leading edge joint FE model are compared with the previous models in Figure 3.28. The leading edge joint model expectedly is more compliant with reduced frequencies relative to the updated geometry model, but the difference is small. The first mode shifted lower in frequency that other models, following more closely to the first breathing mode of the shaker test. However this first FE mode doesn't correlate well with the first breathing mode of the shaker test so the comparison isn't entirely accurate.

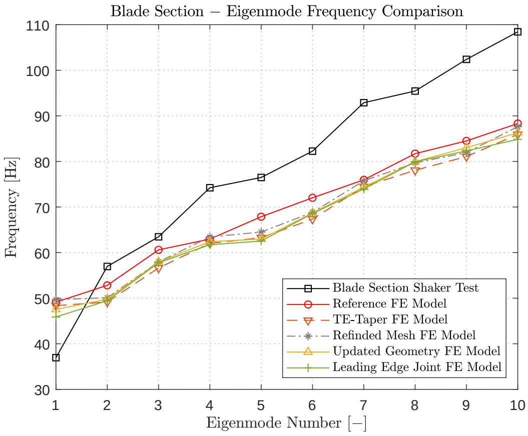

Figure 3.28: Leading Edge Joint FE Model Eigenmode Frequency Comparison

The leading edge joint FE model ultimately better approximates the structure of the blade section from a physical stand point. However this does not translate into any significant improved correlation with the shaker test modal model, and still failed to predict any mode similar to that of the first breathing mode.

3.2.8. Trailing Edge Joint Length

The design length of the trailing edge glue joint is a minimum of 70 mm, however the tolerance ranges all the way up to 90 mm. The average length measured on the blade section is 84 mm, a significant difference. Therefore to better reflect the produced structure the previous finite element model (*Leading Edge Joint FE Model*), is updated to include an additional 15 mm of trailing edge glue joint. This is achieved via an extra chord-wise continuum element for an average glue length of 85 mm in the finite element model, known as *Trailing Edge Glue Joint FE Model*. A comparison of the previous, ppdated, and blade section trailing edge glue joint is shown in Figure 3.29.

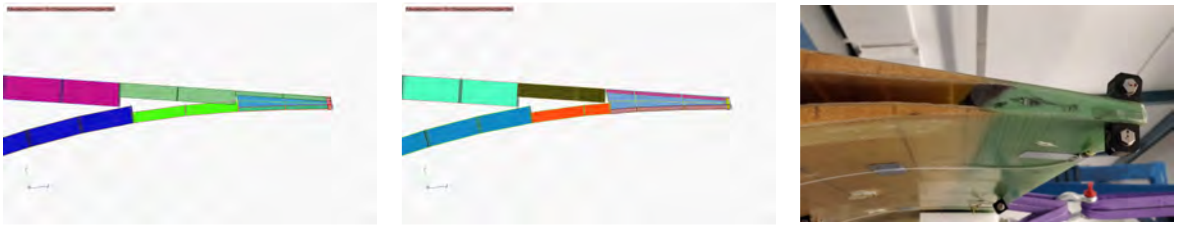

(a) Trailing Edge Taper FE Model

(b) Updated Trailing Edge Glue Joint FE Model

(c) Blade Section Trailing Edge

Figure 3.29: Blade Section Trailing Edge Glue Joint Comparison

The updated trailing edge glue joint FE model is subject to a free-free modal analysis and is correlated against the shaker test in the MAC matrix plotted in Figure 3.30a. Correlation with the shaker test shows an improvement in MAC value for the second, third, fourth, and sixth shaker test modes. Additionally, there are also some mode order changes for the mid to high frequency modes.

To better understand the affect of changing the trailing edge glue length, the updated model is correlated with the previous model shown in the MAC matrix of Figure 3.30b. The comparison confirms the previous observation with some changes in FE mode shape for the lower frequencies, and significant changes in shape for the mid frequency modes. There are also minor changes in mode order for the mid to high frequency modes.

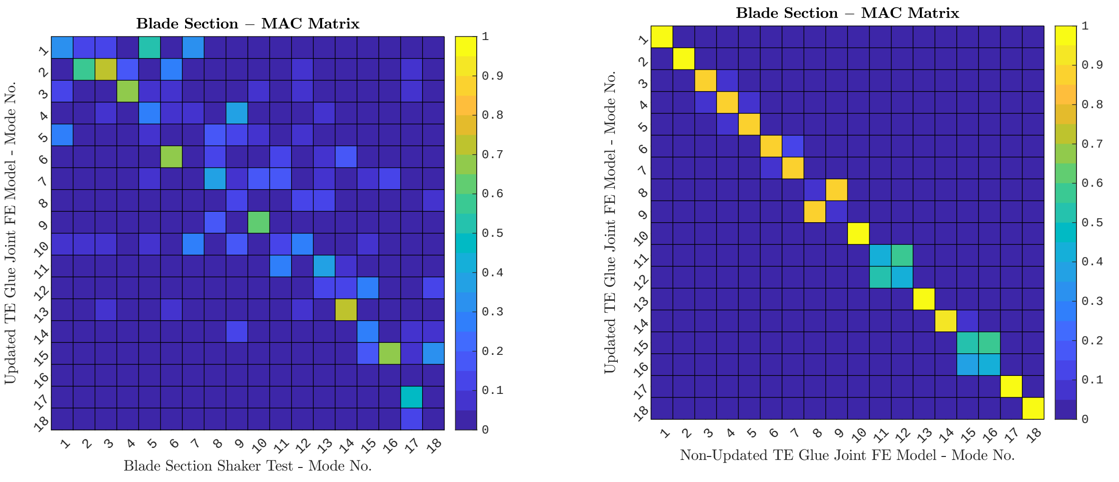

(a) Blade Section Trailing Edge Glue Joint FE Model - Shaker Test MAC Matrix

(b) Updated and Non-Updated Trailing Edge Glue Joint FE Models MAC Matrix

Figure 3.30: Blade Section Trailing Edge Glue Joint Modal Correlation

A comparison of the eigenmode frequencies with previous models is presented in Figure 3.31. A considerable increase in mode frequencies is observed relative the previous model iterations, which more closely matches the measured frequency behaviour. This represents an increased stiffness of the panel boundary contrary to what the previous model improvements have shown.

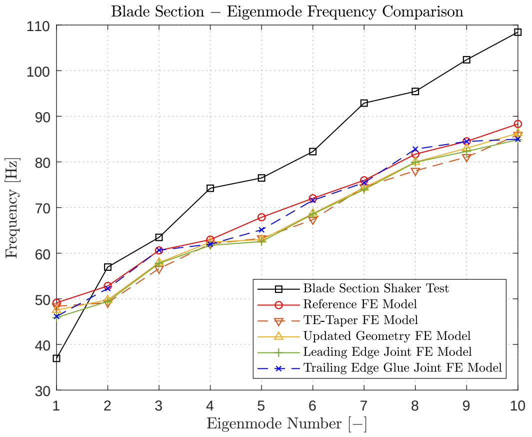

Figure 3.31: Trailing Edge Glue Joint FE Model Eigenmode Frequency Comparison

Considering improved mode shape correlation with the experiment, and frequency behaviour which more closely matches the shaker test the adjustment of the trailing edge glue joint has largely showed positive results. This reaffirms the hypothesis that modelling of the panel boundaries accurately is critical to more closely matching the panel behaviour. However, while this change yielded improvement it failed to identify the first breathing mode of the shaker test.

3.2.9. Suction Side Glue Joint

The finite element model of the blade section included a large thickness glue joint on the suction side, which is not representative of the prototype blade where the spar web is directly laminated on the spar cap. To better reflect the true nature of the spar web glue joint the glue elements on this side are removed and the spar web is extended and merged with the nodes of the spar cap in the suction side shell. This model change is built upon the previous model iteration with the lengthened trailing edge glue joint. A comparison of the suction side glue joint in the previous model, updated model, and the blade section are shown in Figure 3.32.

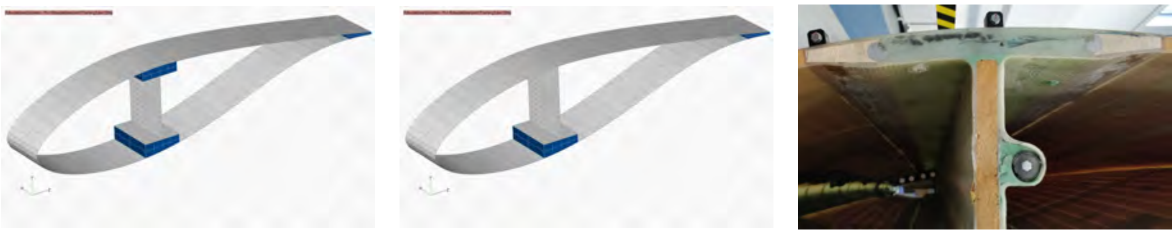

(a) Previous FE Model Spar Web Glue Joints (b) Updated Suction Side Spar Web Glue Joints (c) Blade Section Suction Side Spar Web Glue Joint

Figure 3.32: Blade Section Spar Web Suction Side Glue Joint Comparison

The updated model, herein referred to as *SS Spar Joint Merge*, is subject to a free-free modal analysis and is correlated with the shaker test in Figure 3.33a. The removal of the glue element has had a clear affect on the correlation with reduced MAC values for most the shaker test modes 2,3,4, and 6. Additionally the mode order appears to have changed as well for mid to high frequency modes. This mode shape and order change is also clearly demonstrated by correlating the previous model with the new suction side glue joint in the MAC Matrix plotted in Figure 3.33. The new joint has a very noticeable affect on the mode shapes with lower MAC values of 0.8 for the first two FE modes, where the highest correlations with apparent breathing modes of the shaker test are.

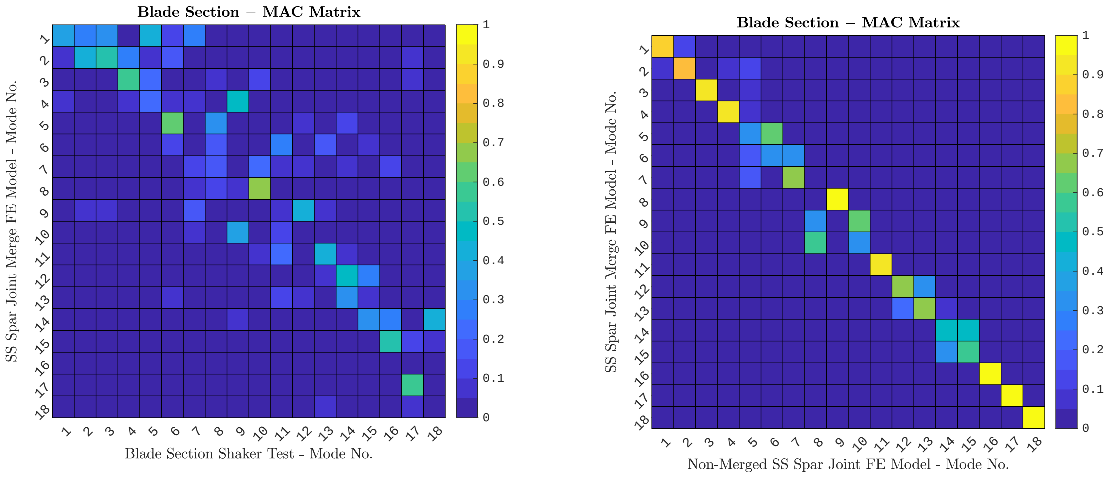

(a) Blade Section Suction Side Spar Joint Merge FE Model - Shaker Test MAC Matrix

(b) Previous and Merged Suction Side Spar Joint FE Models MAC Matrix

Figure 3.33: Blade Section Suction Side Spar Joint Merge Modal Comparison

The mode frequencies of the suction side spar joint merge model are compared with previous models in Figure 3.34. The frequency comparison show a consistent increase in frequency for the first 10 modes. This more closely approximates the shaker test mode frequencies, particularly for FE modes two and three. However, the divergence in frequency for the higher number modes with the experimentally determines ones is still present.

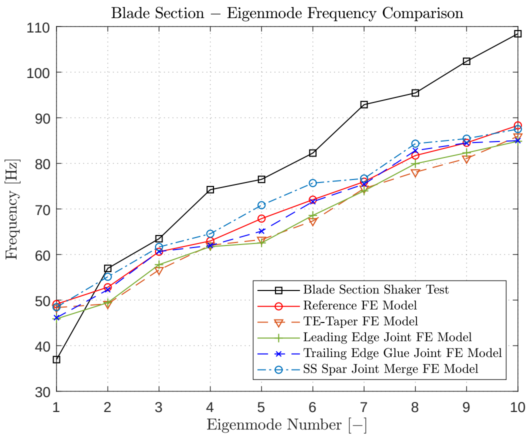

Figure 3.34: Suction Side Spar Joint FE Model Mode Frequency Comparison

The merging the nodes of the spar web with the suction side shell, the rotational degree of freedom between them is fixed which represents a very high stiffness joint. In addition to this change of joint stiffness, the removal of the glue element resulted in a mass change of the blade section which may have also contributed to the higher frequency modes. This results in mode shapes correlations which suggest that the joint stiffness is too high with poor correlation of the second breathing modes. Alternatively the mode frequencies show a result where the finite element modes are still too low in frequency relative the shaker test results.

It is therefore difficult to determine if merging of the joint resulted in an improvement or regression in the finite element model behaviour relative the test results. Ultimately, the result of this topological change is inconclusive. However, the presence of a high thickness glue joint that is not actually physically present in the test article is not an appropriate method to estimate the joint stiffness. For this reason for the future model iterations, the merged glue joint is used as it is the most appropriate representation available for the suction side spar web connection.

3.2.10. Spar Cap Balsa Flanks

Adjacent to the spar caps on both sides of the blade section are tapering regions with balsa core material. These are intended to serve as a thickness transition between the spar caps and the panel core materials. These are not considered in the reference model, therefore they are implemented to better represent the structure. It is hypothesised that the higher transverse shear stiffness of the balsa would change the response of the panels as they are adjacent to the spar glue joint panel boundary.

The design specified a balsa flank transition width of 67 mm, it was measured on the test section to be approximately 75–80 mm. To model the balsa flanks they are implemented to have the same core thickness as the adjacent foam core as the taper isn't significant. They are created with an average width of 80 mm to match the measurements on the blade section. A comparison of the property regions of the previous configuration, updated balsa flank model, and the blade section is show in Figure 3.35.

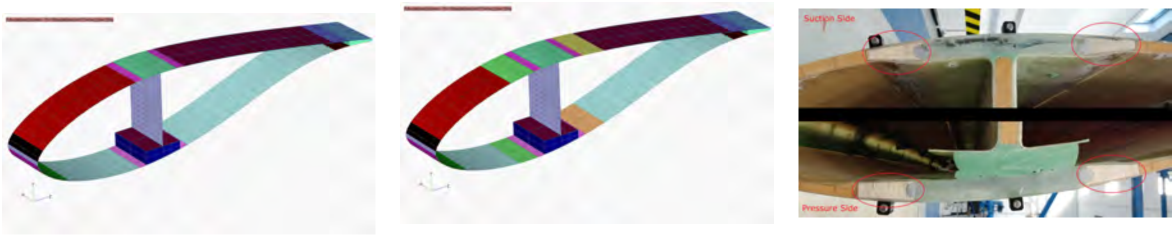

(a) Previous Model Cross-section Properties

(b) Balsa Spar Flanks FE Model Cross-section Properties

(c) Blade Section Spar Caps (Balsa Flanks Circled Red)

Figure 3.35: Blade Section Spar Cap Balsa Flank Area Comparison

The updated model, *Balsa Spar Flanks FE Model*, is subject to a free-free modal analysis and correlated with the shaker test with a MAC Matrix in Figure 3.36a. The MAC values with the shaker test show no significant changes over the suction side spar joint merge FE model. To illustrate the exact changes in mode shape the two models are compared in a MAC matrix in Figure 3.36b. The correlation MAC matrix shows nearly identity apart from some higher frequency modes with lower MAC values, but no mode order changes are observed.

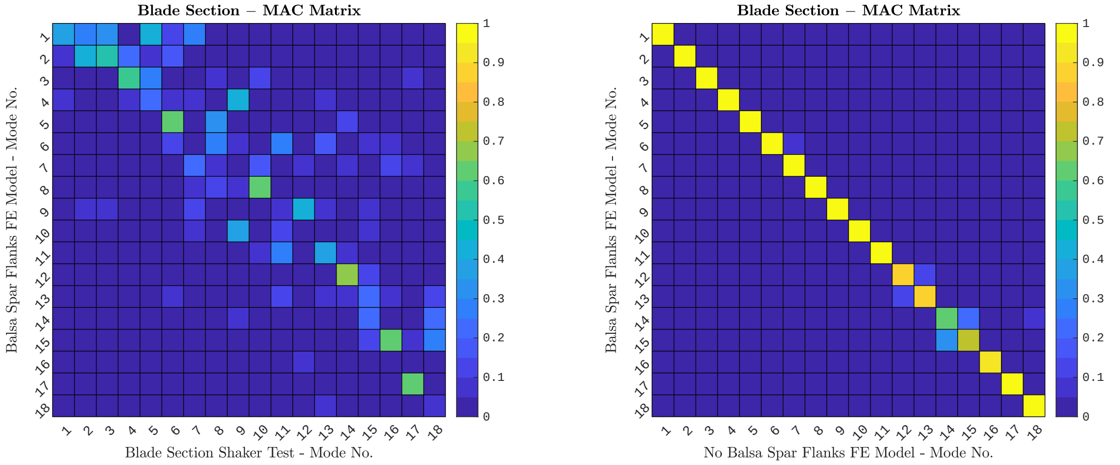

(a) Blade Section Balsa Spar Flanks FE Model - Shaker Test MAC Matrix

(b) Previous and Updated Balsa Spar Flanks FE Models MAC Matrix

Figure 3.36: Blade Section Balsa Spar Flanks FE Model Modal Comparison

To identify the effect on the mode frequencies the balsa spar flanks FE model is compared with previous models in Figure 3.37. The updated model shows a significant increase in frequency over the suction side joint merge model. This matches more closely with the experimentally measured frequencies of the shaker test for the lower frequency modes apart from the first breathing mode. The divergence in mode frequency also appears less significant than for previous models.

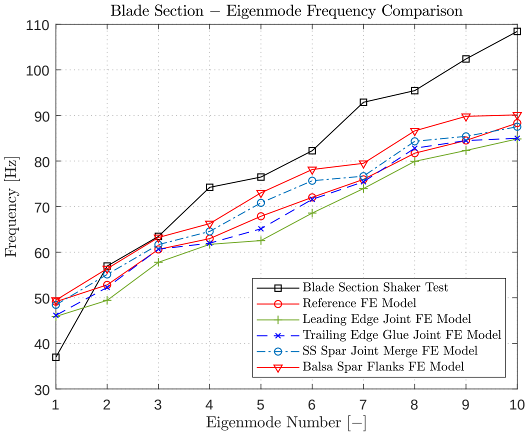

Figure 3.37: Balsa Spar Flanks FE Model Eigenmode Frequency Comparison

The inclusion of the balsa flank transition zone around the spar caps solely affected the frequency of the modal behaviour with stiffened behaviour near the panel boundary resulting in higher frequency modes. However, no effect on mode shape relevant to the breathing modes of the blade section was observed and it failed to predict a first breathing mode.

3.2.11. Spar Web Cable Mass

A notable element of the blade section which was not included in the reference model is that of the spar web lightning protection cable. The cable has an approximated mass of 1.765 kg/m with a diameter of 30 mm[28, 56], it is attached along the center of the spar web with glue and is reinforced with two additional layers of ±45° biaxial laminate. The effect of the cable is included in the finite element model using concentrated mass elements *CONM2* offset 30 mm from the mid-plane. The attachment plies are modelled as well with two additional plies of 2AX45 to the spar web laminate. It is thought that the increased stiffness of the reinforcement plies on the spar web and new distributed mass may have an effect on the mode frequencies. A comparison of the previous balsa flank model iteration, the new spar-web with concentrated masses, and the blade section is shown in Figure 3.38.

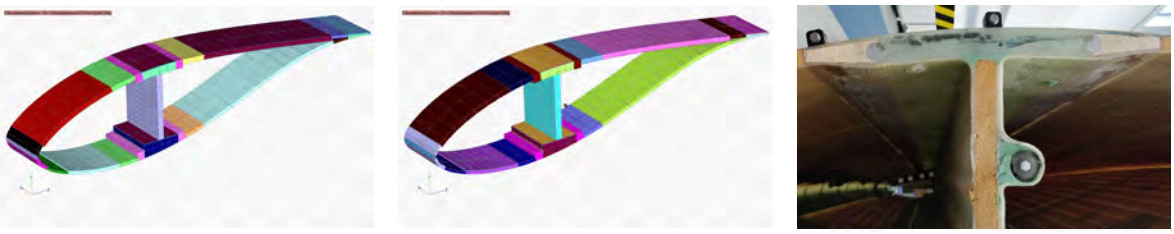

(a) Balsa Flank FE Model Cross-section (b) Spar Web Cable FE Model Cross-section (c) Blade Section Spar Web Cable

Figure 3.38: Blade Section Spar Web Cable Model Comparison

The updated *Spar Web Cable FE Model*, is subject to a free-free modal analysis and correlated with the shaker test in Figure 3.39a. The MAC values showed no significant changes relative the balsa spar flanks model for the low frequency breathing modes. The only notable difference is an improved MAC value for shaker mode 14. The spar web cable model is correlated with the previous model iteration in the MAC Matrix of Figure 3.39b. Comparing the two FE models there is no significant change in the mode shapes for the low frequency modes, and small changes in mode shape and order for the higher frequency modes.

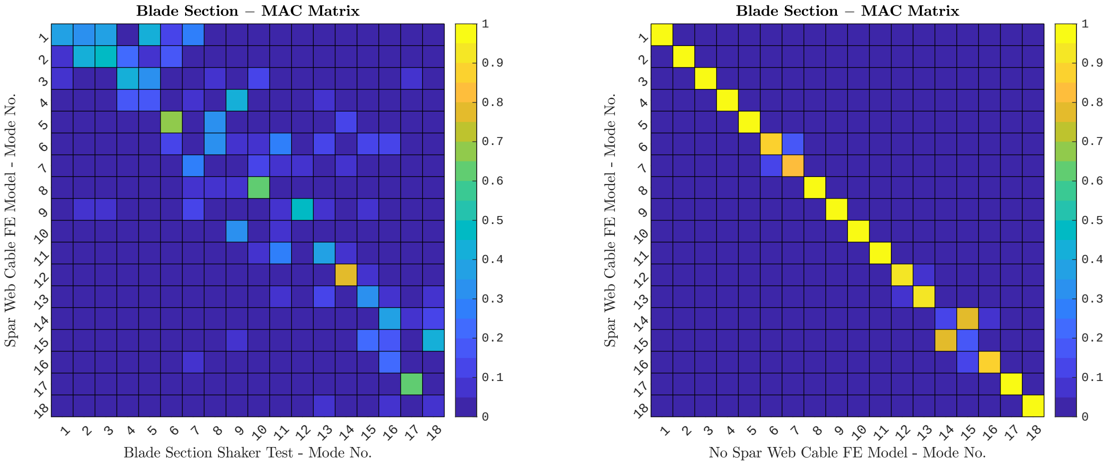

(a) Blade Section Spar Web Cable FE Model - Shaker Test MAC Matrix (b) Previous and Updated Spar Web Cable FE Models MAC Matrix

Figure 3.39: Blade Section Spar Web Cable FE Model Modal Comparison

The mode frequencies for the spar web cable model are compared with previous model in Figure 3.40. The mode frequencies for the spar web cable model are higher than the previous balsa flank model and match more closely with the experiment than any previous model. The divergence for the higher frequency modes is still evident to a lesser extent than before.

The inclusion of the cable mass and attachment plies resulted in no significant changes in terms of the breathing mode shape, and failed to show the first breathing mode. This was expected as the change has little interaction with the motion of the panels which dominate the modal behaviour. The additional cable attachment plies increased the stiffness of the spar web and therefore spar web joint, this likely caused the increased mode frequencies.

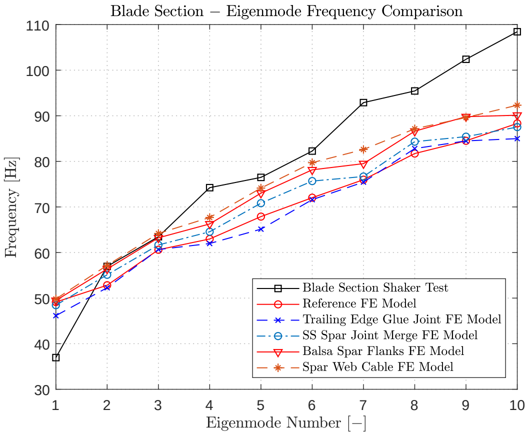

Figure 3.40: Spar Web Cable FE Model Eigenmode Frequency Comparison

3.2.12. Pressure Side Glue Joint

The last topological change explored for the blade section model concerns the glue joint connecting the spar web on the pressure side. The test article has an average glue joint thickness of 24.4 mm at the tip and 30.36 mm at the root, with an approximately constant thickness along the width. The reference FE model implementation of this joint has varying thickness across the width and overestimates the average glue thickness, with 30.5 mm at the tip and 43.5 mm at the root.

This overestimated glue joint thickness is likely to result in lower stiffness than the true behaviour of the glue joint. Therefore the pressure side glue joint is modified to match the measured glue thickness values. This is achieved by interpolating the pressure side spar cap elements into a surface using FEMAP tools, which is then offset and rotated to approximate the measured glue thickness. The nodes of the spar web flange are then projected onto this offset surface, and the *CHEXA* glue elements are created in the space between the pressure side shell and the spar web flange. The revised joint has an average thickness of 25.0 mm at the tip, and 29.6 mm at the root which is a much closer approximation of the structure. The previous and updated versions of the pressure side glue joint are compared with the test article in Figure 3.41.

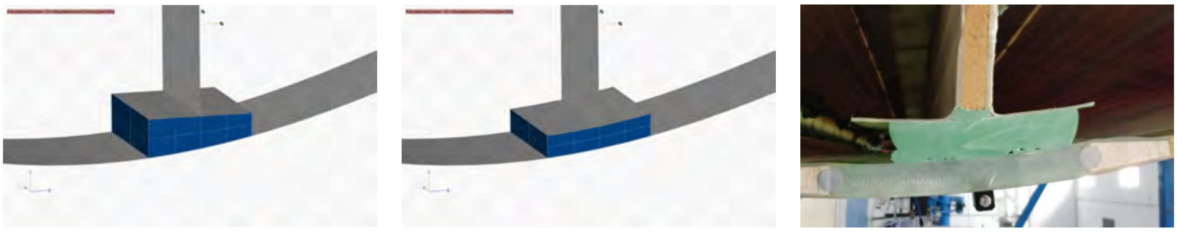

(a) Previous FE Model Pressure Side Glue Joint (b) Updated Pressure Side Glue Joint FE Model (c) Blade Section Pressure Side Glue Joint

Figure 3.41: Blade Section Pressure Side Glue Joint Model Comparison

The modified *Pressure Side Glue Joint FE Model* is subject to a free-free modal analysis and is correlated with the shaker test plotted in a MAC matrix in Figure 3.42a. Relative to the previous spar web cable model, a marginal improvement in MAC value is observed for shaker modes 2, 3, and 6 the remaining modes are unchanged. The model is also correlated with the spar web cable FE model directly in the MAX matrix of Figure 3.42b. The FE mode shape correlation is consistent with the shaker test correlation, showing marginal changes in MAC value and no change in the mode order.

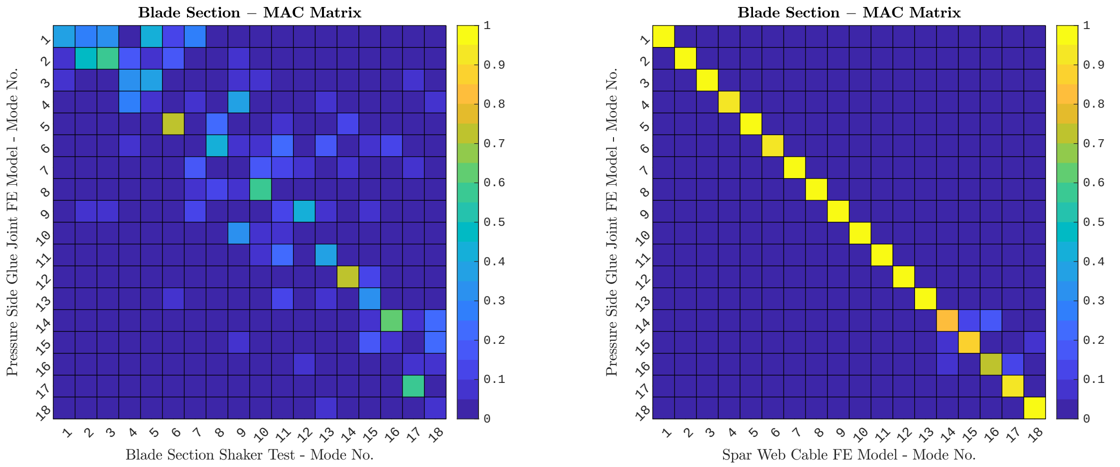

(a) Blade Section Pressure Side Glue Joint FE Model - Shaker Test MAC Matrix (b) Previous and Updated Pressure Side Glue Joint FE Models MAC Matrix

Figure 3.42: Blade Section Pressure Side Glue Joint FE Model Modal Comparison

The mode frequencies for the pressure side glue joint FE model are compared with previous models in Figure 3.43. The mode frequencies from the pressure side glue joint show little difference to the spar web glue joint model, with on average a marginal frequency increase.

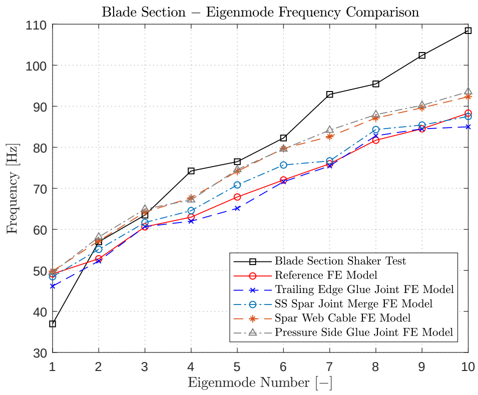

Figure 3.43: Pressure Side Glue Joint FE Model Eigenmode Frequency Comparison

The modification of the pressure side glue joint showed very subtle change relative to the spar web cable model. The predominant change was a small increase in frequency which can be attributed to the lower thickness glue joint which possess an increased stiffness. The modification of the pressure side glue joint ultimately failed to predict the first breathing mode, or improve mode shape identification in a meaningful way.

3.3. Blade Section Conclusion

The topological alterations applied to the blade section model were primarily focussed on the features which may precipitate the finding of the first breathing mode from the shaker test experiment. The findings of these topological alterations are summarised in Table 3.3. Ultimately, focussing only on topological changes failed to yield a significant correlation to the first breathing mode. While this may be the significant result of the work in improving the blade section model topology, several factors concerning the underlying model must be considered to put the result into context.

A significant feature omitted for all the examined finite element models was the ballast chamber at the tip side of the blade section in the leading edge compartment. The ballast chamber of the blade is used to balance the center of gravity to avoid excessive cyclic hub loads in operation, it can be seen in the tip of the blade section in Figure 3.44.

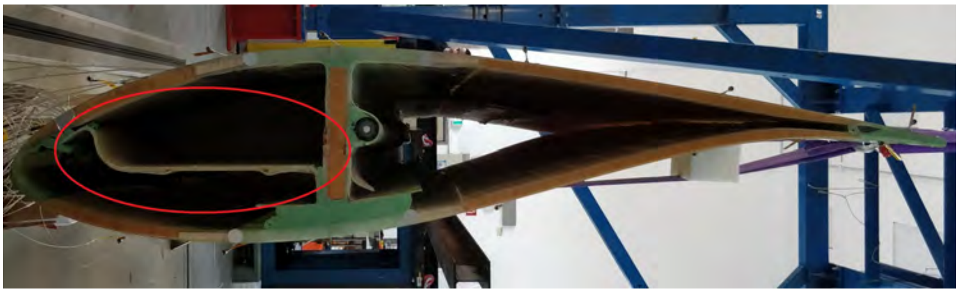

Figure 3.44: Blade Section Tip Ballast Chamber (Circled in Red)

The ballast chamber is a bespoke part for which no geometry or specifications were available. Due to this constraint it wasn't included in the finite element models. It is possible that this may have interacted negatively with the final results of the correlations. It should be considered that it is only in the leading edge compartment of the blade. Therefore its unlikely this would have had a great effect on the stiffness of the trailing edge panels and thus the prediction of the first breathing mode. Additionally, it is likely the ballast chamber would have the effect of increased stiffness for the spar web connection at the tip side. Its probable this may be the cause for the observed frequency divergence in the mode frequencies between the experiments and finite element models. Aside from the ballast chamber it is thought the final finite element model is a good topological approximation of the blade section based on the test article as well as the design drawings.

It is important to note the topological changes that had the most significant affect in the modal behaviour, as these are important to include for improved prediction of panel motion for complete wind turbine blades. With respect to trailing edge panel motion, the model changes focussed on the trailing edge glue joint and the connection with the spar effected the most significant changes in the predicted mode shape and frequency. Particularly inclusion of the core tapering showed in Section 3.2.2 and the alteration of the glue joint length in Section 3.2.8. As the trailing edge panel motion is sensitive to these features they should be considered more closely in future models and in blade manufacturing. It was seen that the design length of the joint and the measured length differed significantly, therefore for better prediction of the panel motion for future blades greater control of the length and thickness of this joint should be implemented to allow for improved analysis of the trailing edge panels.

The implementation of the spar glue joints also showed a great sensitivity to the motion of the trailing edge panels as shown in Section 3.2.9 and to a lesser extent in Sections 3.2.10 and 3.2.12. The modification of the glue joints showed that the glue thickness has a significant effect on the stiffness of the panel boundary, with a large increase in panel mode frequency with the merged suction side joint. The pressure side glue joint implementation while very close the real structure effected only a small change as the reference configuration was relatively close to the blade section already.

Throughout all of these topological modifications the mass of the modelled blade changed so it is important to understand the reasons for this. Table 3.2 shows the mass and center of gravity for the blade section test article, the reference model configuration, and the final model.

Table 3.2: Mass and Centre of Gravity for Prototype Blade Section

Blade Section	Mass [kg]	CoG X [mm]	CoG Y [mm]	CoG Z [mm]
Test Article	187	14087	-210.12	109.02
Reference Model	192.58	14139.46	-214.95	150.11
Final Model	176.66	14149	-221.82	153.77

The center of gravity between the models and the test article are fairly close however the mass of the final model of the blade section which best approximates the true structures is underweight by 10.34 kg or 5.53 % compared to the test article. This reduced weight is largely attributed to the changing of the spar glue joints as they largely overestimated the quantity of adhesive in the test section. Part of the missing mass can be attributed to the absence of the ballast chamber estimated to be 2.11 kg [28]. However this still leaves a significant amount of unaccounted for mass which is from an unknown source, possibly excess resin mass in the panels.

The topological changes to the blade section finite element models failed to yield a distinct first breathing mode despite an accurate representation. It is possible that this difference in behaviour is a result of inaccurate material properties, a conclusion consistent with the underestimated mass and difference in mode frequencies. Another possibility is that the element configurations used to model the panels as shells are inadequate to predict their modal behaviour. To investigate these possibilities, a sample plate using the same materials as the blade is tested in and compared with various finite element implementations in Chapter 4.

Table 3.3: Blade Section Topology Change and Effect Summary

Model Change	Effect
Trailing Edge Core Taper	Inclusion of core tapering along the trailing edge resulted in reduced frequencies for eigenmodes and significant mode shape changes over the reference model with small improvement in mode shape correlation with the experiment.
Mesh Refinement 50 mm	Re-meshing along the chord-wise direction showed a consistent increase in eigenmode frequencies and marginal change in mode shape correlation from the previous FE model.
Spar Glue Joint Mesh Elements	Increasing the number of thickness elements in the spar web glue joints showed no measurable change in eigenmode frequency or shape.
Geometry Correction	Projection of the remeshed nodes onto the blade curvature showed no change in frequency or mode shape over the previous model with nodes on element midpoints.
Boundary Condition Modelling	As examined in the experiment tests in Section 3.1 the sling suspension boundary conditions had no perceivable change to the modal response of the low frequency panel modes of the blade section.
Leading Edge Joint	Implementation of the leading edge joint via shell properties showed a significant reduction in the first mode frequency and small frequency reductions for other modes, the mode shapes showed change but the correlation with experiment did not improve.
Trailing Edge Joint Length	Extension of the trailing edge glue joint resulted in a significant increase in eigenmode frequency for all modes in addition to some mode order and shape changes resulting in an improved correlation with the experiment.
Suction Side Glue Joint	Removal of the suction side glue joint elements resulted in a significant increase of mode frequencies, changes to mode order, and reduced correlation with the experiment. This resulted in closer frequency matching to the experiment as a result of stiffer joint behaviour.
Spar Cap Balsa Flanks	Balsa flanks increased mode frequencies further matching more closely to the experiment with no perceivable change in mode shape, the correlation with experiment remained poor.
Spar Web Cable Masses	Inclusion of concentrated masses and attachment plies for the lightning cable showed small increase in mode frequency closer to the experiment, a result of increased joint stiffness. No significant change in mode shape was observed, with experiment correlation remaining poor.
Pressure Side Glue Joint	Correction of the pressure side glue joint thickness showed a marginal increase in mode frequencies with no change to the mode shapes, experimental correlation remained poor.

4

Model Element and Material Effects

In Chapter 3 the model topology of the blade section was studied to determine which model features contributed to prediction of the shaker test first breathing mode. The topological modifications of the model failed to predict this first mode, therefore a closer examination of the elements and material properties used for these models is examined.

To examine the element and material effects in a more controlled environment a sample plate which was manufactured from the same materials of the blade section is used. This sample plate is first subject to a modal test where the modal parameters are used for comparison with several finite element model implementations. The sample plate was also processed into test coupons and subject to three-point bending tests for comparison and estimation of material properties. These tests are discussed in Section 4.1. With test results available for comparison, finite element models of the plates examining element type and size as well as material properties are examined in Section 4.2.

4.1. Sample Plate Testing

To make an assessment of the influence of element type and material properties without consideration of the geometric complexity of the wind turbine blade, a sample plate with the same materials was manufactured. The plate was processed into a precise rectangular shape of 680 mm by 650 mm to remove the variability of geometry.

To make a comparison with the dynamic behaviour of the finite element model the plate is subjected to a modal test detailed in Section 4.1.2. As a result of the variability of the manufacturing process there is a difference in the estimated fibre volume content, and therefore predicted stiffness. To control for this additional factor three point bending tests are performed with nine coupons cut from the plate detailed in Section 4.1.4.

4.1.1. Geometry and Design

The sample plate was laminated with ±45° biaxial non-crimp fabric sheets aligned along the zero direction. This is same laminate described in Table 2.3 as ’2AX45’. The core material is the ’C70-55-20 mm’ perforated PVC foam core also described in Table 2.3. The plate was manufactured via the same resin vacuum infusion method as the blades with the same resin system. Even with the same manufacturing process, the vacuum infusion method resulted in different fibre volume content than was assumed in the blade. This can result in variations of the plate density and stiffness uniformly, and in local areas which affect the modal parameters of the sample plate.

To account for this variation of fibre volume content, the final plate is measured for its mass, and average thickness, these parameters are shown in Table 4.1. With the area, total mass, and thickness of the plate measured it is possible to estimate the fibre volume content using the parameters specified in the material data-sheets detailed in Tables 2.1 to 2.3.

Table 4.1: Sample Plate Measured Properties

m_{plate} [g]	t_{avg}[mm]	A_{plate} [m^2]
1715	21.0 ± 0.2	0.442

Using Equations (4.1) to (4.3) the mass breakdown between all three materials within the sample plate is estimated. Namely the total mass for foam, glass, and resin parts. The results of these calculations are shown in Table 4.2

$$m_{glass} = m'_{\mathrm{2AX45}} \cdot 2A_{plate} \tag{4.1}$$

$$m_{core} = \rho_{core(dry)} \cdot A_{plate} \cdot \left(t_{avg} - t_{core}\right) \tag{4.2}$$

$$m_{resin} = m_{plate} - m_{glass} - m_{core} \tag{4.3}$$

$$V_f = \frac{2m'_{\mathrm{2AX45}}}{\rho_{glass} \cdot \left(t_{avg} - t_{core}\right)} \tag{4.4}$$

$$m_{lam-resin} = \rho_{resin} \cdot \frac{m_{glass}}{\rho_{glass}} \cdot \frac{1 - V_f}{V_f} \tag{4.5}$$

$$m_{core-resin} = m_{resin} - m_{lamresin} \tag{4.6}$$

$$\rho_{lam} = \frac{m_{glass} + m_{lam-resin}}{A_{plate} \cdot \left(t_{avg} - t_{core}\right)} \tag{4.7}$$

$$\rho_{core(wet)} = \frac{m_{core} + m_{core-resin}}{A_{plate} \cdot t_{core}} \tag{4.8}$$

Table 4.2: Sample Plate Mass Properties

m_{glass} [g]	m_{core} [g]	m_{resin} [g]	m_{plate} [g]
716.04	530.4	468.56	1715

Using the previously specified masses for the resin, glass, and core, the fibre volume content can be calculated and density of the infused components estimated. It should be noted some of the resin is uptaken in the core material and not solely the face sheets. If the core and face sheets are assumed to be of constant thickness, the fibre volume fraction and adjusted wet densities of infused lamina can be estimated using Equations (4.4) to (4.8). The resulting infused set of mass properties for the sample plate are shown in Table 4.3.

Table 4.3: Sample Plate Estimated Properties

V_f	$m_{lam-resin}$ [g]	$m_{core-resin}$ [g]	ρ_{lam}[kg/m^3]	$\rho_{core(wet)}$[kg/m^3]
61.83%	185.62	282.94	2039.96	92.01

The assumption regarding constant thickness of the core and infused laminate are not entirely correct and ultimately drive the calculated fibre volume content. In reality the amount of resin uptake is dependant on the core material, amount of perforation, viscosity of the resin, and infusion time so it is difficult to estimate. In the sample plate the infusion time is very small and likely has less resin uptake compared to the wind turbine blade which underwent a longer infusion process. The full blade had different core material thicknesses, grooves and spaces to accommodate curvature, panel gaps, and perforations for infusion which results in much larger amounts of resin uptake, this is shown in the densities of the lamina shown in Table 2.3. In addition to just density affects, these resin filled areas of the blade core material can also increase the core material shear stiffness [15], which may affect the modal behaviour of the sandwich panels. While this has a measurable affect its very difficult to predict due to the non-uniform distribution of resin uptake, therefore this is not considered here.

The face sheet laminate of the sample plate is a non-crimp fabric, meaning the layers are placed unidirectionally and stitched together with a synthetic fibre. As the fabric is non woven the moduli of face sheets can be roughly approximated using the rule of mixtures to estimate the properties each unidirectional layer. The properties of the unidirectional layers are calculated with the rule of mixtures using Equations (4.9) to (4.12).

$$E_1 = E_{glass} \cdot V_f + E_{resin} \cdot \left(1 - V_f\right) \tag{4.9}$$

$$E_2 = \frac{E_{glass} \cdot E_{resin}}{E_{glass} \cdot \left(1 - V_f\right) + E_{resin} \cdot V_f} \tag{4.10}$$

$$G_{12} = \frac{G_{glass} \cdot G_{resin}}{G_{glass} \cdot \left(1 - V_f\right) + G_{resin} \cdot V_f} \tag{4.11}$$

$$\nu_{12} = \nu_{glass} \cdot V_f + \nu_{resin} \cdot \left(1 - V_f\right) \tag{4.12}$$

To create approximate laminate moduli for the complete fabric these properties must be applied using composite laminate theory. As the thickness of the face sheets are known and determined from the fibre volume content, the direction weights of the glass fabric can be used to determine the approximate thickness of each unidirectional layer in the fabric. For the ’2AX45’ laminate the directional weights are specified in Table 2.2, and each layer thickness is calculated by the ratio the directional weight over the total weight times the total laminate thickness as shown in Equation (4.13)

$$t_\theta = t_{lam} \cdot \left(\frac{m'_\theta}{m'_{2AX45}} \right) \tag{4.13}$$

Using the unidirectional layer moduli with the directions and thickness for each layer of the non-crimp fabric, composite laminate theory is applied to determine the effective moduli along the principal direction. The general method for this calculation is detailed in Appendix A. The effective laminate moduli are estimated from the a matrix to model purely the in-plane behaviour, the resulting parameters are shown in Table 4.4.

Table 4.4: Sample Plate Rule of Mixtures Estimated Laminate Properties

Materials (Plate)	Angle	E_1 [MPa]	E_2 [MPa]	G_{12} [MPa]	ν_{12}	V_f	t[mm]	ρ[kg/m^3]
2AX45	±45°	9066.22	8988.34	8213.28	0.5163	61.83%	0.500	2039.96
C70-55-20 mm	-	55	55	22	0.3	-	20	92.01

The properties estimated using rule of mixtures are significantly different than the reference properties of Table 2.3. It should be considered that the only material properties of the blade which were experimentally verified are that of the ’UD’ laminate, all other laminate moduli are approximated including the ’2AX45’ laminate used in the plate. The method used to predict the laminate properties in Table 2.3 is unknown, however they are inconsistent with the predictions using rule of mixtures as shown in Section 4.2.6. It should be noted that the rule of mixtures method is only an estimate and has difficulty modelling transverse and shear behaviour of unidirectional layers, therefore it is not necessarily more accurate than the reference properties.

4.1.2. Modal Tests

To characterise the dynamic behaviour of the a modal test of the sample plate is carried out. Due to the small size of the plate a roving hammer type test is used as it requires less setup. A 5x5 grid of excitation points was laid out to best identify the low frequency mode shapes, the grid points are located at the intersection points of the tape lines in Figure 4.1a. Three uniaxial accelerometers are used and attached at unique points by means of a 3M double sided tape on a threaded plastic base. The sensor unit mass was 5 g, which relative the total mass makes the added mass effect negligible. Initially, the test setup used 2 sensors however the estimated mode shapes this yielded were of low quality, therefore the additional third sensor was installed. A small modal hammer was used as the excitation device utilising a hard tip to excite the higher frequency ranges as the first plate modes were in the 100−400 Hz range.

With this setup two free-free configurations of the plate were tested, one on a soft foam placed underneath the plate shown in Figure 4.1a, and another suspended by bungee chords shown in Figure 4.1b. Initially the foam support was used as it was assumed the rigid body frequencies would be low enough not to interfere with the elastic modes. However the results showed unrealistically high damping values and therefore the second test with the bungee chords was conducted.

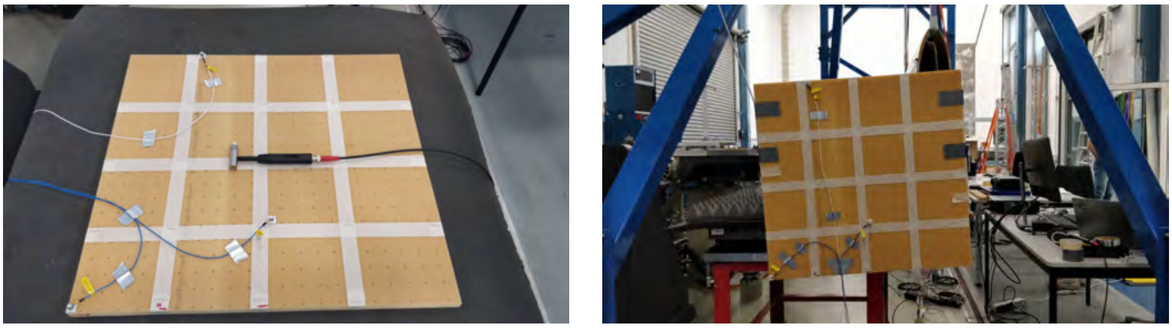

(a) Sample Plate Foam Boundary Conditions

(b) Sample Plate Bungee Cord Boundary Conditions

Figure 4.1: Sample Plate Roving Hammer Test Setups

During the modal test the response of the plate was damped very quickly therefore no windowing of the response signal was needed. For each excitation point 3 averages were used to obtain a clean frequency respone function. The Siemens LMS Testlab software was used to conduct the test measurements. To identify the modal parameters of the sample plate the built in tool of LMS Testlab was used, this uses the PolyMAX method described in Section 2.3.2. For each of the two test configurations the first 16 modes were identified.

4.1.3. Modal Results

The modal parameters identified from the foam and bungee supported tests are shown here. The frequencies and damping ratios for the first 16 identified modes of the foam and bungee hammer tests are summarised in Tables 4.5 and 4.6 respectively.

Table 4.5: Sample Plate Foam Hammer Test Modal Parameters

Modal Param.	Mode 1	Mode 2	Mode 3	Mode 4	Mode 5	Mode 6	Mode 7	Mode 8
Freq. [Hz]	105.89	126.07	164.93	234.86	239.86	368.53	374.26	410.95
Damping Rat.	0.0140	0.0329	0.0195	0.0128	0.0130	0.0244	0.0241	0.0149
Modal Param.	Mode 9	Mode 10	Mode 11	Mode 12	Mode 13	Mode 14	Mode 15	Mode 16
Freq. [Hz]	413.71	463.87	601.58	609.44	625.59	658.39	688.48	700.42
Damping Rat.	0.0118	0.0210	0.0163	0.0155	0.0187	0.0200	0.0199	0.0153

Table 4.6: Sample Plate Bungee Hammer Test Modal Parameters

Modal Param.	Mode 1	Mode 2	Mode 3	Mode 4	Mode 5	Mode 6	Mode 7	Mode 8
Freq. [Hz]	104.55	122.34	168.12	232.73	238.16	366.45	374.37	407.66
Damping Rat.	0.0090	0.0099	0.0066	0.0103	0.0095	0.0145	0.0102	0.0144
Modal Param.	Mode 9	Mode 10	Mode 11	Mode 12	Mode 13	Mode 14	Mode 15	Mode 16
Freq. [Hz]	411.16	464.66	597.04	605.23	625.25	657.07	684.22	702.68
Damping Rat.	0.0100	0.0126	0.0134	0.0148	0.0124	0.0137	0.0123	0.0117

To show the quality of the identified mode shapes of both tests, their respective autocorrelation MAC matrices are plotted in Figure 4.2. The auto correlation plots for both tests are clean with no significant off-diagonal MAC values. This illustrates that there is no mode coupling present for the first 16 modes, and the shapes are high quality.

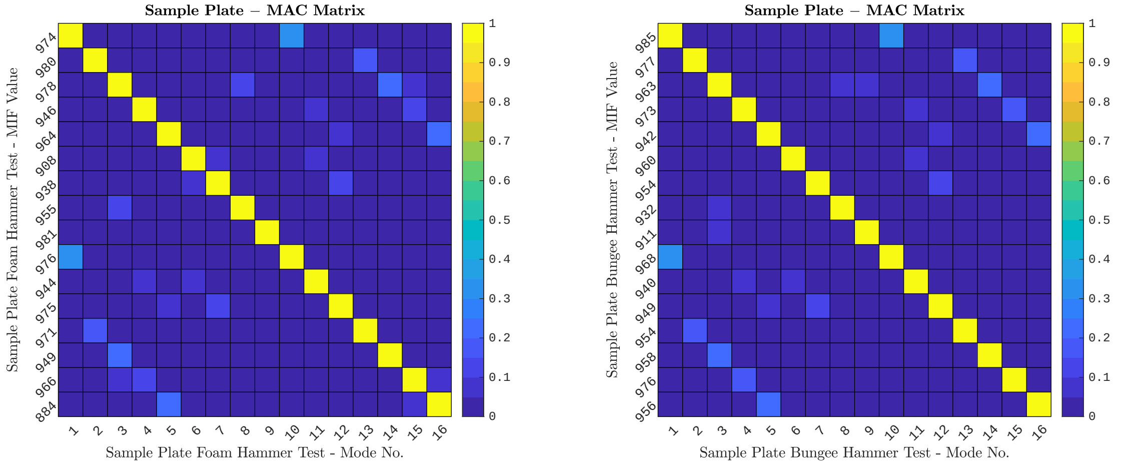

(a) Sample Plate Foam Hammer Test Auto MAC Matrix

(b) Sample Plate Bungee Hammer Test Auto MAC Matrix

Figure 4.2: Sample Plate Hammer Tests Auto Modal Correlation

The modal parameters of the foam hammer test show strong similarity to those of the bungee test. However, on average from the identified modes the foam test shows slightly higher frequency and damping. This suggests the foam underneath the plate increased out-of-plate stiffness and absorbed more energy from the plate vibration. The mode shapes of both tests are also compared directly with a MAC matrix shown in Figure 4.3. The MAC corrleation matrix is nearly identity apart from modes 8 and 9, where the mode shapes appear to have some difference, which may be a result of the boundary conditions.

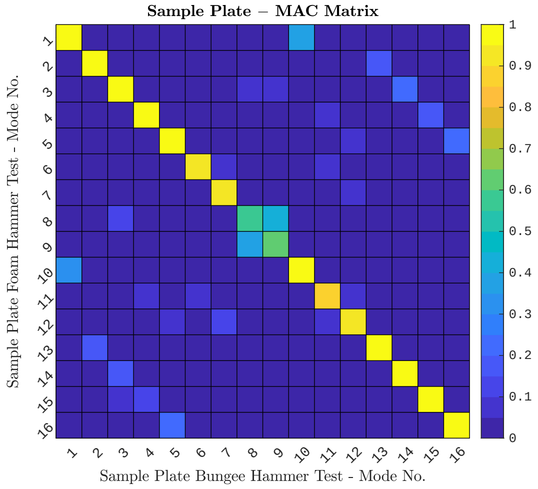

Figure 4.3: Sample Plate Hammer Tests MAC Matrix

The results of boths tests are very similar. However, as the bungee suspension has lower frequency rigid body modes and thus less interference from the boundary conditions compared to the foam, it better represents a true free-free condition. Considering this the modal model generated from the bungee test is used for future analysis of the sample plate. The first 9 mode shapes are shown in Figure 4.4.

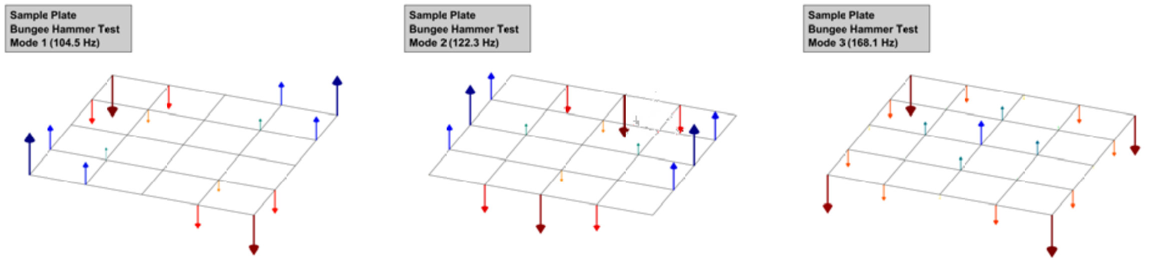
Sample Plate
Bungee Hammer Test
Mode 1 (104.5 Hz)
Sample Plate
Bungee Hammer Test
Mode 2 (122.3 Hz)
Sample Plate
Bungee Hammer Test
Mode 3 (168.1 Hz)

(a) Mode 1: Torsion (b) Mode 2: Saddle (c) Mode 3: Breathing

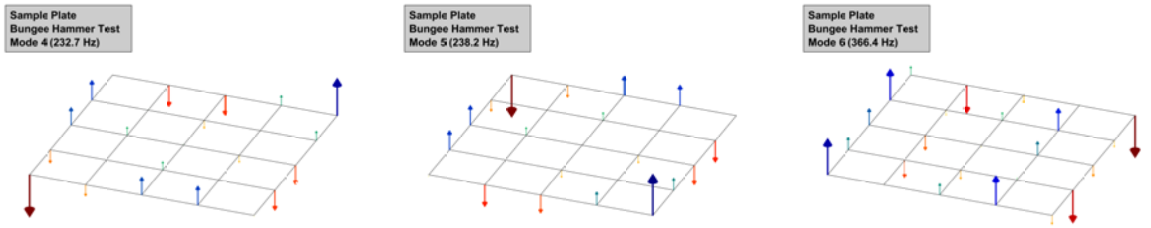
Sample Plate
Bungee Hammer Test
Mode 4 (232.7 Hz)
Sample Plate
Bungee Hammer Test
Mode 5 (238.2 Hz)
Sample Plate
Bungee Hammer Test
Mode 6 (366.4 Hz)

(d) Mode 4: Wave 1 (e) Mode 5: Wave 2 (f) Mode 6

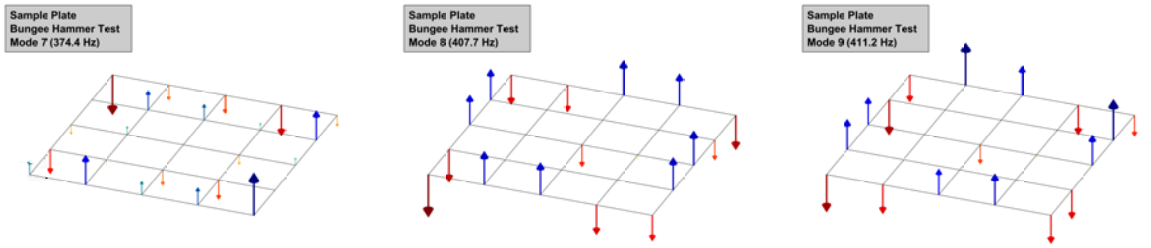
Sample Plate
Bungee Hammer Test
Mode 7 (374.4 Hz)
Sample Plate
Bungee Hammer Test
Mode 8 (407.7 Hz)
Sample Plate
Bungee Hammer Test
Mode 9 (411.2 Hz)

(g) Mode 7 (h) Mode 8 (i) Mode 9

Figure 4.4: Sample Plate Bungee Hammer Test Identified Mode Shapes 1-9

As a result of the ±45° laminate the lowest frequency mode of the plate is torsion mode, followed by a saddle shape, and a breathing shape mode shown in Figures 4.4a to 4.4c respectively. Beyond these first three modes the shapes for the higher frequencies are more wave like in shape and more nondescript.

It should be noted that while mode 3 shows some similarity with the breathing modes of the blade and blade section, the sample plate is too different of a structure to draw a direct comparison between them. The purpose of the sample plate study is not find breathing modes within the plate but rather investigate the effect of element and material differences.

4.1.4. Flexural Stiffness Tests

As demonstrated in Section 4.1.1, there is difference in material properties between the sample plate and blade as a result of fibre volume content. To better approximate the sample plate properties three point bending tests are made from coupons cut from the sample plate. Three point bending tests were chosen as they are simpler to conduct than tensile testing because of the core material, in addition to the fact that the flexural behaviour may be particularly relevant for the breathing modes.

Three test coupons for each principal direction of the laminate (0°, 45°, 90°) were tested according to ISO Standard 14125 for determination of flexural properties [13]. The test samples were cut from the sample plate of Section 4.1.1, a diagram of how the test samples were processed is shown in Figure 4.5a.

To quantify the flexural stiffness of the test coupons two calculation methods are used in conjunction with three different measurement systems. The first calculation method is the ISO 14125 standard calculation [13] which uses the bench measurement system. Namely the setup dimensions, bench displacement s, and force measurement P to estimate the flexural stiffness. A diagram of the test setup is shown in Figure 4.5b.

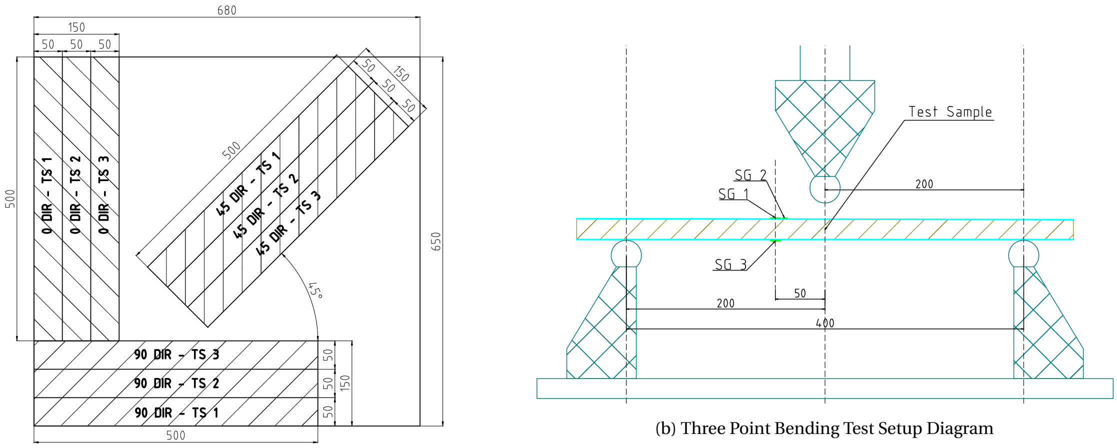

(b) Three Point Bending Test Setup Diagram

(a) Sample Plate Test Coupons Diagram

Figure 4.5: Sample Plate Flexural Bending Test Diagrams

The ISO calculation method assumes a homogenous Euler-Bernoulli beam in bending, which considers no transverse shear and out-of-plane deformation. The flexural modulus is expressed for this case in Equation (4.14), alternatively the flexural stiffness can be quantified in terms of a classical plate as D_f in Equation (4.15). The ISO 14125 standard states to calculate these parameters between 0.05% and 0.25% percent flexural strain in Equation (4.16). Where displacement s is related to the specified flexural strains $\epsilon'_f = 0.05\%$, $\epsilon''_f = 0.25\%$ respectively.

$$E_f = \frac{L^3}{4bh^3}\left(\frac{\Delta P}{\Delta s}\right) \qquad (4.14) \qquad\qquad D = \frac{L^3}{48b}\left(\frac{\Delta P}{\Delta s}\right) \qquad (4.15) \qquad\qquad s = \epsilon_f \cdot \frac{L^2}{6h} \qquad (4.16)$$

To verify the bench measurements, a second measurement system is used, namely strain-gauges are placed upon the face sheets of the samples at 50 mm distance from the centre loading member. On the first test coupon of each series, strain-gauges 1 'SG1' and 3 'SG3' measure the longitudinal strain of the top and bottom faces respectively, and strain-gauge 2 'SG2' measures the transverse strain on the top face. On the second and third test samples of each series strain gauge 2 is omitted. The locations of the strain-gauges are shown in the test setup diagram, Figure 4.5b.

The strain-gauges are placed at a specific distance from the loading member such that they experience the same local bending moment. Using the width of the coupon b and position of the strain-gauges relative the loading member d_{sg} and neutral axis h_{sg}, the measured strain can be used to estimate the flexural stiffness D_f shown in Equation (4.17). To ensure the flexural stiffness is calculated only using bending strain ϵ_B, the tensile strain component is removed from the measurements of 'SG1' and 'SG2' shown in Equation (4.18). Lastly using strain-gauge 2, the major poisson ratio ν can be calculated for the first sample in each series, this is shown in Equation (4.19).

$$D_f = \frac{d_{sg} h_{sg}}{2b}\left(\frac{\Delta P}{\Delta \epsilon_B}\right) \qquad (4.17) \qquad\qquad \epsilon_B = \epsilon_{sg1} - \frac{\epsilon_{sg1} + \epsilon_{sg3}}{2} \qquad (4.18) \qquad\qquad \nu = -\frac{\Delta \epsilon_{sg1}}{\Delta \epsilon_{sg2}} \qquad (4.19)$$

The third measurement system used is a digital image correlation (DIC) strain measurement system to measure the strain of the test sample core material. The purpose of the DIC system is to quantify the amount of transverse shear strain as well as out-of-plane strain. This allows to determine how valid the beam theory based methods being used to estimate the flexural stiffness of coupons are. The second and third test samples from each series have a painted speckle pattern on their core material to enable measurement. A picture of the DIC test configuration is shown in Figure 4.6.

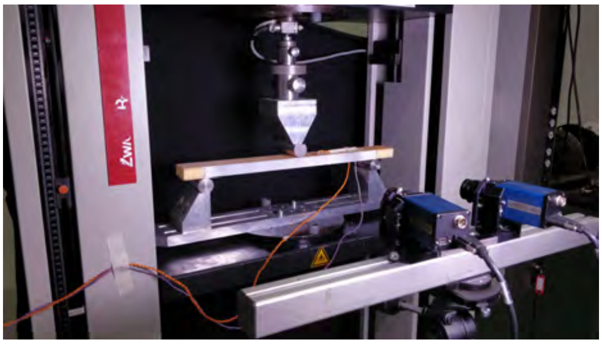

Figure 4.6: Sample Plate Test Coupon with DIC measurement system in three point bending test machine

4.1.5. Flexural Stiffness Results

The load-displacement plots for all 9 samples is shown in Figure 4.7. As expected the 45 test series ('45 DIR-TS') clearly show the stiffest behaviour as it aligned along the fibre direction of the laminate. There is also a considerable difference in stiffness between the 0 ('0 DIR-TS') and 90 ('90 DIR-TS') test series' which is not expected as the data-sheet shows a symmetric distribution of glass weight in Table 2.2.

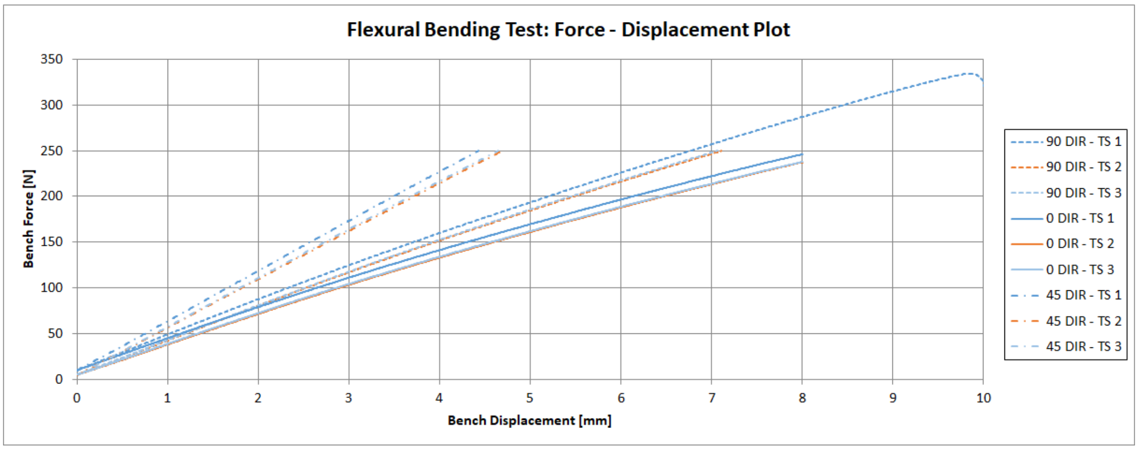

Figure 4.7: Sample Plate Test Coupon Flexural Stiffness Test Force - Displacement Plot

The flexural stiffness for both methods are calculated as an average for each coupon series. Additionally the major poisson ratio is calculated for the first coupon of each series. To compare the test results the flexural stiffness and estimated major poisson ration for the plate are also calculated using composite laminate theory, using the D_{xx} values from the ABD matrix and ν_{12} from the extrapolated engineering constants as described in Appendix A. For this the rule of mixtures properties from Table 4.4 are used. The results are shown in Table 4.7.

Table 4.7: Flexural Stiffness Test Results

Identifier	D_f (ISO) [N mm]	D_f (SG) [N mm]	ν (SG) [-/-]	D_{11} (ROM) [N mm]	ν_{12} (ROM) [-/-]
0 DIR Series	873,537	846,405	0.412	2,005,716	0.653
45 DIR Series	1,436,806	1,825,132	0.167	3,183,335	0.070
90 DIR Series	1,004,392	1,071,894	0.704	1,993,866	0.650

Comparing the experimental values with the rule of mixtures CLT results shows a very clear difference, with the experimental stiffness being 40 – 60% less than predicted. As the experimental flexural stiffness calculation methods assumed no out-of-plane and shear deformation the DIC results are examined to see if these were present during the test. The engineering strain captured by the DIC system is shown for test sample 2 of the 0 series in Figure 4.8

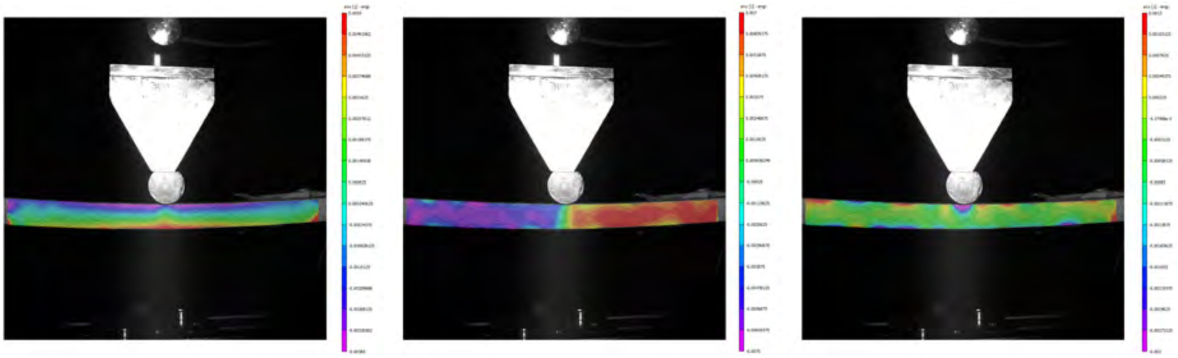

(a) Longitudinal Strain ϵ_{xx} (b) Transverse Shear Strain ϵ_{xy} (c) Out-of-Plane Strain ϵ_{yy}

Figure 4.8: Test Coupon '0 DIR - TS 2' DIC strain fields at maximum load (~237 N)

During the DIC measurements issues relating to the speckle pattern size and calibration were encountered, resulting in only the presented test coupon '0 DIR - TS 2' having clear data. Noting this accuracy limitation the DIC strains captured at maximum load can be compared with the measured longitudinal strain gauge values of 'SG1' and 'SG2' to validate the DIC accuracy. The DIC measurements were difficult to extract from the images, therefore the approximated min and max values are compared as opposed to the local measurement at the strain gauges, these measured strain results are presented in Table 4.8.

Table 4.8: Test Coupon '0 DIR - TS 2' Measured Strains at maximum load (~237 N)

0 DIR - TS 2	(Strain-Gauge) ϵ_{sg} [-/-]	(DIC) ϵ_{xx} [-/-]	(DIC) ϵ_{xy} [-/-]	(DIC) ϵ_{yy} [-/-]
Maximum Strain	0.00568	0.0055	0.0070	0.0013
Minimum Strain	-0.00508	-0.0038	-0.0075	-0.0030

The table shows roughly similar longitudinal strain values within 25% between the DIC system and strain-gauges, which is quite positive considering the measurement issues. With roughly similar results examination of the transverse shear strain and out-of-plane strain shows the min and max strains are all of the same order of magnitude. This indicates that the shear and out-of-plane deformation are significant, and the methods used to determine the flexural stiffness of the test should underestimate the composite laminate theory values. This is consistent with the results of Table 4.7. Therefore, to make an appropriate comparison with the test results the predicted model stiffness needs to consider these shear and out-of-plane strain effects. This is investigated in Section 4.2.6.

The DIC measurement of the transverse shear strain also makes it possible to make a rough estimation of the shear modulus of the laminate. As discussed in Section 2.2.2, the shear deformation is dominated by the core material when the ratio of face sheet thickness to core thickness is high. For the sample plate the ratio of core thickness to face sheet thickness is 40, indicating that the transverse shear stiffness of the laminate should be very close to the shear modulus of the core material. To estimate the shear modulus Equation (4.20) is used, which is a very crude approximation for a homogenous beam.

$$G_{lam} = \frac{P_{max}}{2\epsilon_{xy} A} \tag{4.20}$$

Using the DIC transverse shear strain, coupon cross-section area, and max bench force a transverse shear modulus of ~17 MPa is obtained. Considering the inaccurate strain and equation, this is fairly close to the specified core material shear modulus of 22 MPa. This suggests the material uncertainty for the core materials is insignificant for the sample plate and blade.

4.2. Sample Plate Models

The first breathing mode is not clearly identified by the topology changes made for the blade section model, as examined in Chapter 3. It is hypothesised that the cause of the breathing mode may be unrelated to the model topology and instead related to the element size/configuration as well as the mass and laminate material properties. To determine if these factors play a role in the prediction of breathing modes, a finite element model of the sample plate which uses similar materials to the blade is created and analysed for these material and element effects. To determine the sensitivity of these parameters the finite element models of the sample plate are compared with the results of the modal and static testing of the plate of Section 4.1.

4.2.1. Reference Plate Model

To serve as a baseline a reference model of the plate is created with the similar characteristics as that of the blade section model. The reference sample plate model utilises the same architecture with *CQUAD4* elements of 50 mm size. The finite element model is compared with a picture of the sample plate in Figure 4.9.

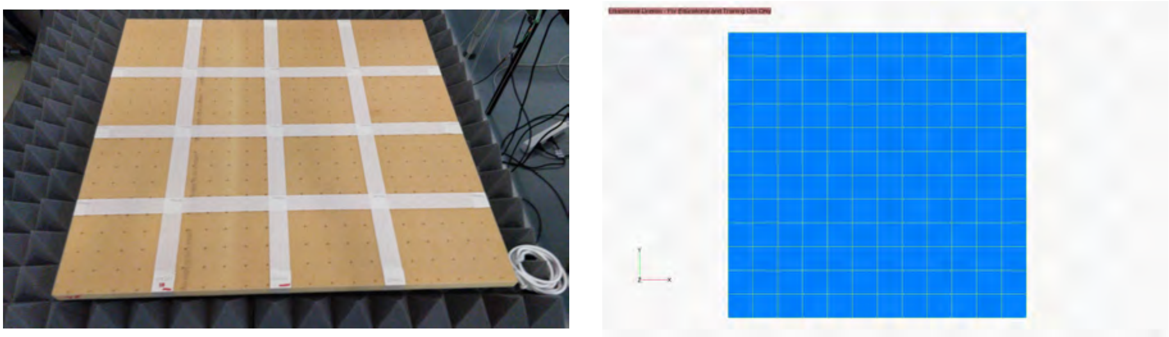

(a) Sample Plate Top View

(b) Sample Plate Reference Model *CQUAD4* 50 mm

Figure 4.9: Sample Plate and Reference FE Model Comparison

The properties of the reference plate model are the same as that used in the blade section. Namely the face sheets used the properties of the ’2AX45’ laminate including thickness and modulus, and the core material uses the properties of the ’C70-55-20 mm (Spar)’ including modulus and density these properties are detailed in Table 2.3. The blade section properties are used to have an appropriate comparison between the sample plate and blade section. While the sample plate itself was manufactured with same materials, it is recognised that the parameters of its manufacture are different and the effects of these differences are examined in Sections 4.2.4 to 4.2.6.

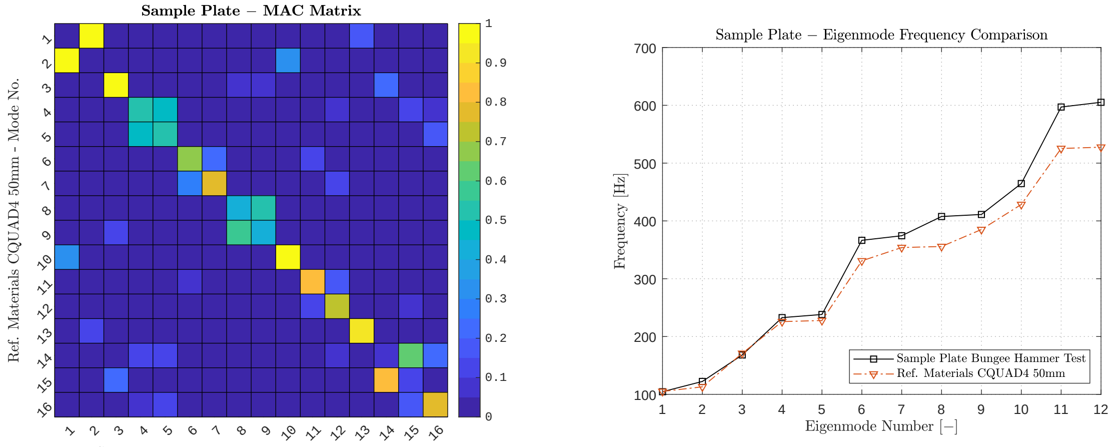

(b) Sample Plate Reference FE Model Eigenmode Frequency Comparison

(a) Sample Plate Reference FE Model - Bungee Hammer Test MAC Matrix

Figure 4.10: Sample Plate Reference FE Model Modal Comparison

In an analogous method as used for the blade section, the sample plate finite element model is subjected to a free-free modal analysis. The modal parameters extracted from the model can then be compared using the method described in Section 2.1.6 to select the closest node and degree of freedom matching with the experimental modal test results. The finite element model of the sample plate is meshed such that there is a node placed exactly in the position of the test sensors to eliminate any position uncertainty. The mode shapes between the reference model and bungee experiment for the sample plate are correlated in the MAC matrix of Figure 4.10a, and the mode frequencies are compared in Figure 4.10b.

The plots show that the mode frequencies between the experiment and finite element model are fairly close with a slight under-prediction with increasing frequency. Interestingly this is a similar trend as observed for the frequency behaviour of the blade section. The mode shape correlations show very strong results where most modes have a clear identification, particularly regarding the first three modes all with MAC values above 0.95. This is a very different result than the blade section which has low MAC values and few identified modes. This is likely attributed to the very simple structure and geometry of the plate in contrast to the much more complex blade section. However the first two modes are in the wrong order and some modes have more coupled shapes with lower MAC values. For such a simple structure a nearly identity MAC matrix would be expected. This suggests that there exists differences between the model and experiment, unrelated to geometry or sensor position as this has been controlled for.

4.2.2. Shell Element Size

For a fundamental structure of a rectangular panel, much better correlation results should be expected than what was predicted with the reference model. To establish a likely cause for these differences the principal aspects of the model must be examined for their sensitivity in the results. It is hypothesised that inconsistencies in modelling the plate may relate to the ability of finite element models to predict the breathing modes of the full and blade section.

The first aspect to be examined is the model sensitivity to element size, thus a convergence study is made. Five different versions of the sample plate model are created with element size varying from 200 mm to 10 mm. The meshes of these of these models are shown and compared in Figure 4.11.

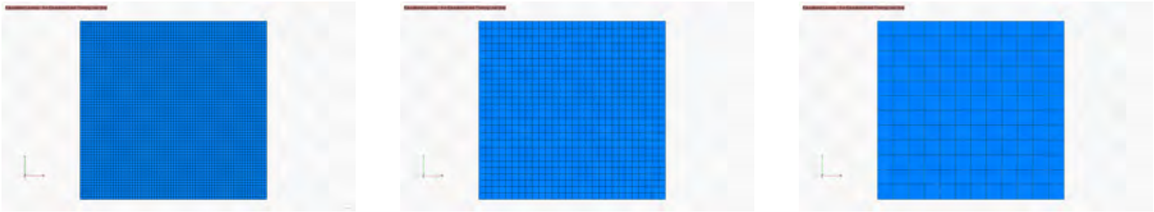

(a) 10 mm Element Size (b) 25 mm Element Size (c) 50 mm Element Size

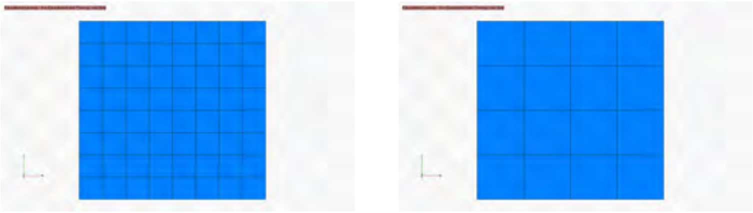

(d) 100 mm Element Size (e) 200 mm Element Size

Figure 4.11: Sample Plate *CQUAD4* Finite Element Models for Varying Element Size

These models are subjected to a free-free modal analysis and their modal parameters are compared to each-other to determine the effect of element size. A comparison of the five models mode frequencies is shown in Figure 4.12b. The results show a clear convergence behaviour on the mode frequencies with increased element density. This is also visualised in Figure 4.12a where the different models are normalised to the 10 mm element size model. The lower frequency modes appear to converge must faster than the higher frequency modes, an expected result considering their more simplistic shapes.

In the context of predicting the breathing modes, which were experimentally determined to be among the lowest frequency modes of the blade and blade section systems, it seems that beyond a threshold element size, in this case 100 mm, the lowest frequency modes show less than a 5% difference with the converged 10 mm model. So for a plate of minimum dimension 650 mm, which is significantly smaller than the trailing edge panels of the blade, a 50 mm element size predicts the frequency within 5% up to the 11^{th} mode.

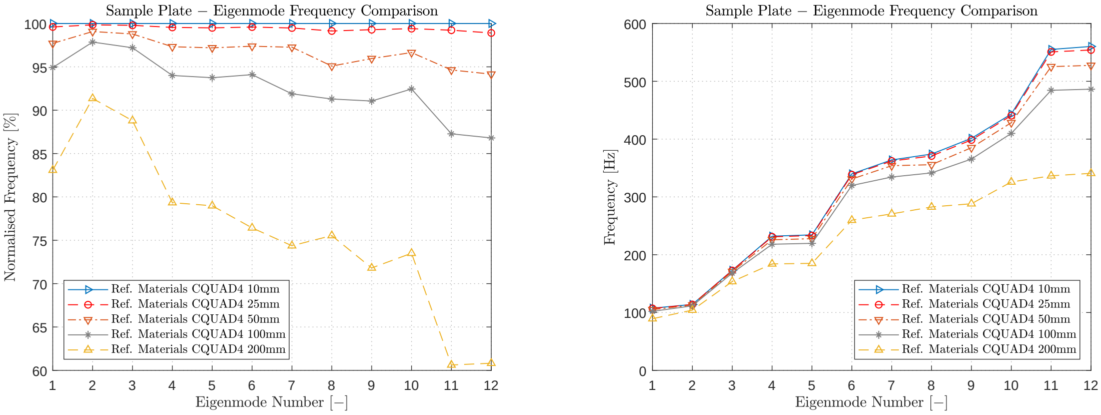

(a) Eigenmode Normalised Frequency Comparison (b) Eigenmode Frequency Comparison

Figure 4.12: Sample Plate *CQUAD4* Element Size Models Mode Frequency Comparison

In addition to the mode frequency behaviour the effect on mode shape is also considered. In Figure 4.13 the element size models are correlated in a MAC matrix with the 10 mm model.

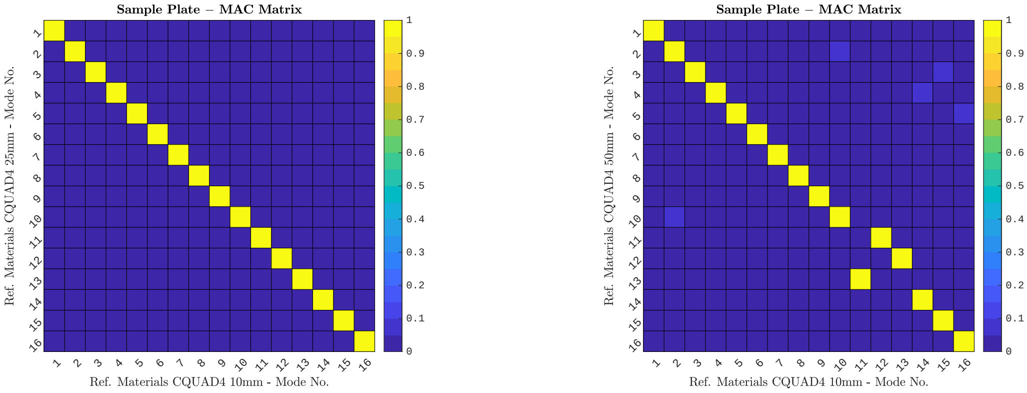

(a) *CQUAD4* 25 mm MAC Matrix (b) *CQUAD4* 50 mm MAC Matrix

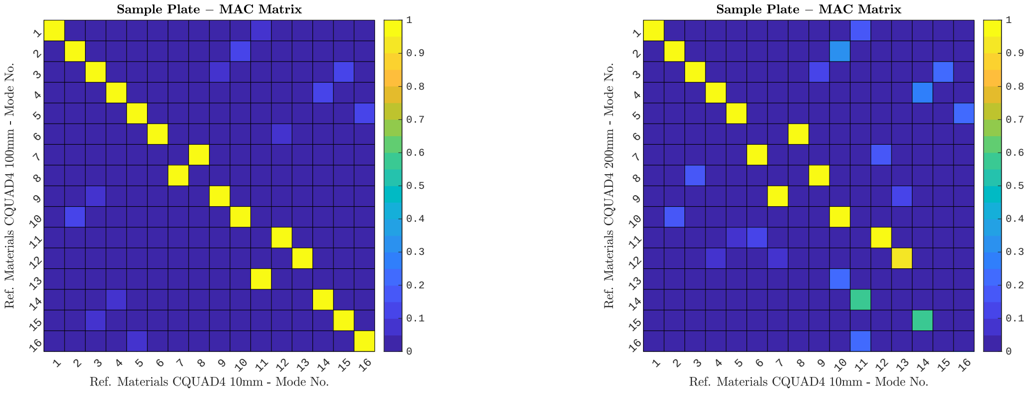

(c) *CQUAD4* 100 mm MAC Matrix (d) *CQUAD4* 200 mm MAC Matrix

Figure 4.13: Sample Plate Mode Shape Correlation for Element Size Models with 10 mm Model

The correlation of the mode shapes show a consistent behaviour across all models with MAC values greater than 0.95 on all of the modes with the exception of the 200 mm model. The property which seems to vary the most for the modes shapes is the order of the modes. However this is limited to the higher frequency modes and modes close in frequency for the 50 mm and 100 mm element size models.

In the context of the breathing modes it can be seen for the converged models the low frequency modes show an excellent prediction of the mode shapes. It is considered that the element size is very unlikely to be a factor for the inability to predict the breathing mode shapes. For this reason the 50 mm element size is deemed sufficient to adequately predict the vibration modes of the full blade and blade section models considering they have larger panels relative to the sample plate. As the blade has larger panel area using the same element size results in a higher element density per modelled area and therefore offers a better approximation of the same basic mode shapes. For the purposes of further examination of the sample plate an element size of 10 mm is used to greatly limit its influence on the mode order and frequency.

4.2.3. Model Element Configuration

With the influence of element size on the finite element modal results established, the affects of model element configuration are examined. While shell element a commonly employed method to predict the behaviour of plate structures there are different variations of these implementations as well as higher fidelity configurations that may improve prediction of the modal behaviour. Here five different model configurations are examined for their potential effect on the prediction of the sample plate modal behaviour.

The baseline *CQUAD4* linear shell element with 4 nodes in NASTRAN is examined, this is the industry standard element with reduced integration and 5 nodal degrees of freedom [38]. Additionally the linear *CQUADR* reduced integration shell element is also examined. The *CQUADR* element also uses 4 nodes and an updated formulation of the *CQUAD4* element with an additional out of plane torsional degree of freedom for a total of 6 [38]. Lastly the quadratic serendipity function *CQUAD8* shell element configuration is examined with mid-side nodes and 5 nodal degrees of freedom.

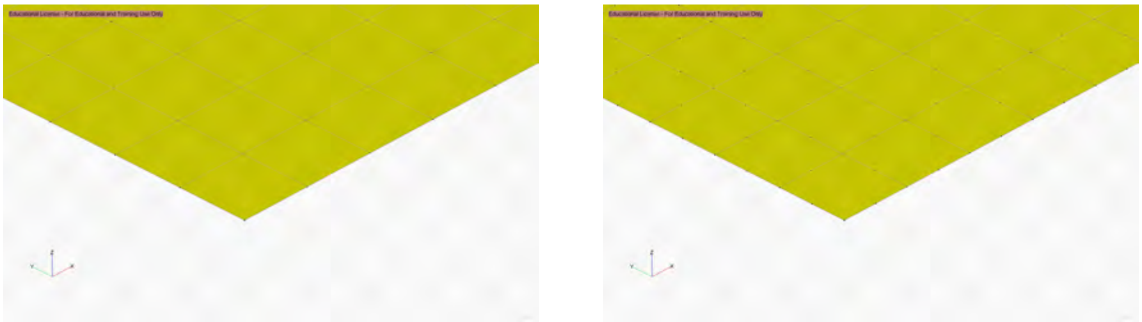

(a) *CQUAD4*/ *CQUADR* Element Configurations

(b) *CQUAD8* Element Configuration

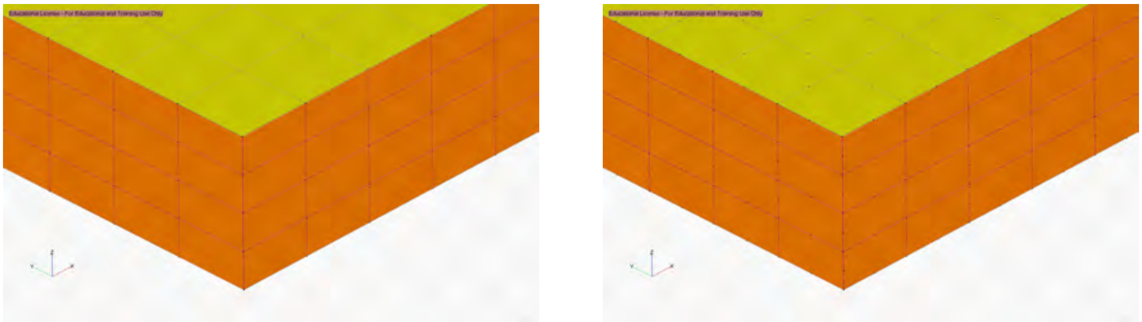

(c) *HEX8* Core Element Configuration

(d) *HEX20* Core Element Configuration

Figure 4.14: Sample Plate Element Configuration Models

In addition to these shell elements, two other configurations are examined where the core material is modelled with continuum elements merged with the shell nodes of the faces. The advantage of such a model is that is has a better prediction of transverse shear strain in the core as the additional degrees of freedom allow variation of displacement through the thickness. The shell elements available in MSC NASTRAN are based on Mindlin plate theory where a constant strain is used to represent the transverse strain necessitating energy correction methods to correctly predict the transverse shear stiffness. The first model uses *CQUAD4* elements to represent the face sheet laminas, with four *CHEXA8* continuum elements through the thickness to represent the core material. The second variation of this model uses *CQUAD8* elements to represent the face laminas and four *CHEXA20* elements through the thickness to represent the core material. The *CHEXA8* and *CHEXA20* continuum elements have only three nodal degrees of freedom representing translation, and utilise iso-parametric integration schemes [38]. The considered element configurations are shown in Figure 4.14.

The considered element configurations are subject to a free-free modal analysis and their mode frequency behaviours are compared in Figure 4.15b. At the absolute scale all the model configurations have nearly identical mode frequency behaviour. The models are then compared more closely with a normalised frequency scale in Figure 4.15a with the *CQUAD4* model configuration as a reference. The variation of frequency over the different element configurations is extremely small where the first 12 modes vary less than 1.5%. The shell element models have very close frequencies, with the *CQUAD8* model showing the highest mode frequencies, followed by the *CQUADR* model and then the *CQUAD4* model. This is a logical result as these models have higher degrees of freedom and have a slightly stiffer behaviour.

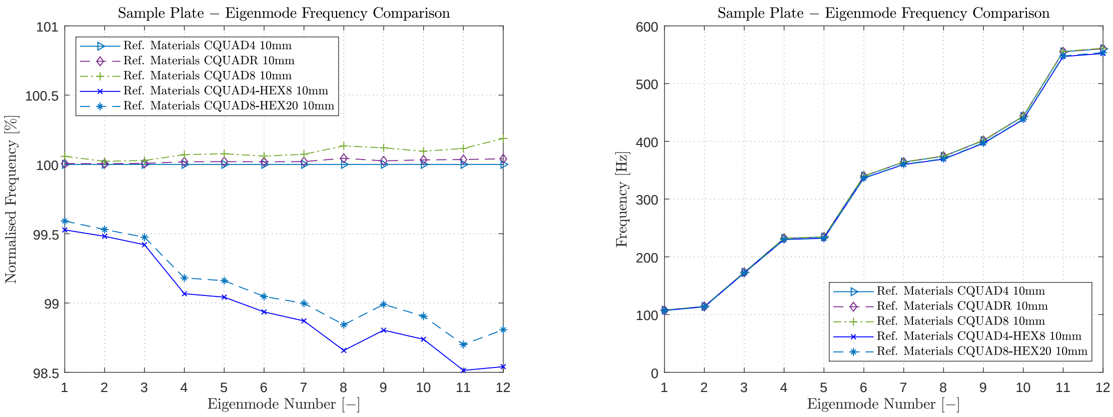

(a) Eigenmode Normalised Frequency Comparison

(b) Eigenmode Frequency Comparison

Figure 4.15: Sample Plate 10 mm Element Configuration Models Mode Frequency Comparison

The continuum element core models appeared to have a distinctively different trend than the shell element models. Particularly they showed lower mode frequencies, this is also an expected results as previously mentioned shells tend to over estimate the transverse shear stiffness of laminates with this effect becoming greater with increased frequency modes. The two continuum models had the same difference in behaviour between the quadratic and linear elements for the shells. Namely the quadratic *CQUAD8-CHEXA20* element model showed stiffer behaviour with increased mode frequencies compared to the *CQUAD4-CHEXA8* model.

However in the greater context of predicting the breathing mode shapes for the blade it is distinctly clear that for the low frequency modes the other element configurations show no distinct advantage over the standard *CQUAD4* element.

Considering the effect of mode shapes the modal results for the different element configurations are correlated in a MAC matrix with the baseline *CQUAD4* model in Figure 4.16. Similar to the mode frequency behaviours, all models have an identity MAC matrix with all MAC values above 0.95. No distinct differences between the model configurations are observed with respect to mode shape or order.

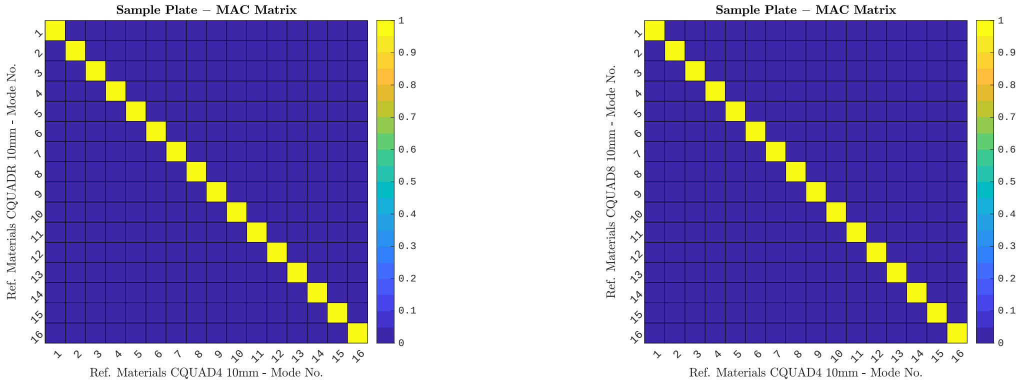

(a) *CQUADR* 10 mm Model MAC Matrix

(b) *CQUAD8* 10 mm Model MAC Matrix

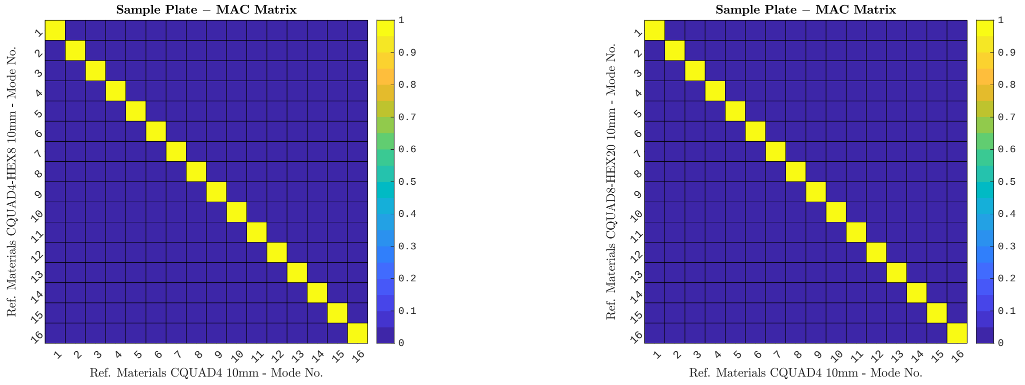

(c) *CQUAD4-CHEXA8* 10 mm Model MAC Matrix

(d) *CQUAD8-CHEXA20* 10 mm Model MAC Matrix

Figure 4.16: Sample Plate Mode Shape Correlation for Element Configuration Models with *CQUAD4* 10 mm Model

The results clearly show that for simple plate like geometries undergoing modal analysis, more advanced shell element configurations do not have a distinct advantage over the standard *CQUAD4* element. In the context of predicting breathing modes, the trailing edge panels of the blade have small curvatures and are comparable to the sample plate case. Therefore the *CQUAD4* element is more than sufficient to model the sample plate and blade for the low frequency modes being examined.

4.2.4. Adjusted Core Density

The numerical effects on the modelling of the sample plate have been investigated, it is now important to examine the effects of mass and stiffness. The reference material properties used for the blade section are not necessary applicable for the sample plate as the manufacturing parameters are different as discussed in Section 4.1. The first aspect of these differences to be investigate is the effect of the mass of the sample plate materials. The simulated mass with reference materials and the measured mass of the plate are compared in Table 4.9.

Table 4.9: Sample Plate and Reference Model Mass Comparison

Sample Plate Mass	Reference Materials Model Mass
1715 g	2627 g

The reference materials significantly over estimate the mass of the plate by approximately 50%, which likely results in underestimated mode frequencies. To investigate this effect the density of the core material is adjusted to match the mass of the plate. The non-infused density of the 'C70-55 (dry)' foam core is 60 kg/m^3, compared to the assumed 'C70-55-20 mm (Spar)' foam core with density of 180 kg/m^3 used for the reference model as shown in Table 2.3. Therefore the density lies somewhere between these, the density of the core is then calculated to match the measured plate mass and the final adjusted material properties are shown in

Table 4.10.

Table 4.10: Sample Plate Adjusted Core Density Material Laminate Properties [29]

Material	Angle	E_1 [MPa]	E_2 [MPa]	G_{12} [MPa]	ν_{12}	FVC	t [mm]	ρ [kg/m^3]
2AX45	±45°	11316	11316	11978	0.633	50%	0.625	1875
C70-55-20 mm	-	55	55	22	0.3	-	20	76.82

These adjusted material properties are applied to the *CQUAD4* 10 mm model and subjected to a free-free modal analysis. The resulting mode frequencies are compared in Figure 4.17. Interestingly the adjusted material model shows a constant relative change over the original model. Figure 4.17a shows the mode frequencies normalised to the reference material model. This better shows how the reduced mass of the adjusted materials model increased the mode frequencies exactly 23.8% over the reference model. This uniform changing of the panel density results in a truly constant change of the mode frequencies.

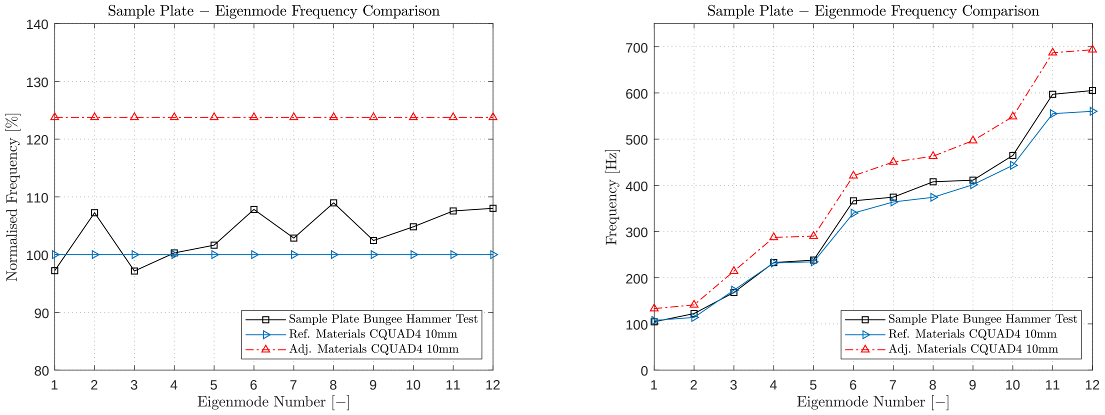

(a) Eigenmode Normalised Frequency Comparison (b) Eigenmode Frequency Comparison

Figure 4.17: Sample Plate Adjusted Materials Model Mode Frequency Comparison

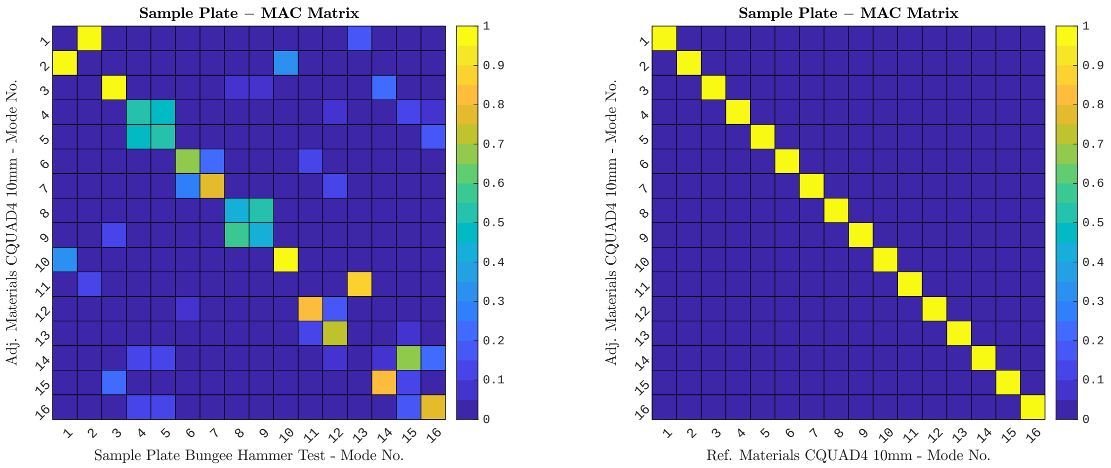

(a) Sample Plate Adjusted Materials FE Model - Bungee Hammer Test MAC Matrix

(b) Sample Plate Adjusted Materials FE Model - Reference Materials FE Model MAC Matrix

Figure 4.18: Sample Plate Adjusted Materials Model Modal Correlation

The mode shapes of the adjusted materials finite element model are correlated in a MAC matrix with the bungee hammer test in Figure 4.18a. The correlation with the bungee hammer test appears unchanged over the reference plate model discussed in Section 4.2.1. The sample plate reference model and the adjusted core density material model are correlated directly in a MAC matrix shown in Figure 4.18b. The direct correlation shows an identity MAC matrix, demonstrating that changing the mass properties in such a global way has no effect at all on the mode shapes.

Considering the full blade and blade section models it is thought that the mass distribution can have a large affect on the mode frequencies. However in the context of the breathing mode shapes, changes to the laminate or core density of the trailing edge panels are likely to be distributed in a nearly global way. This then implies that inaccuracies in the panel densities are not likely to make a significant change on the mode shapes of the blade but mostly affect their frequencies. It is also possible that inaccuracies in panel mass could be more localised in nature and this could potentially have an effect on the panel mode shapes, but its effect is likely small.

4.2.5. Rule of Mixtures Properties

Having examined the effects of the panel mass the laminate stiffness properties should also be considered. The manufacturing parameters for the blade reference materials, particularly the fibre volume fraction are certainty different than those for the sample plate. As discussed in Section 4.1.1 the measurements of the plate mass and thickness are combined with the data sheet parameters of the glass, resin, and foam core to calculate a new estimated set of material properties based on the rule of mixtures and composite laminate theory. These estimated material properties are shown in Table 4.4.

It should be noted that there may be uncertainties in the underlying data sheets so these parameters are only an estimation. It should also be considered that the rule of mixtures is not an entirely accurate method to determine lamina stiffness properties and is merely an estimate based off the extracted parameters of the sample plate.

The estimated materials model is subject to a free-free modal analysis and the mode frequencies are compared in Figure 4.19. The estimated material properties appear to show similar results to the reference model however using correct mass values. The mode frequencies are also normalised to the bungee experiment modal results shown in Figure 4.19a. The estimated material model frequencies appear to show similar frequency behaviour as the reference materials properties, however with better accuracy for the higher frequency modes. The estimated material model can be said to closely match the experimental frequencies, however some discrepancies still exists particularly mode 2 which is underestimated by over 10%.

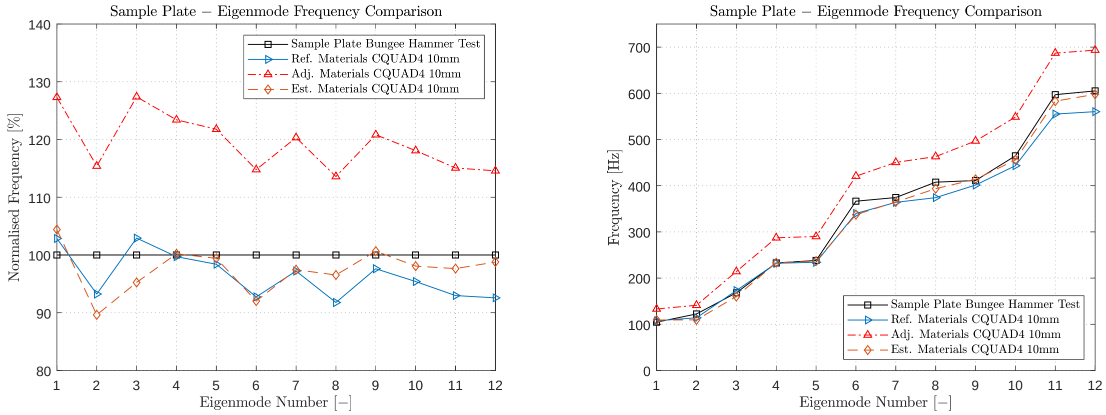

(a) Eigenmode Normalised Frequency Comparison

(b) Eigenmode Frequency Comparison

Figure 4.19: Sample Plate Rule of Mixtures Estimate Materials Model Mode Frequency Comparison

The estimated material model is then correlated in MAC matrix with the bungee hammer test in Figure 4.20a. The estimated materials show a more correct mode order than the reference model with the first three modes now correctly identified apart from their frequency. This result is confirmed when the estimated material model is correlated directly with the adjusted material model in Figure 4.20b. The direct modal correlation shows identity MAC values and mode order switching for mode pairs 1-2, and 14-15.

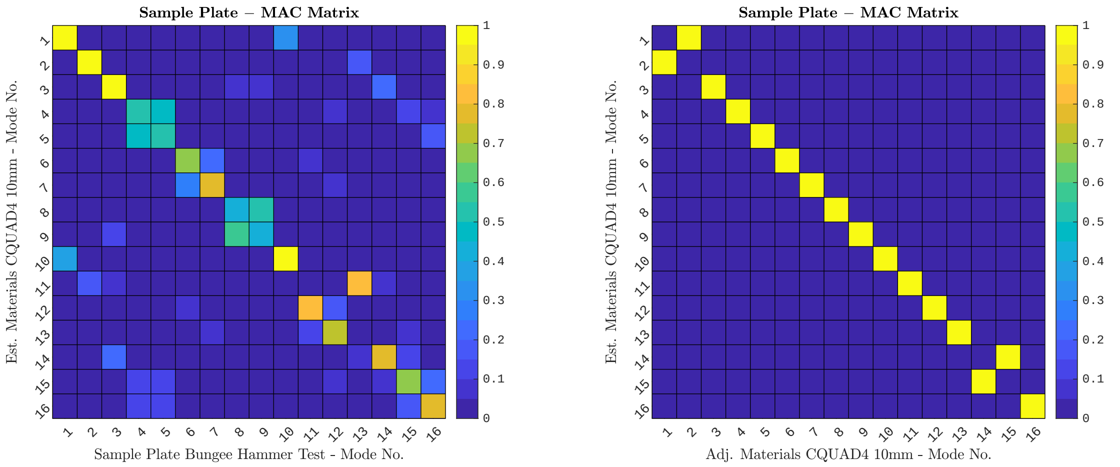

(a) Sample Plate Estimated Materials FE Model - Bungee Hammer Test MAC Matrix

(b) Sample Plate Estimated Materials FE Model - Adjusted Materials FE Model MAC Matrix

Figure 4.20: Sample Plate Rule of Mixtures Estimated Materials Model Modal Correlation

While the estimated material model showed improved correlation over the reference and adjusted material models there still appears to be fundamental differences with bungee hammer test results. Particularly the second mode has a large 10% frequency difference, and the mode couples of 4-5, 6-7, and 8-9 have low MAC values with bungee test modes. For such a simple plate structure the modal correlation should be very close to identity, which is not the case with the property sets examined.

4.2.6. Flexural Test Model

In the original blade models only the unidirectional spar cap material was mechanically tested for its stiffness and strength properties, the remaining laminate material properties were estimated in an unknown way. Considering the improved results for the rule of mixtures estimated material properties discussed in Section 4.2.5, the same method is applied to try to replicate the blade reference material properties. The same *2AX45* laminate properties are estimated according to the data sheet specifications and prescribed fibre volume content using the same rule of mixtures and composite laminate theory method. A comparison of the reference and estimated values is shown in Table 4.11.

Table 4.11: '2AX45' Estimated Material Laminate Property Comparison

Material	Angle	E_1[MPa]	E_2[MPa]	G_{12}[MPa]	ν_{12}	V_f	t[mm]	ρ[kg/m^3]
2AX45 (Ref.)	±45°	11316	11316	11978	0.633	50%	0.625	1875
2AX45 (Est.)	±45°	7112.60	7049.07	6556.45	0.525	50%	0.6183	1860.15
Difference (%)	-	-37.15	-37.71	-45.25	-17.06	-	-1.07	-0.79

Table 4.12: 'UD' Estimated Material Laminate Property Comparison

Material	Angle	E_1[MPa]	E_2[MPa]	G_{12}[MPa]	ν_{12}	V_f	t[mm]	ρ[kg/m^3]
UD (Ref.)	0°	44151	14526	3699	0.3	55%	0.827	1948
UD (Est.)	0°	44674.51	7382.45	2539.90	0.2165	55%	0.8203	1936.14
Difference (%)	-	1.19	-49.18	-31.34	-27.83	-	-0.81	-0.61

An alarming discrepancy in properties is observed, where the thickness and density properties show very close agreement however the stiffness properties are significantly different. It should be considered that the rule of mixtures is not an entirely accurate method to estimate the stiffness laminates but can provide a close approximation. To illustrate this the properties of the 'UD' laminate are estimated and compared with the experimentally verified results in Table 4.12.

As can be seen the rule of mixtures estimates the 'UD' density and thickness closely in addition to the longitudinal stiffness E_1. However it fails to reproduce the transverse properties E_2, G_{12}, and ν_{12}. Considering such a large margin of error when comparing the estimated properties with the reference properties, mechanical testing of plate specimens was conducted to measure the properties of the plate, this testing is detailed in Section 4.1.4. The flexural stiffness measured from the bending tests are compared with the calculated values using composite laminate theory from the reference and estimated material properties in Table 4.13.

Table 4.13: Experimental Flexural Stiffness Comparison

Identifier	D_f (ISO) [N mm]	D_f (SG) [N mm]	D_{11} (Ref.) [N mm]	D_{11} (Est.) [N mm]
0 DIR Series	873,537	846,405	2,551,089	2,001,942
45 DIR Series	1,436,806	1,825,132	3,683,136	3,190,205
90 DIR Series	1,004,392	1,071,894	2,551,089	1,989,977

The experimental flexural stiffness is more than 50% less than either the reference or estimated stiffness values. As discussed in Section 4.1.4 this discrepancy is likely attributed to transverse shear and out-of-plane compression of the core. Composite laminate theory assumes pure bending behaviour which is not representative of the conditions of the test. To provide a suitable comparison for the measured stiffness values, the test conditions are replicated in a finite element model of the three point bending test.

The test conditions are modelled in finite element by replicating the specimens using *CQUAD8* elements for the face lamina and *CHEXA20* elements to model the core. A fine mesh is used with an average size of 5 mm, and 8 elements are modelled though the thickness of the core material. The test specimen is simply supported on the supporting bars 400 mm apart, and an *RBE2* element couples vertical displacement from the top-side middle nodes to a control point where a 250 N load is applied in the downward direction. An image of the three point bending test model is shown in Figure 4.21.

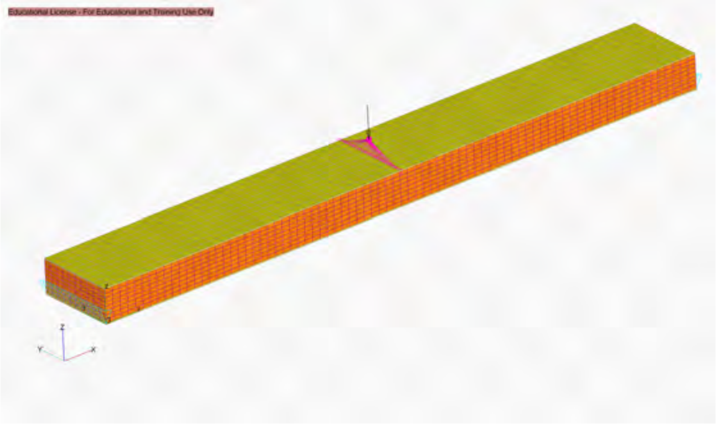

Figure 4.21: Three Point Bending Test Finite Element Model

Models to replicate each test series are made where the face lamina are oriented at 0°, 90°, and 45° degrees. Both reference and estimated properties are compared for these specimens, and using the virtual specimen dimensions the same ISO Standard 14125 method is used to derive the flexural modulus from the load and displacement of the control point. The resulting derived flexural stiffness's are shown in Table 4.14.

Table 4.14: Experimental Flexural Stiffness Values from 3-Point Bending Test

Identifier	D_f (ISO) [N mm]	D_f (Ref.) [N mm]	D_f (Est.) [N mm]	Diff. (Ref.)	Diff. (Est.)
0 DIR Series	873,537	1,263,514	871,630	44.643%	-0.218%
45 DIR Series	1,436,806	2,010,235	1,292,375	39.910%	-10.052%
90 DIR Series	1,004,392	1,119,888	865,711	25.799%	-13.807%

Comparing the results with the experimental tests shows that the reference material properties overestimate the measured flexural stiffness from 25-45%. Alternatively the estimated material properties underestimate the flexural stiffness up to -15%. This result shows a clear uncertainty regarding the stiffness of the non-crimp fabric laminates used in the plate but also the blade and blade section structures. The effect being the models analysed for the blade section likely show an artificially stiff behaviour which may be a factor in the determination of the breathing mode shapes.

4.2.7. Blade Section Estimated Materials

Considering the large effect the estimated material properties has on the sample plate mode frequencies, the blade section is revisited to examine if it is similarly affected. The estimated properties are calculated for the laminates of the blade and they are replicated using the data sheet parameters and rule of mixtures with composite laminate theory as described in Section 4.1.4 and appendix A. For each laminate the fibre volume content is assumed to be correct and the lamination properties including the ply thickness are calculated with this as the driving parameter. All non-crimp fabric laminates are changed to the estimated values, except for the UD spar materials as this is deemed accurate considering its mechanical testing. The estimated material properties using rule of mixtures for the blade are shown in Table 4.15.

Table 4.15: Blade Rule of Mixtures Estimated Materials Laminate Properties

Material	Angle	E_1[MPa]	E_2[MPa]	G_{12}[MPa]	υ_{12}	V_f	t[mm]	ρ[kg/m^3]
UD	0°	44151	14526	3699	0.3	55%	0.827	1948
2AX45 (Est.)	±45°	7112.60	7049.07	6556.45	0.525	50%	0.6183	1860.15
2AX90 (Est.)	0°/90°	13250.26	14555.32	2303.24	0.0594	50%	0.6412	1860.15
3AX (Est.)	0°/±45°	20047.05	7229.95	3813.13	0.5547	50%	0.9153	1860.15
Baltek SB.100 [4]	-	2526	2526	187	0.3	-	19.4	291
C70-55 (dry) [3]	-	-	-	-	-	-	-	60
C70-55-5 mm [3]	-	55	55	22	0.3	-	5	596
C70-55-10 mm	-	55	55	22	0.3	-	10	384
C70-55-15 mm	-	55	55	22	0.3	-	15	314
C70-55-20 mm	-	55	55	22	0.3	-	20	279
C70-55-20 mm (Spar)	-	55	55	22	0.3	-	20	180

The blade section model is updated using the rule of mixtures estimated materials of the blade and is subject to a free-free modal analysis. The estimated material model is correlated in a MAC matrix with the shaker test modal model in Figure 4.22a. For the purposes of comparison the previous model iteration of the pressure side glue joint from Section 3.2.12 is also correlated with the shaker test with a MAC matrix in Figure 4.22b. The correlations show a large improvement in MAC value of the fourth and fifth experimental modes with FE modes 3 and 4 respectively. No change in the correlation with the first three experimental modes is observed, including the first breathing mode. However the result also shows that some of the higher frequency modes appear to have changed order, and have reduced correlation with the estimated materials finite element model.

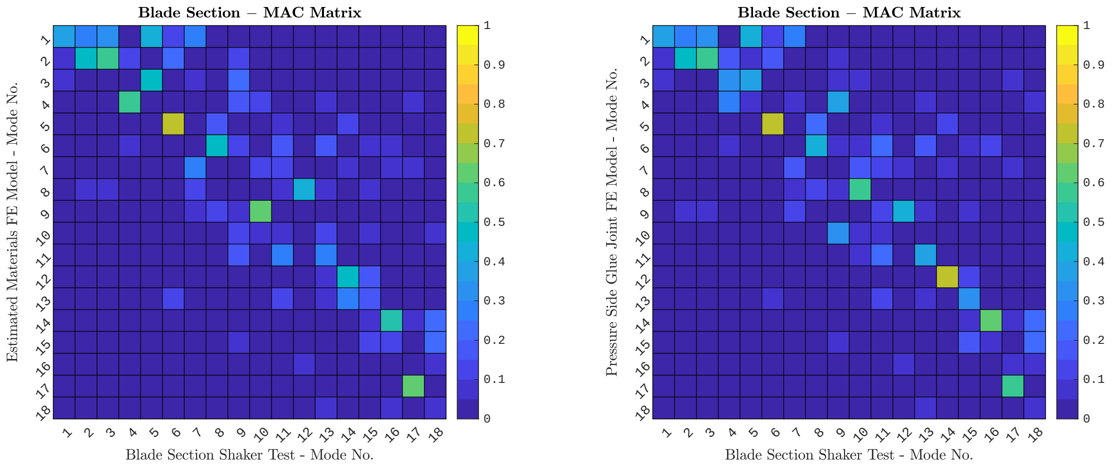

(a) Blade Section Estimated Materials FE Model - Shaker Test MAC Matrix (b) Blade Section Pressure Side Glue Joint FE Model - Shaker Test MAC Matrix

Figure 4.22: Blade Section Estimated Materials Experimental Correlation Comparison

A modal correlation of the estimated material model is also made with the pressure side glue joint model shown in Figure 4.23a. This FE model correlation confirms the results of the experimental correlations showing significant changes to FE modes 3 and 4. It also shows reduced MAC values for the higher frequency modes indicating a change of shape consistent with the experimental correlation plots.

A frequency comparison of the estimated material FE model with the experimental modes and other finite element models is shown in Figure 4.23b. The mode frequencies show a very significant reduction, significantly lower than any of the previous topology changes. Interestingly the first mode shows a very close frequency to the experimental breathing mode despite having low MAC value correlation. While a large frequency reduction was expected, it suggests perhaps that the estimated material properties may not be accurate for the blade model as the frequencies appear much too low relative the experimental modes. Another possibility is that the ballast chamber has an even more significant effect than previously assumed on the blade section mode frequencies, however this is difficult to know considering no design information is available for it.

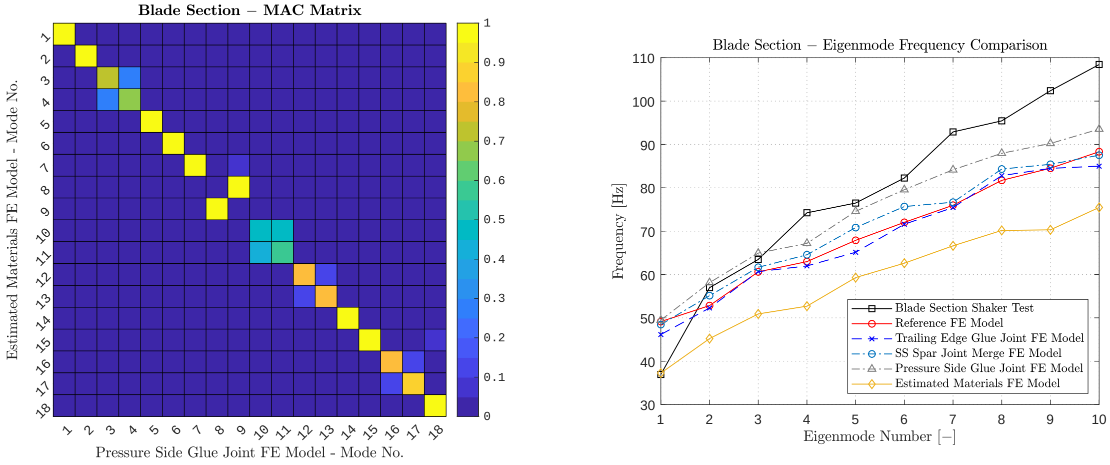

(a) Blade Section Estimated Materials FE Model - Pressure Side Glue Joint FE Model MAC Matrix

(b) Estimated Materials FE Model Eigenmode Frequency Comparison

Figure 4.23: Blade Section Estimated Materials FE Model Modal Comparison

4.2.8. Material Sensitivity Analysis

With the validity of the reference and estimated material properties used in the plate analysis being questionable, a study to examine the sensitivity of the plate mode shapes and frequencies to changes in the material properties is made. By examining how the modal behaviour changes for different material parameters an understanding of which properties most affect different modal behaviours can be very useful. The study is limited to examining the sensitivity of the first three modes of the sample plate, the mode shapes are shown in Figure 4.24.

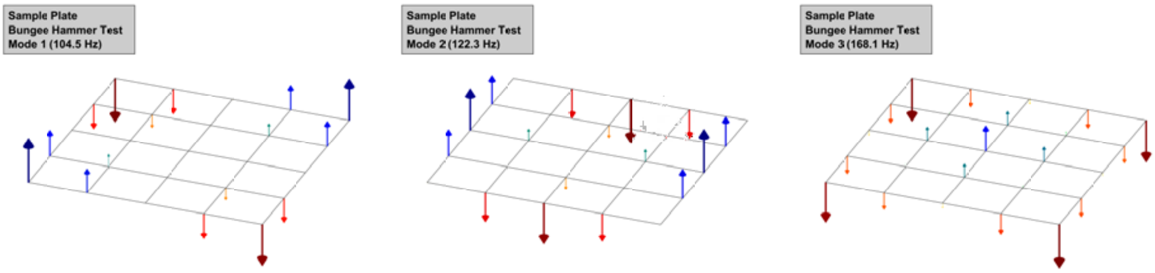

(a) Mode 1: Torsion (b) Mode 2: Saddle (c) Mode 3: Breathing

Figure 4.24: Sample Plate Bungee Hammer Test Identified Mode Shapes 1-3

To conduct the sensitivity analysis the sample plate estimated materials are used as a baseline for the variations. The baseline material properties are altered by different scaling factors and these altered property models are subject to free-free modal analysis in MSC NASTRAN. The modal results of the altered models are then compared with the experimental modal parameters. The sample plate *CQUAD4* finite element model configuration with 10 mm size elements is used to conduct the sensitivity analysis.

The material model of the face laminate is considered as an transversely isotropic material using *MAT8* material definition in NASTRAN with the core material specified as isotropic using *MAT1* material definition. The transversely isotropic face lamina consists of 4 explicit mechanical parameters E_1, E_2, G_{12}, and ν_{12} as well the implicit parameter ν_{21} in addition to the mass density parameter ρ. The core material only has 2 explicitly defined mechanical parameters E and G, with ν being an implicitly defined parameter and ρ as the density. These materials are then assembled in a *PCOMP* composite property definition where each layer is defined with a thickness t and a layer rotation angle θ. The modal parameter sensitivity is mainly focussed around the variation of these explicitly parameters. For each sensitivity analysis the material parameters are varied by ±50% using 2% increments for 51 models per analysis.

The first parameters to be examined will be uniform scaling of the '2AX45' lamina moduli E_1 and E_2, in addition to adjusting the ratio of the moduli E_1/E_2. These moduli are subject to a uniform scaling by a parameter K_{EE} varying the values by ±50%, this is shown in Equation (4.21). To adjust the ratio of the moduli the parameter K_{ER} is made to represent the ratio E_1/E_2, and additionally a requirement is set that the average of the two moduli is constant resulting in Equation (4.22).

$$\begin{aligned} \tilde{E}_1 &= K_{EE} \cdot E_1 \\ \tilde{E}_2 &= K_{EE} \cdot E_2 \end{aligned} \tag{4.21}$$

$$\begin{aligned} \tilde{E}_1 &= K_{ER} \cdot \tilde{E}_2 \\ \tilde{E}_2 &= \frac{E_1 + E_2}{K_{ER} + 1} \end{aligned} \tag{4.22}$$

The set of property scaled models are each subject to a free-free modal analysis and the first 3 modes are identified with the aforementioned experimental modes. The identified mode eigenfrequencies are normalised with respect to the experimental modes and plotted with the modal correlation MAC values over the property scaling. The modal sensitivity plots for the uniform and ratio scaling of the principal moduli of the face lamina are shown in Figure 4.25.

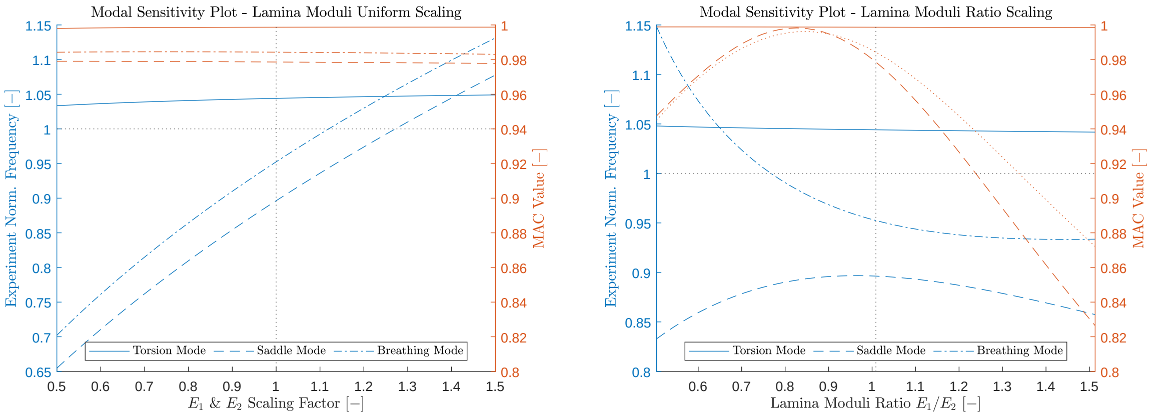

(a) Lamina Modulus Uniform Scaling K_{EE}

(b) Lamina Moduli Ratio Scaling K_{ER}

Figure 4.25: Modal Sensitivity Plot Lamina Moduli Collective Scaling

The sensitivity plots show that the first three mode shapes are unaffected by the uniform scaling to the principal moduli. The torsion mode eigenfrequency of the sample plate also was relatively unaffected by the changes to the uniform moduli scaling. However the saddle and breathing modes showed a high but equivalent sensitivity to the scaling, with the breathing mode pairing the experimental frequency at 12% scaling, and the saddle mode at 28%. Examination of the scaling of the moduli ratio similarly only affected the saddle and breathing modes in a non-linear fashion. The mode shape correlations shows a clear maximum around a ratio of 0.827., indicating a bit of anisotropy in the laminate. The mode frequencies also show a non-linear behaviour with the breathing mode increasing for lower moduli ratios. Conversely the saddle mode appears to already close to its maximum frequency. Its clear the modulus ratio has a very high sensitivity on the modal parameters. The plots clearly show the estimated laminate properties are underestimated and that the ratio of E_1/E_2 is too high.

The next parameters to be examined are the individual scaling of the face lamina principal moduli E_1 and E_2. Here a factor is applied to each moduli, as a consequence of this the ratio between E_1 and E_2 are changed this has an effect on the implicit parameter ν_{21}. The scaling of the material parameters are shown in Equations (4.23) and (4.24). The modal sensitivity plots for scaling of the lamina E_1 modulus is shown in Figure 4.26a, scaling of E_2 is shown in Figure 4.26b.

$$\begin{aligned}\tilde{E}_1 &= K_{E1} \cdot E_1 \\ \tilde{\nu}_{21} &= \nu_{12} \cdot \frac{E_2}{K_{E1} E_1}\end{aligned} \tag{4.23}$$

$$\begin{aligned}\tilde{E}_2 &= K_{E2} \cdot E_2 \\ \tilde{\nu}_{21} &= \nu_{12} \cdot \frac{K_{E2} E_2}{E_1}\end{aligned} \tag{4.24}$$

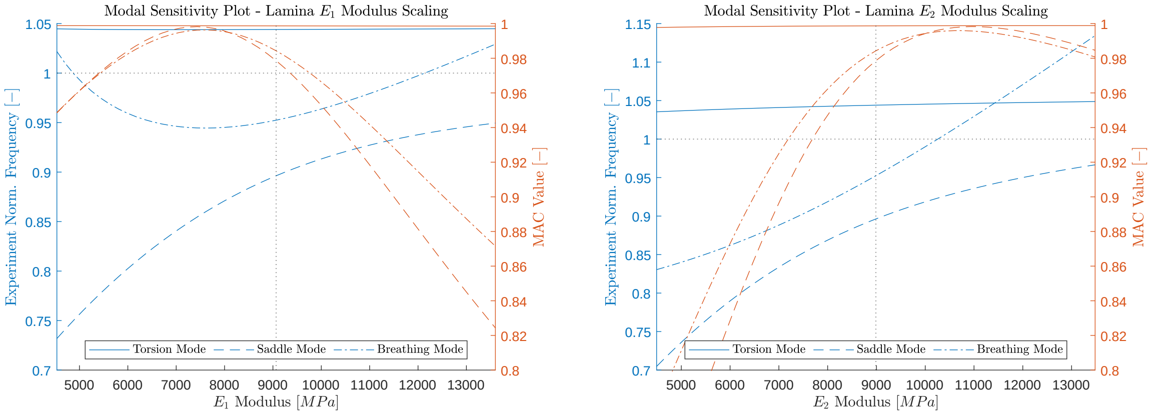

(a) Lamina $\tilde{E}_1$ Modulus Scaling

(b) Lamina $\tilde{E}_2$ Modulus Scaling

Figure 4.26: Modal Sensitivity Plot Independent Lamina Moduli Scaling

The scaling of the independent lamina constants show a high similarity to the results of uniform and ratio moduli scaling. For both lamina moduli the torsion mode frequency and modes shapes are unaffected. The response of the saddle and breathing modes show clearly to be a super position of the uniform and ratio scaling. The maxima for the mode shape correlations of both the E_1 and E_2 scaling correspond to the same moduli ratio of 0.827 as predicted in the ratio scaling. The frequency behaviour of the modes is also clearly a super position of the uniform and ratio scaling. The plots suggest the same as the collective scaling plots, E_1 and E_2 are both under predicted and E_2 should be higher to reach the approximated ratio.

The next properties to be examined are the coupling parameters major poisson ratio ν_{12}, and the in-plane shear modulus G_{12}. Similarly a scaling parameter is applied to each material property, scaling of ν_{12} also affects the implicit minor poisson ratio ν_{21}. The scaling factors applied are shown in Equations (4.25) and (4.26).

$$\begin{aligned} \tilde{\nu}_{12} &= K_\nu \cdot \nu_{12} \\ \tilde{\nu}_{21} &= K_\nu \cdot \nu_{12} \cdot \frac{E_2}{E_1} \end{aligned} \tag{4.25}$$

$$\tilde{G}_{12} = K_g \cdot G_{12} \tag{4.26}$$

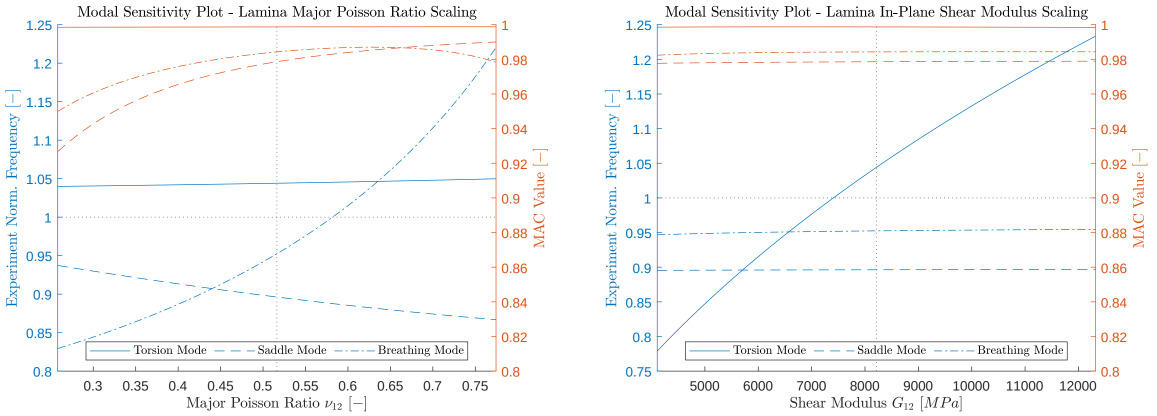

(a) Lamina Major Poisson Ratio $\tilde{\nu}_{12}$ Scaling

(b) Lamina In-plane Shear Modulus $\tilde{G}_{12}$ Scaling

Figure 4.27: Modal Sensitivity Plot Material Coupling Parameter Scaling

Scaling of the major poisson ratio ν_{12} had no visible effect on the frequency or correlation with the torsion mode. However, it has a more complex behaviour with the saddle and breathing modes. Regarding the correlation with these mode shapes it appears to have small effect with an increased poisson ratio showing marginal improvement, but a decrease having a stronger negative affect. Regarding the effect ν_{12} has on frequency, the breathing mode has a high sensitivity with increased scaling showing a large frequency increase. Alternatively the saddle mode has a lower sensitivity in the opposite trend with an increased ν_{12} showing a small reduction in frequency relative the experimental modes. The in-plane shear modulus has a much simpler effect on the modal results, where only the torsion mode eigenfrequency is sensitive to its variation. Expectedly an increased in-plane shear stiffness results in a higher mode frequency, the plot shows the estimated value slightly high where a reduction to an in-plane shear modulus of 7392 MPa would match the experimentally found mode.

The last material parameters to be examined are the core material shear modulus G_{core}, and density scaling of the lamina and core material. Scaling of the core material shear modulus G_{core} is analogous to the other studies and is an independent parameter. The density scaling of the lamina and core materials is done simultaneously to show the effect of a uniform change of the plate mass. The scaling functions are shown in Equations (4.27) and (4.28). The modal sensitivity plots for these parameters are shown in Figure 4.28.

$$\tilde{G}_{core} = K_{gc} \cdot G_{core} \tag{4.27}$$

$$\begin{aligned} \tilde{\rho}_{lam} &= K_{rho} \cdot \rho_{lam\ est.} \\ \tilde{\rho}_{core} &= K_{rho} \cdot \rho_{core\ est.} \end{aligned} \tag{4.28}$$

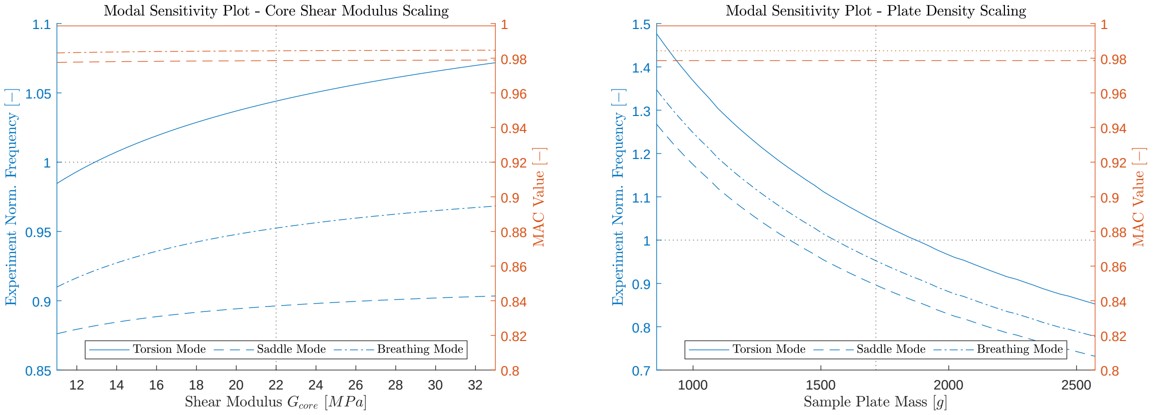

(a) Core Material Shear Modulus $\tilde{G}_{core}$ Scaling

(b) Plate Mass Uniform Density Scaling

Figure 4.28: Modal Sensitivity Plot Core Shear and Plate Mass

The plate mode shapes are unaffected by variation of the core shear stiffness, however for higher frequency modes it may have a larger affect due to the higher curvature of the mode shapes. All of the mode's frequencies are affected equally by the core shear modulus, but show a small sensitivity with marginally increased mode frequencies for higher modulus values. The plate density changes are shown by calculating the equivalent mass of the sample plate to put the changes into a greater context. Like the core shear modulus, the mode shapes are not affected by changes to the plate density however the mode frequencies show a high sensitivity. The scaling of the plate also affects all modes equally, with reduced frequencies for higher density and plate mass, a logical result. Considering the densities of the estimated material properties have already been matched to the measured mass it does not make much sense to alter this value.

The last sensitivities to be examined will be the effect of the lamination parameters, namely the thickness of the face lamina t_{lam} and offset angles from the principal laminate orientation θ_{lam}. The face lamina thickness is treated the same as other parameters with a scaling parameter applied to the reference parameter value. The ply offset angle is treated differently though where a value range is predefined, in this study the offset angles of $-5°$ to $5°$ are investigated with an increment of $0.2°$. The resulting modal sensitivity plots are shown in Figure 4.29.

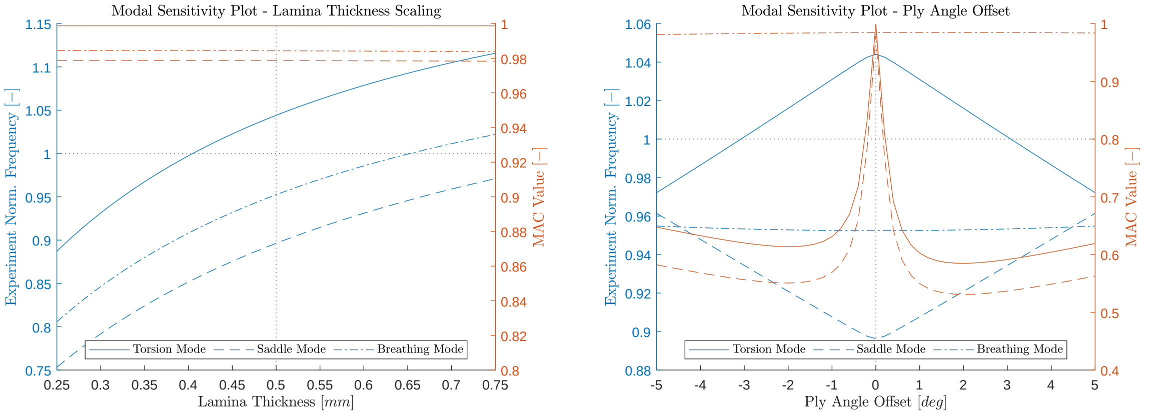

(a) Face Lamina Thickness Scaling

(b) Face Lamina Ply Angle Offset

Figure 4.29: Modal Sensitivity Plot Lamination Parameters

The scaling of the face lamina thickness showed no effect on the mode shape correlation, however it had a high sensitivity to the mode frequencies in an opposite trend to the plate density. The face lamina thickness showed uniform changes in frequency between all the modes examined. The ply offset angle however showed a highly sensitive behaviour for all metrics aside from the breathing mode shape and frequency which remained unchanged across the examined angle range. Perhaps the most interesting result is the very high sensitivity of the saddle and torsion mode shapes, where a 1° offset reduces the MAC of the torsion mode to 0.6 and that of the saddle mode to 0.55. This extreme sensitivity is almost surely to do with the high anisotropic nature of the laminate used in the sample plate. Most composite laminates like those used in the blade and blade section of this thesis are made of multiple layers of different lamina where the whole laminate behaves quasi-isotropically where the total stiffness is less affected by subtle angle changes.

Aside from this a slight asymmetry in the MAC values of these mode shape correlations is also visible, this is possibly due to the rectangular nature of the plate. The frequency of the saddle and torsion modes show an almost purely linear symmetric change with the ply offset angles.

4.2.9. Converged Properties

Using the plots of the modal sensitivity analysis from Section 4.2.8, the sample plate laminate material properties can be estimated using a best fit approach. The lamina material properties are then selected such that the finite element model matches the frequency and mode shapes of the first three experimental modes accurately.

The easiest property to estimate was that of the torsion mode as its frequency was only affected by the in-plane shear modulus of the lamina. Selecting the shear modulus at its intersection point where the experimental normalised frequency was 1.0 resulted in an approximate stiffness of 7370 MPa.

The next step involved defining the best ratio of the lamina moduli ratio previously found to be approximately 0.83. This however only partially constrained the value of the lamina principle moduli therefore a moduli uniform scaling factor was chosen such that the saddle and breathing modes were equidistant from a normalised frequency of 1.0, approximately a factor of 1.19. The normalised frequencies of the saddle and breathing modes then needed to be converged towards a normalised frequency of 1.0. The only material parameters whose change converged these mode frequencies is the major poisson ratio ν_{12}, the value at which these modes intersected was chosen approximately 0.44.

These properties were then entered into the sensitivity analysis again to check if the frequencies had converged close to unity. The non-linear behaviour of the saddle and breathing mode frequencies when altered by ν_{12} resulted in an offset of the frequencies from a normalised value of unity. The procedure to adjust the lamina scaling such that both modes are equidistant followed by an adjustment of ν_{12} to the point where the lines converged was repeated twice more where the frequencies had sufficiently converged to a final property estimation. The converged properties are shown in Table 4.16 and compared with the reference and estimated properties for the '2AX45' laminate.

Table 4.16: Sample Plate Converged Material Properties Comparison

Material	Angle	E_1 [MPa]	E_2 [MPa]	G_{12} [MPa]	ν_{12}	t [mm]
2AX45 (Ref. - t_{corr})	±45°	14145	14145	14972.5	0.633	0.5
2AX45 (Est.)	±45°	9066.22	8988.34	8213.28	0.5163	0.5
2AX45 (Conv.)	±45°	10114	12186	7370	0.420	0.5
Ref. - Conv. Diff (%)	-	39.86	16.08	103.15	50.71	-
Est. - Conv. Diff (%)	-	-10.36	-26.24	11.44	22.93	-

To facilitate comparison the reference material mechanical properties are thickness corrected to represent a lamina thickness of 0.5 mm to match those of the estimated and converged laminates. Comparing the converged results with the other properties shows that there was a significant difference between both, however the converged properties fell closer to the estimated properties. The average principal modulus lied somewhere between the other properties but also had a significant difference between E_1 and E_2 which was not predicted. For both cases the in-plane shear stiffness appeared to be highly overestimated to the converged result. Also interesting is the much smaller major poisson ratio indicating the actual laminate shows less coupling and has less anisotropy than predicted.

The converged properties are then applied in a more complete free-free modal analysis covering all the measured experimental modes, to examine if the higher frequency modes also showed a converged modal result. The mode frequencies for the converged material model are shown in Figure 4.30 for absolute and experimentally normalised scales.

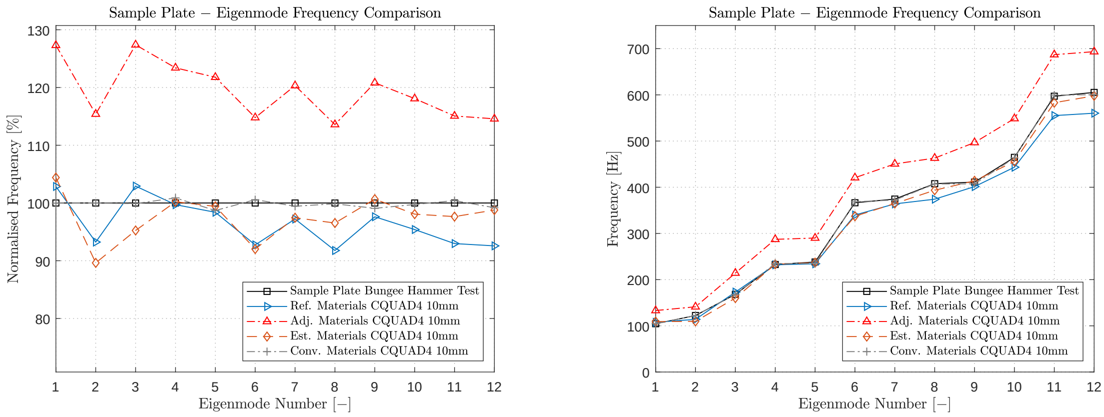

(a) Converged Materials Eigenmode Normalised Frequency Comparison

(b) Converged Materials Eigenmode Frequency Comparison

Figure 4.30: Sample Plate *CQUAD4* 10 mm Converged Materials Mode Frequency Comparison

The frequency comparison of the converged results shows a distinctly improved matching with the experimental identified mode frequencies over the other material models. The converged properties show a maximum deviation of 1.4% from the experimental modes for mode 5, a very close result. Also to be considered is the mode correlation MAC matrix with the experimental modes and estimated material model shown in Figures 4.31a and 4.31b respectively.

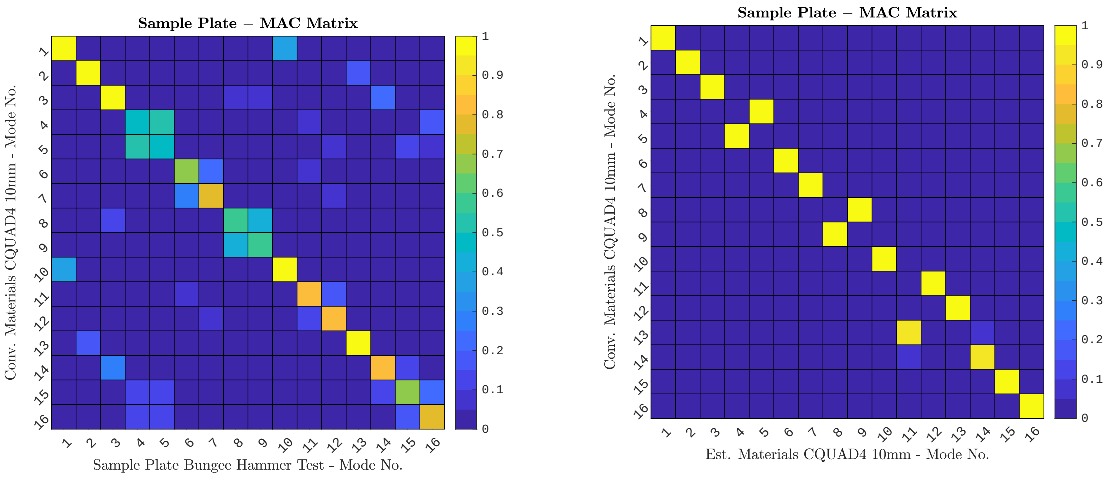

(a) Converged Materials FE Model - Bungee Hammer Test MAC Matrix

(b) Converged Materials FE Model - Estimated Materials FE Model MAC Matrix

Figure 4.31: Sample Plate *CQUAD4* 10 mm Converged Material Model Modal Correlation

The mode shape correlations with the experiment show a clear identity like pattern where the mode order is exactly correct. However the correlation of the shapes themselves are surprisingly not very different from the estimated properties model, where the only property that appeared to change was the mode order. When taking a closer look at the frequencies, the modes with poorer correlation all are very close to an adjacent mode. The reduced MAC value may be then related to symmetry of the modes because of the slight rectangular shape of the plate causing these mode shapes to become slightly coupled. It can then be said the converged sample plate materials match the properties of the sample plate very closely.

To validate this result of the modally converged materials the flexural static test results are also used for a comparison. In Section 4.2.6 a finite element model of the three point bending test was created to compare the experimentally determined flexural stiffness with the reference and estimated material property models.

The converged material properties for the sample plate are applied to the three point bending test finite element model, and the ISO standard flexural stiffness calculation is used for the three directions of the test. A comparison between the reference, estimated, and converged property models is made with the experimentally determined flexural stiffness shown in Table 4.17.

Table 4.17: Experimental Flexural Stiffness from 3-Point Bending Test Material Model Comparison

Identifier	0 DIR Series	45 DIR Series	90 DIR Series
D_f (ISO) [N mm]	873,537	1,436,806	1,004,392
D_f (Ref.) [N mm]	1,263,514	2,010,235	1,263,514
D_f (Est.) [N mm]	871,630	1,292,375	865,711
D_f (Conv.) [N mm]	938,152	1,336,553	1,080,521
Diff. (Ref.) [%]	44.643	39.910	25.799
Diff. (Est.) [%]	-0.218	-10.052	-13.807
Diff. (Conv.) [%]	7.397	-6.977	7.580

The converged results show a somewhat close result to the experiment with a difference of ±7% for the three direction sample laminates. While closer to the experiment than the estimated properties model, it is not a significantly better representation of the material properties according to the static test results. Therefore the modal test experiment results appeared to match much more closely than the static three point bending test. However, it could be stated that it is much simpler to replicate the exact circumstances of the free-free modal test than that of the three point bending test in a finite element model. For the three point bend test only direct nodal constraints were applied, the contact between the loading bars of the test rig and the test specimens were not considered so it is likely the finite element results for the bending test have a greater margin of error to that of the modal test.

In the greater context of the work, analysis of the plate showed that the choice of *CQUAD4* elements is more than adequate to represent the modal behaviour of panels. Furthermore it was also shown that an element size of 50 mm should not greatly affect the ability of finite element models to predict the shape and frequency of a similarly scaled panel structure's eigenmodes. Analysis of the plate also showed significant differences between the reference '2AX45' lamina mechanical properties with the estimated and accurately predicted properties of the plate. If the validity of the '2AX45' material properties is questionable then those of the other lamina used in the blade are as well. However, due to a lack of experimental data it is uncertain to what degree these lamina are different from their true behaviour. The reference properties of the blade then appear to be a likely upper-bound of the laminate stiffness properties. However the rule of mixtures estimated properties may not necessarily be lower-bound as it also overestimated the in-plane shear stiffness as well as the major poisson ratio. The sample plate served as a useful validation exercise to show the influence of element and material considerations on the modal response of a general plate structure, no clearly evident reason for the inability to predict the breathing modes was determined conclusively.

5

Full Blade Analysis

In Chapter 3 the effect which finite element model topology has on the modal behaviour of the blade section was investigated. The objective was to determine which model topology features contributed to the prediction first breathing mode found in the shaker test of the blade section. Chapter 4 investigated the effects of element configuration and material parameters have on the modal behaviour of a sample plate. Both these investigations identified which aspects of the model contributed the most to improving the modal behaviour relative their experimental results. This chapter uses these findings and applies them the to full blade finite element model to evaluate its efficacy in predicting breathing modes.

5.1. Blade Model Improvements

The improvements to the full blade model are applied to the original reference model of the blade detailed in Section 2.1.6. Using the understanding of how topological, material, and element configuration considerations affect the modal behaviour at the scaled level an improved model of the blade is created to measure how these translate into the global modal results. All of the relevant changes are included together into a final model where their efficacy to predict global and breathing mode behaviour is evaluated.

To create the blade model improvements the original Abaqus CAE model database was sourced. Using the database to change the model features directly allowed for more precise changes to the geometry and mesh than what previously available to use during the study of the blade section in Chapter 3. The improved model is compiled in Abaqus and then the model is translated using FEMAP to a NASTRAN input deck to allow usage of the modal correlation tools.

5.1.1. Reference Model Corrections

As initially discussed in Section 2.1.6, several inconsistencies between the data sheet material properties of Table 2.3 and the properties of the reference model of Table 2.6 were observed. The minor laminate thickness differences likely did not have a significant affect on the blade section so was not a large concern. However the largest inconsistency observed was for the material properties of the balsa core material 'Baltek SB.100', where the properties in the model were considerably lower in stiffness. As this represents a major material used for the full blade it is important the material properties are updated to reflect the data sheet values of Table 2.3. Therefore, for the improved model of the blade, the more correct data sheet properties are used for all materials.

The second consistency issue observed with the blade model was the core material thickness and density. In one large area of the model the core material thickness did not match the design drawings, this was changed such that they were consistent with the manufactured blade. Several core material regions did not match the specified density from data sheet properties, this was also corrected to ensure the correct mass distribution.

An inconsistency between the reference model and the trailing edge glue joint of the blade specified in the design drawings was also observed. Namely that in the reference model the trailing edge glue joint starts at 2.1 m span where as in the design drawings it is specified to begin at 4.0 m span. This extra 1.9 m of glue joint may have a considerable affect on the stiffness of the panel boundary at the trailing edge near the blade root. Therefore in the improved blade model the trailing edge glue joint is adjusted to match the design drawings, the difference between the models in shown in Figure 5.1.

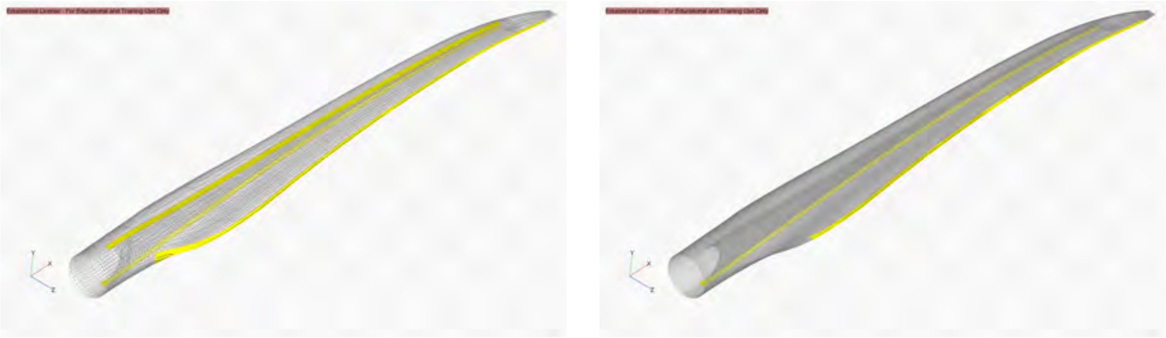
(a) Reference Model Glue Zones

(b) Improved Model Glue Zones

Figure 5.1: Full Blade Finite Element Model Trailing Edge Glue Zones

5.1.2. Topology Improvements

With the inconsistencies of the reference model addressed, improvements based upon the analysis of blade section are also implemented. The topology effects studied in Chapter 3 can be divided into four categories, the first category dealing with trailing edge joint features. The trailing edge joint features investigated included creation of a core taper region as described in Section 3.2.2 and adjustment of the glue joint length in Section 3.2.8. The trailing edge joint was found to be a sensitive area for the mode frequencies and shapes.

To include the trailing edge joint core tapering into the complete blade model, new property zones were added along the blade span by partitioning the model geometry. The created taper property zones have a length of approximately 100 mm from the start of the glue joint. The taper is approximated by halving the local core thickness in the taper property zone, the core material at the glue joint is entirely removed. The taper ratios in the design drawings are 10 : 1 therefore for an average core thickness of 10 mm this is roughly correct. This tapering effect is visible in the section view of the improved model in Figure 5.2b. The property zones for the trailing edge taper are also visible in Figure 5.2a.

Adjusting the length of the trailing edge glue joint is not as simple to implement for the full blade compared to the blade section. For the blade section, measurement data was easily obtainable to know the average length of the glue joint as direct access to the test article was available. However no such measurements exist for the manufactured blade, there there is no basis to change the length of the glue joint from the specified design length already in the model. Therefore no changes to the trailing edge glue joint length are included for the improved finite element model.

The second category of topology changes made to the blade section concerns the leading edge joint feature detailed in Section 3.2.7. The analysis showed that the shell laminate implementation of leading edge joint showed only small changes to the mode frequencies, and little affect on the mode shapes for the breathing modes of the blade section. An attempt to include the leading edge joint feature to the full blade model was made. However as a result of how the shell surfaces and property partitions were defined and the limited tools available within Abaqus CAE, the property zones were unable to be projected onto the curved shell surfaces. As a result of these problems the leading edge joint feature could not be included into the improved finite element model. It is thought that based on the analysis of the joint in the blade section, the omission of the feature is not likely to have a considerable effect on the ability of the blade model to predict the breathing modes of the blade.

The third category of topology changes made to the blade section concerns the spar web and spar web glue joint features. These comprise the modification of the suction and pressure side spar web glue joints in Sections 3.2.9 and 3.2.12 and addition of the spar cap balsa flanks in Section 3.2.10.

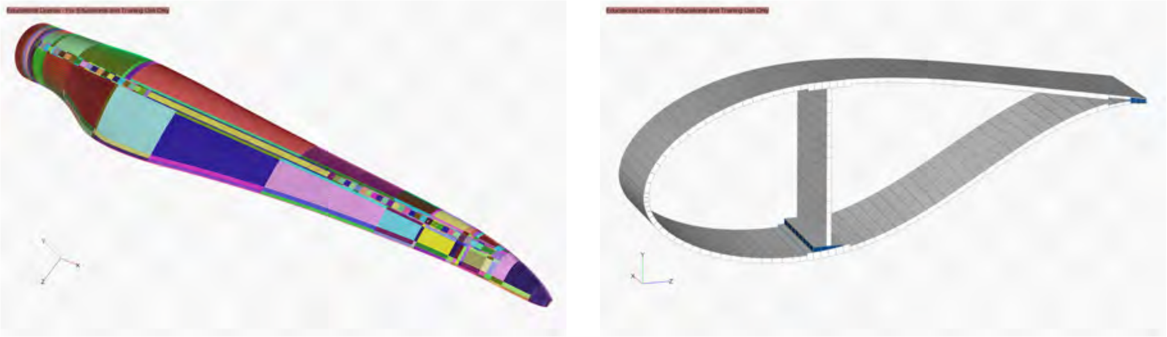

(a) Model Mesh Coloured by Property

(b) Model Cross-Section with Glue Joints

Figure 5.2: Full Blade Improved Finite Element Model Features

The removal of the suction side spar web glue elements resulted in considerable change of the modal behaviour of the blade section. Namely a large stiffening effect was observed for the mode frequencies which more closely represented the experimental modes, and a considerable change in the breathing mode shapes was observed. These effects resulted in poorer mode shape correlation for the breathing modes of the blade section, however usage of a fictitious glue joint in the model is not representative of the structure. Therefore for the improved model of the blade the suction side glue elements are removed and the spar web is directly merged with the shells, in the same method as used for the blade section. The modified suction side spar web glue joint is visible in the cross-section of the improved model in Figure 5.2b.

The modification of the bond thickness for the pressure side glue joint for the blade section resulted in no perceivable change in the mode frequencies and no affect on the low frequency mode shapes. As a result of the minimal effect and lack of measurement data of the glue thickness along the blade span, no correction to the pressure side spar web glue joint is made for the finite element model.

The addition of the spar cap balsa flanks to the blade section model showed a consistent increase in mode frequency which more closely matched that of the experimental modes, and had little to no affect on the mode shapes. The balsa flank features are added to the improved blade model by creating property zones adjacent to the spar caps with a width of 67 mm to match the design drawings. The balsa flanks use the specified core thickness of the adjacent core material, no tapering affect between the spar cap thickness and panel core is made. The balsa flanks are included in the model as they are straightforward to implement, and better represent the physical structure and panel behaviour. The balsa property regions are visible on the improved blade model mesh in Figure 5.2a.

The last category of topology changes made to the blade section concern the mass distribution of secondary structural elements, namely the addition of the spar web cable mass in Section 3.2.11. The spar web cable mass topology change resulted in little change of the mode shape and a small increase in mode frequencies caused by included hand laminates. While the inclusion of these mass effects in the small structure of the blade section was small, they can significantly affect the center of gravity for the full blade which is a sensitive parameter for the frequency of the blade global modes. Therefore modelling of the secondary structure masses is critical to match the experimental results for the full blade. The extra structure masses considered for the improved blade model include the spar web cable, ballast chamber, camera optical reflectors, blade tip, and additional internal sensors for a total additional mass of 44.97 kg. It should be noted that unlike the blade section model, the extra hand laminates used to attach the cable are not included in the improved model. The positions and masses of the secondary structures masses was documented by Johannes in [34].

In addition to the secondary structural masses of the blade, the contribution of sensor masses for the blade modal tests is also considered. The free-free modal test was made with less measurement equipment and the cables could be routed directly off the side onto the ground therefore the sensor masses are insignificant amount of additional mass. Alternatively, for the clamped modal test all the sensors needed to be routed towards the blade root, this resulted in significant additional sensor mass on the blade. These additional sensor masses are documented in [34]. The total additional sensor mass included in the blade model for the clamped modal test is 108.46 kg.

These additional masses for secondary structures and sensors are added via a *CONM2* concentrated mass element connected to the blade nodes. The concentrated masses for the free-free and clamped versions of the improved model are shown in Figure 5.3.

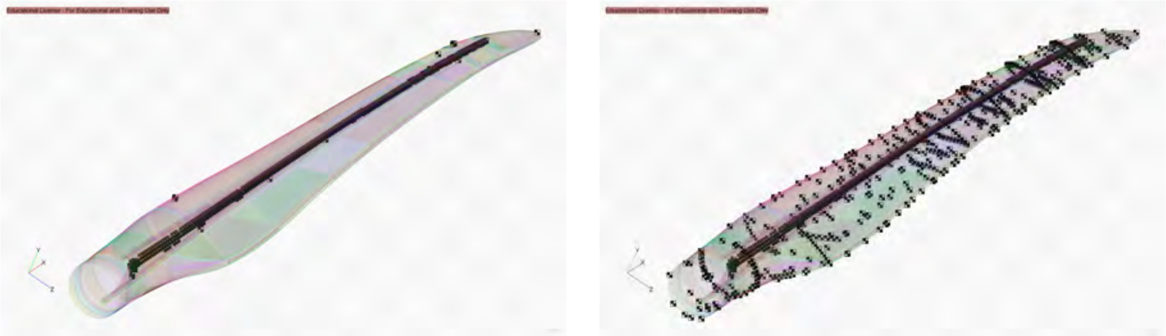

(a) Free-Free Configuration Additional Masses

(b) Clamped Configuration Additional Masses

Figure 5.3: Improved Blade Model Concentrated Masses for Free-Free and Clamped Modal Tests

5.1.3. Material and Element Improvements

The last aspects of the blade model improvements to discuss are the element and material modifications. The analysis of Chapter 4 showed that at the scale of the blade modelled 50 mm size shell element are more than sufficient to accurately model the behaviour of the trailing edge panels. Likewise the analysis for element configuration showed that *CQUAD4* elements can be used to mode panel behaviour accurately relative the other element types examined. The improved model is then remeshed to have *CQUAD4* linear shell elements with an average size of 50 mm in both span-wise and chord-wise directions.

The final change included in the improved blade model concerns the material properties. As explored in Chapter 4 on the sample plate model, a significant difference in the properties of the laminate was measured using the sample plate tests. The reference material properties appeared to over-estimate the material stiffness whereas the rule of mixtures estimated properties under-estimated the material stiffness, when compared to the modal and flexural test data. While there is sufficient basis to cast doubt on the accuracy of both sets of properties, it is fair to assume them as an upper and lower bound for the material stiffness. To control for this known variation in material properties an addition variant of the improved blade model is constructed using the rule of mixtures estimated material properties shown in Table 4.15. Considering the topology changes to the model, and different material sets, the mass and center of gravity for the finite element models are compared with the measured blade mass in Table 5.1.

Table 5.1: Mass and Centre of Gravity Comparison for SmartBlades 2 Prototype Blade Models

Identifier Material Configuration	Blade 1 - Free-Free	Blade 1 . Clamped	Imp. Model Ref. Prop. Free-Free	Imp. Model Ref. Prop. Clamped	Imp. Model Est. Prop. Free-Free	Imp. Model Est. Prop. Clamped
Mass [kg]	1793 ±42	1901±42	1641	1749	1663	1771
CoG X [mm]	6580 ±200	6580±200	6718	6806	6732	6818

Comparing the measured and FE model masses it is observed the center of gravity for the models are fairly close to the measured value and within the margin of error for the measurement. However the improved models estimate a mass difference of 152 kg less than measured masses, for both the free and clamped configurations. As the additional masses have already been considered the internal parts, the remaining masses likely originate from the laminates, core materials, or possibly excess glue of the blade. The difference in mass between the improved blade model material sets is small with the estimated materials being only 22 kg distributed over the blade.

5.2. Improved Blade Model Analysis

In this section the improved finite element blade models discussed in Section 5.1 are analysed and compared with the modal test data presented in Section 2.1.4, and the reference finite element model of the blade in Section 2.1.6. The analysis and comparison of the modal behaviour of the blade models is presented in Section 5.2.1, and the probable causes for the breathing modes are discussed in Section 5.2.2.

5.2.1. Modal Behaviour

As stated in Section 2.1.4 the prototype blade of SmartBlades2 was subject to two modal tests, a free-free test of lower sensor density and a clamped test where the root was attached to a test fixture. These tests used different measurement equipment and the clamped versions of the improved model includes these sensor masses, where as the free-free model does not. The free-free test models use no boundary conditions in the analysis, and the clamped used use a fixed constraint along the nodes at the root attachment point. Therefore four versions of the improved blade model are used, two models using the reference material set *'Imp. Model Ref. Mats Free-Free'*, *'Imp. Model Ref. Mats Clamped'* and two models using the rule of mixtures estimated material set *'Imp. Model Est. Mats Free-Free'*, *'Imp. Model Est. Mats Clamped'*. These four models are subject to a linear modal analysis within NASTRAN and the results are compared here with the experimental modal tests and the reference finite element model configuration.

The results of the improved model with reference materials is examined first. The modal correlation MAC matrices comparing the models with the experimental modal models is shown in Figure 5.4. Similarly the improved blade models are also correlated directly to the reference finite element model from Section 2.1.6 in the MAC matrices shown in Figure 5.5

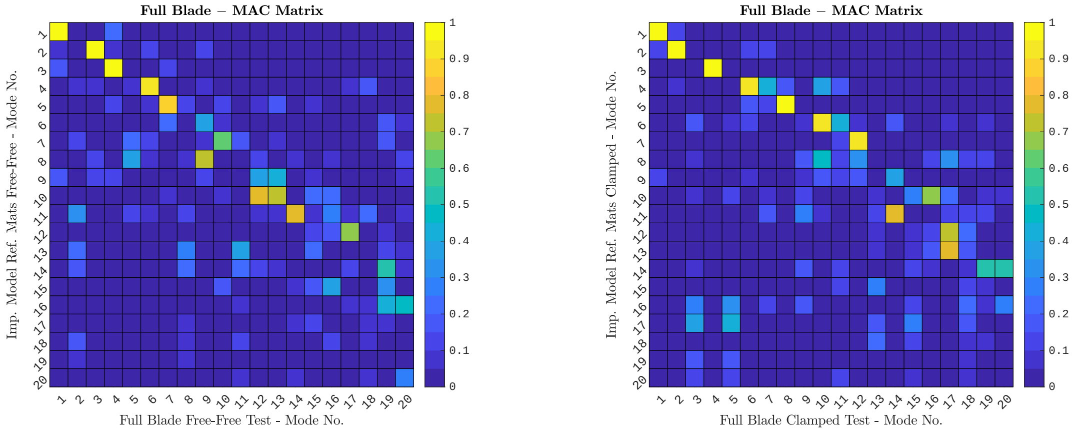

(a) Free-Free Configuration

(b) Clamped Configuration

Figure 5.4: Improved Blade Model with Reference Materials - Blade Modal Tests Modal Correlation MAC Matrices

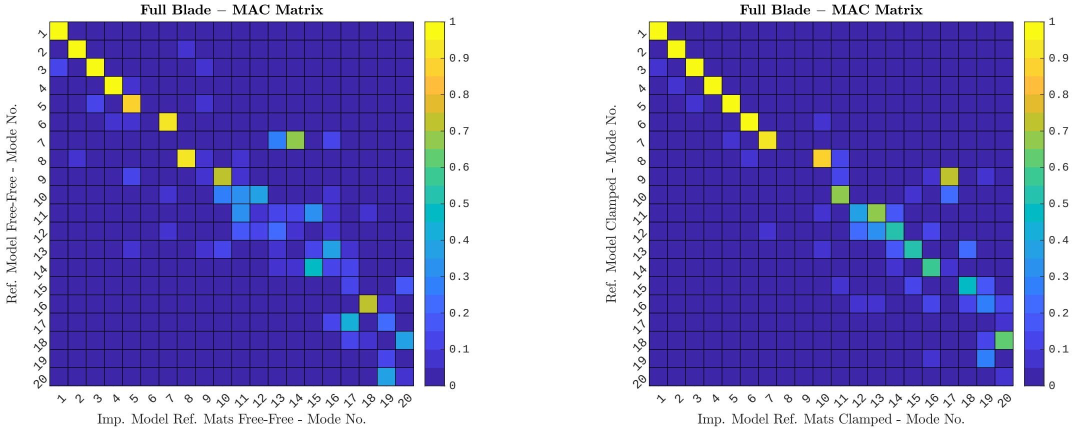

(a) Free-Free Configuration

(b) Clamped Configuration

Figure 5.5: Blade Reference Model - Improved Blade Model with Reference Materials Modal Correlation MAC Matrices

First examining the free-free configuration in Figure 5.4a the first global modes of the improved blade model show very high MAC values with the experimental modes. This matching of the global modes is very similar to the results of the reference model, additionally the higher frequency modes do appear to have shown an improvement over the reference model experimental MAC matrix shown in Figure 2.11a. A direct comparison of the reference and improved model is shown in Figure 5.5a. The direct comparison confirms this similarity of the global modes and changes of the higher frequency modes.

Recall the breathing modes for the free-free modal test experiment were modes 2, 5, and 8 for the first second and third breathing respectively. Examining the experimental MAC matrix it is observed that none of these modes have a significant correlation with improved blade model with reference materials. The FE mode which most closely replicates a breathing mode is for mode 8, they are compared in Figure 5.6. The mode shape shows some trailing edge panel motion however, as the low MAC value of 0.45 suggests it is not a very good approximation of second breathing. Furthermore, the FE mode 8 actually most closely correlates with mode 9 of the free-free test representing second bending edge-wise with a MAC value of 0.75. Even with this improvement in modal correlation for some higher frequency modes, the breathing modes are still clearly absent from the modal results of the improved blade model.

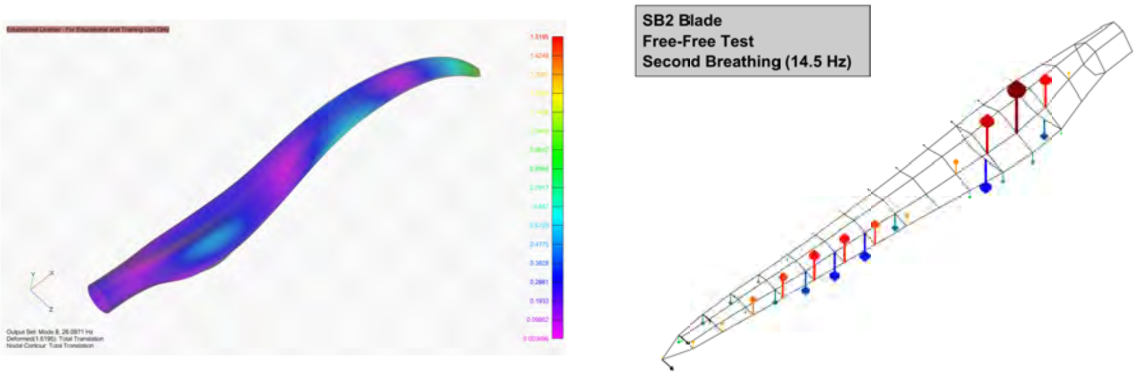

(a) Improved Blade Model with Reference Materials Free-Free Mode 8

(b) Free-Free Test Second Breathing Mode 5

Figure 5.6: Comparison of Free-Free Test Second Breathing Mode Shape with Improved Model Mode 5

Examining the clamped configuration correlation results in Figure 5.4b, shows they have a similar trend as that of the free-free configuration. Namely they show consistent identification with the global modes and further improved MAC values for some higher frequency modes. When comparing with this with the experimental correlation of the reference model in Figure 2.11b this trend is clearly evident. The mode shape correlation between the reference blade model and improved model with reference materials for the clamped configuration is shown in Figure 5.5b. The correlation shows that the first 7 global modes are unchanged, and after this the higher frequency modes showed significant change, which is consistent with the free-free results.

The breathing modes for the clamped experiment are for modes 3, 9, and 13 representing the first, second, and third breathing. Additionally some mode coupling was observed where modes 5, 7, 11 were global modes coupled with a breathing mode. The experimental correlation with the improved blade model with reference materials shows that none of the pure breathing modes showed a significant MAC value with an FE mode. The closest correlation for with a breathing mode was for FE mode 17 with a MAC value of 0.45 with mode 3 first breathing. Their mode shapes are compared in Figure 5.7. The FE mode 17 corresponds to a spar web mode coupled with a small amount of breathing in the trailing edge panels, however the amount of breathing is much smaller than the first breathing mode of the experiment. This is an interesting result because there is a link between spar and breathing motion, and they are not coupled with any other global modes. This link between the two motions suggests that the modelling of the breathing modes may be limited by the ability to the predict the stiffness of the joint from the spar web to shell panels. This is discussed briefly in Section 5.2.2.

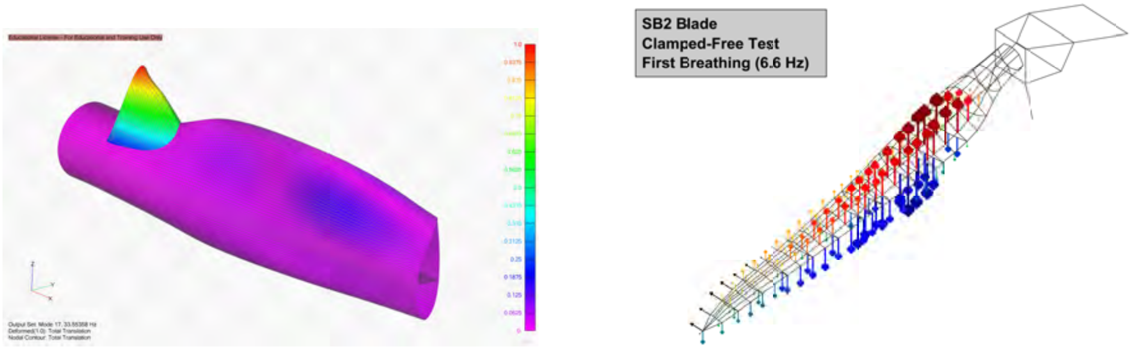

(a) Improved Blade Model with Reference Materials Clamped Mode 17

(b) Clamped Test First Breathing Mode 3

Figure 5.7: Comparison of Clamped Test First Breathing Mode Shape with Improved Model Mode 17

Next the influence of the material model is considered. The improved blade model with the rule of mixtures estimated properties is compared with the experimental modal tests in Figure 5.8, and with the improved blade model using reference materials in Figure 5.9.

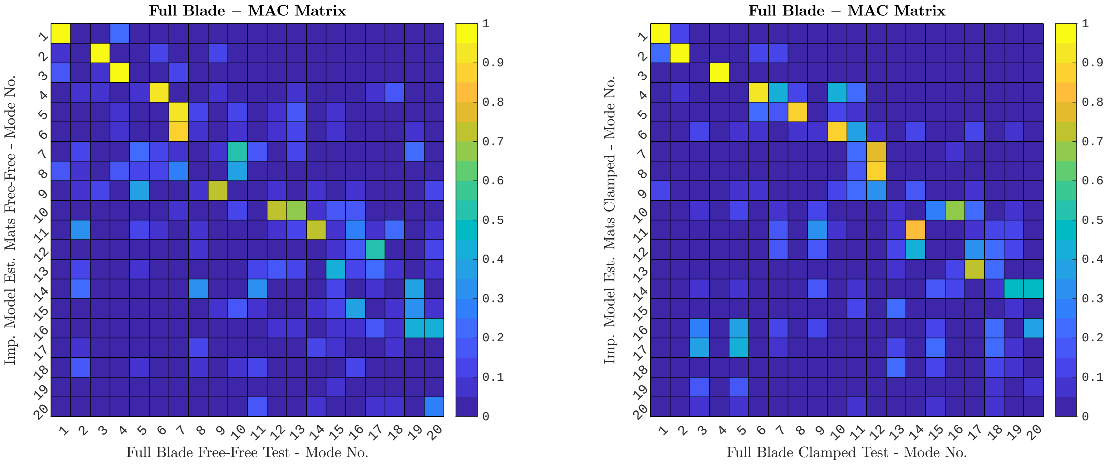

(a) Free-Free Configuration

(b) Clamped Configuration

Figure 5.8: Improved Blade Model with Estimated Materials - Blade Modal Tests Modal Correlation MAC Matrices

The free-free configuration for the improved blade model with estimated materials is examined first, with the experimental correlation in Figure 5.8a. The correlation with the experiment shows little change compared to the reference material model variant with the exception of FE mode 6 which has coupled with the third flap-wise bending mode strongly. The global mode correlation remains relatively unchanged except for FE mode 5 which has a slightly higher MAC value. The higher frequency modes show a reduced level of correlation, with lower MAC values for most. No breathing modes of the experiment have improved in correlation relative the reference material model, this consistent with the finding of Section 4.2.7. The direct correlation with the reference and estimated material models in Figure 5.9a also consistent with these findings where the low frequency mode shapes are relatively unchanged and the higher frequency modes show more change with lower MAC values.

The clamped configuration is examined with the estimated materials variant correlated with the clamped modal test in Figure 5.8b. The estimated material variant shows poorer modal correlation with the experimental global modes relative the reference materials variant. The correlation of the higher frequency modes are not significantly effected, appearing to have less change between the model variants compared to free-free configuration. The direct modal correlation between the improved blade model material variants in Figure 5.9b is consistent with these finding of small changes. Similar to the free-free configuration, no changes in correlation with the clamped modal test breathing modes is observed between the modal variants.

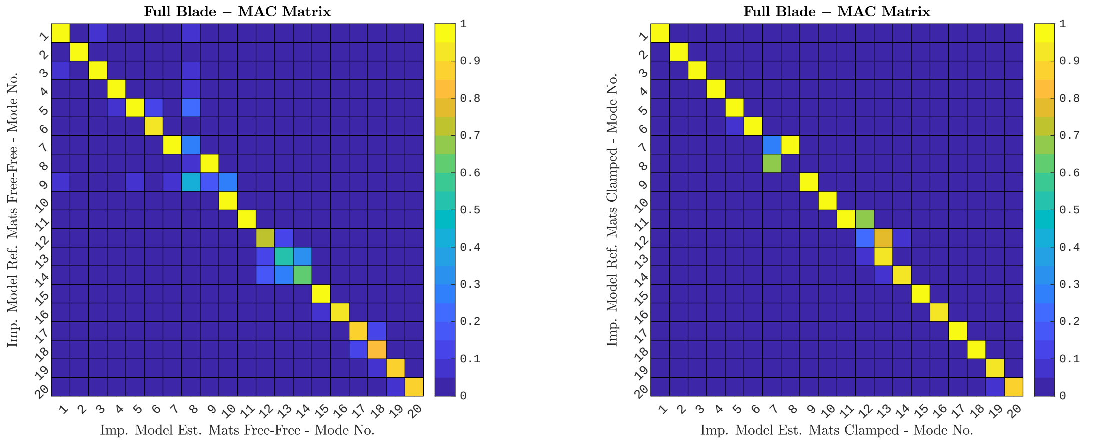

(a) Free-Free Configuration

(b) Clamped Configuration

Figure 5.9: Improved Blade Model Estimated Materials Variant - Reference Materials Variant Modal Correlation MAC Matrices

To examine how the improved blade model variants affected the mode frequencies for the identified global modes, the mode frequencies are compared for the free-free configuration in Figure 5.10, and the clamped configuration in Figure 5.11.

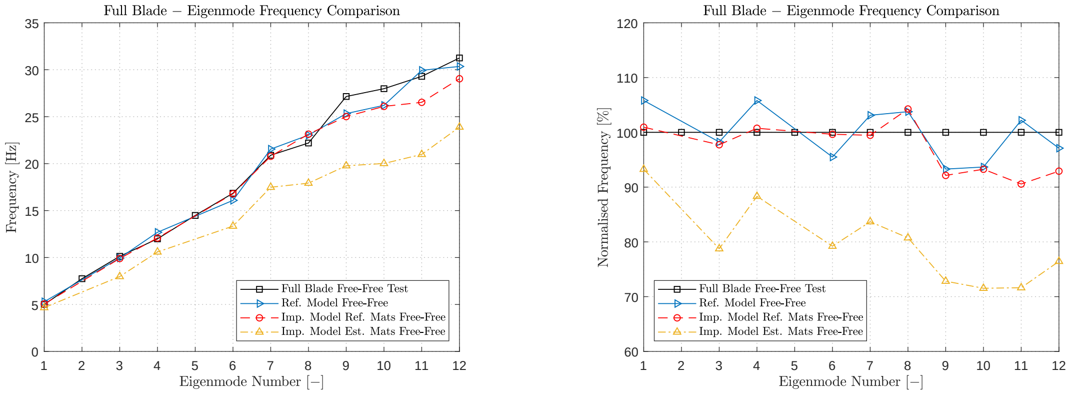

(a) Eigenmode Frequency Comparison

(b) Normalised Eigenmode Frequency Comparison

Figure 5.10: Full Blade Identified Eigenmode Frequency Comparison for Free-Free Test Configuration

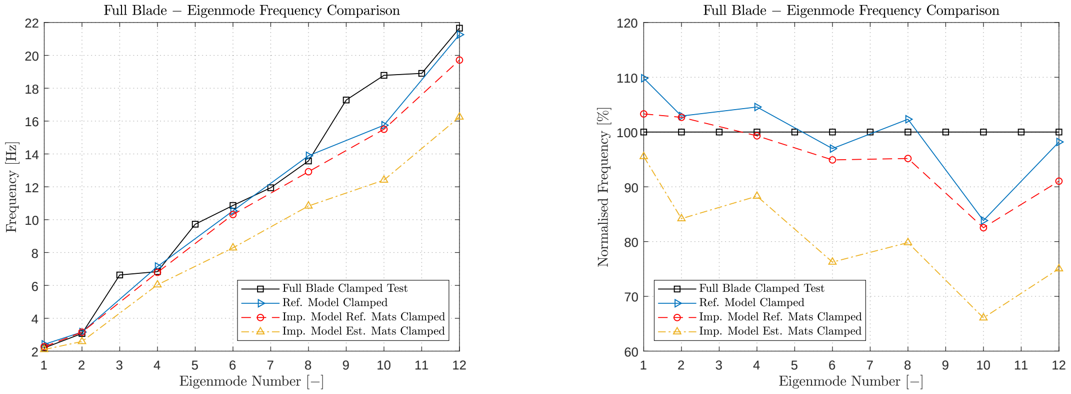

(a) Eigenmode Frequency Comparison

(b) Normalised Eigenmode Frequency Comparison

Figure 5.11: Full Blade Identified Eigenmode Frequency Comparison for Clamped Test Configuration

The mode frequency comparisons show that the improved blade model with the estimated material set consistently underestimates the global mode frequencies by $10-30\%$ for both the free-free and clamped test configurations. The reduced stiffness of the materials appears to have strongly affected blade modal frequency behaviour, this reduction in mode frequency is consistent with the results of the blade section analysis using the estimated materials in Section 4.2.7. The estimated materials showed much better behaviour for the sample plate that for the blade, this may be related to the assumed fibre volume content or manufacturing parameters of the blade, more likely its attributed to the inaccuracy of the method to predict the stiffness of non-crimp fabrics. Nonetheless it is shown that the rule of mixtures method to estimate laminate stiffness from data sheets is not applicable for large wind turbine structures and the material properties should preferably be obtained via mechanical testing.

The improved blade model with reference material properties appears to have the closest matching with the experimentally determined mode frequencies. However this is primarily for the low frequency global, for the higher frequency modes it appears to under-predict the frequencies relative the reference blade model, this is observed for both the free-free and clamped test configurations. The frequency behaviour has sightly changed however it largely remains very close to the mode frequencies of the reference model. This illustrates the sensitivity of the blade mode frequencies to the material properties, and how the laminate properties should be properly characterised via mechanical testing. In terms of the global identified modes shown it appears the topology changes did not strongly affect mode frequencies. The reference blade model, and variants of the improved blade model all significantly under-predict the clamped modal test the torsion mode 10, indicating that the in-plane shear stiffness of the panels is likely underestimated.

The examination of the mode shape correlations between the improved model variants and the experimental modal tests show that generally the improved blade model has marginally higher MAC value correlation with the experimental modes. This was mostly evident for the free-free test where the MAC values for all global modes improved, whereas the global modes for the clamped test saw less change. The largest improvements in correlation seen by the improved blade model variants concerned the higher frequency modes which indicates the structure is better represented over the reference model. The comparison of the material sets showed that generally the rule of mixtures estimated material properties did not significantly change or improve the correlation with the experimental modal tests over the reference material set, also supported by the mode frequencies. The improved blade blade models did not yield any improved correlation with the breathing modes relative the reference model, suggesting the source of the discrepancy was not implemented in a change that was investigated in the thesis. However some amount of coupling between spar motion and breathing motion was observed, this is discussed further in Section 5.2.2.

5.2.2. Breathing Modes

The improvements to the blade while supported by the analyses in Chapters 3 and 4, did not result in any of the breathing modes being successfully identified by the improved blade models. Therefore, it is examined here to what may be the probable causes for the discrepancy between finite element model and modal test data.

The material analysis of Chapter 4, showed that the sample plate material stiffness was underestimated compared to modal and flexural test data. However when applied to the blade section in Section 4.2.7, and in the improved blade model in Section 5.2 this appears to significantly reduce the mode frequencies diverging from the experimental and reference property results. It may be the case that for the simple laminate of the sample plate this was applicable but for the thicker more quasi-isotropic laminates contained in the panels this rule of mixtures estimate is no longer appropriate. It can then be stated that the material stiffness does not appear to be a significant factor in the modelling of the breathing modes.

The model topology analysis of Chapter 3 showed that the model features which affected the mode shapes of the blade section most significantly were all related to the trailing edge joint, or spar web and spar web connections. These features all occur around at the boundaries of the trailing edge panels, as identified in the thesis these were the primary focus for the topology changes. However the topology changes primarily focused on the panels themselves such tapering of balsa flanks and the modelling of the glue elements. However, the spar web connection to the glue flange or spar cap is never examined. All implementations of this T-joint use a common node between the flange shells and the spar web shells as shown in Figure 5.12.

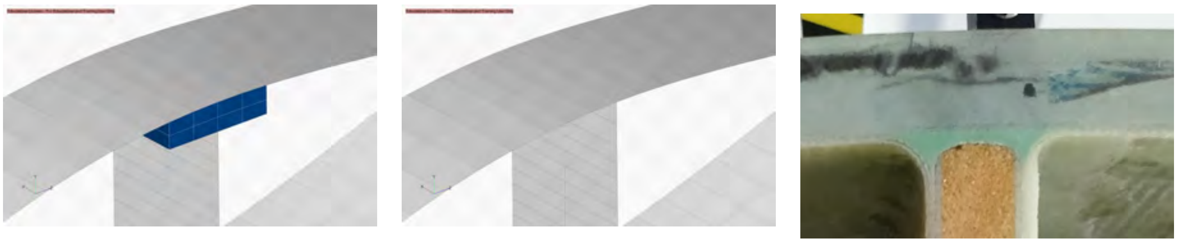

(a) Finite Element Spar Web to Shell Glue Connection

(b) Finite Element Spar Web to Shell Merged Connection

(c) Blade Section Spar Web to Shell Connection

Figure 5.12: Spar Web to Shell Connection Comparison

This type of merged joint between the shear web and shell is a commonly used connection method for analysis of wind turbine blades for full 3D shell analyses as seen in [8, 25, 41, 42, 58]. While this type of joint will behave very closely to a lap joint in the span-wise direction, hence its usage to model a blade, its implementation with respect to modelling breathing modes may be unrepresentative. By merging the nodes of the spar web with the shell directly or to a glue flange there is one common rotational degree of freedom in the section plane at the joint. This effectively creates a rigid connection between the spar web shell element and the glue joint flange or blade shell.

Examining Figure 5.12c, the manufactured joint consists of two low radius fillets with 2 layers of glass fibre, and the spar web core material bonded to the blade shell. The true stiffness of the joint is unknown, however it is possible that in the section plane this joint is not adequately represented by the conventional attachment method used in literature. This rigid connection in finite element likely couples the bending of the panels with the bending of the leading and trailing edge panels resulting in a response which is overly constrained. The observation in Section 5.2 that the improved blade model mode 17 had coupling between a spar mode with breathing motion is also evidence toward this hypothesis.

Modelling of composite T-joints for wind turbine blades has been examined in literature [53, 55]. However, these primarily examine strength affects do not consider the bending stiffness of the joints or how it may effect the behaviour of the attached panels.

6

Conclusions and Recommendations

In this thesis modal test results for the SmartBlades2 wind turbine prototype blade were examined. These modal tests detected breathing modes, consisting of out-of-plane motion of the trailing edge panels, which were not predicted by a conventionally constructed shell model of the blade. To determine the possible causes and answer the research questions the analysis was broken down into three parts, an examination of the model topology effects, a study on the sensitivity of modal behaviour to element and materials, and lastly an analysis of an improved model to compare with the experimental modes of the blade.

First examined was the influence of the blade topology by comparing modal test data of a cut out section of the blade and its relevant finite element model. Many aspects of the model topology were altered to better reflect the manufactured product. Features examined for the blade section included the influence of improved modelling of the leading and trailing edge glue joints, shell curvature and geometry, spar web glue joint modelling, as well as the effect of tertiary mass elements for the lightning cable. These topology changes generally improved the correlation with the experiment modal models, particularly the features relating to modelling of the glue joints of the spar and shells. However, none of the topology improvements made to the blade section models revealed or showed any breathing mode similar to the first experimental mode measured in the blade section tests.

The second topic examined was the effect of finite element configurations and material properties on modal behaviour of plate structures. To establish the effect of these parameters, a witness panel plate using the same materials as the SmartBlades2 panels was modelled. The sample plate was subject to mutual comparisons between finite element model configurations comparing element type and size. The analysis showed that higher fidelity element configurations offer no advantage over linear shell elements for prediction of modal behaviour and that element size does not have a sensitive effect to the low frequency modes of the plate.

To determine the effect of materials on the modal behaviour, the sample plate was subject to modal and stiffness tests. This testing revealed the supplied material stiffness was greater than the measured stiffness. Thus an estimated set of material properties was created using rule of mixtures and composite laminate theory from the manufacturing data. Conversely this estimated set was closer but smaller than the measured stiffness. To further explore the effect of the materials a sensitivity analysis was conducted where the material parameters were varied and then compared with the modal results of the sample plate. From this a converged set of materials was found for the plate. Comparing the stiffness of the measured, specified, estimated, and converged properties showed relatively close agreement, except for the specified properties which greatly over predicted the stiffness. The variation of material properties appeared to have a sensitive effect on the mode frequencies and mode order of the plate but did not significantly change the mode shapes.

Finally, these topological, element, and material studies were then applied to an improved version of the finite element model for the SmartBlades2 prototype blade. The improved model utilising the reference properties did yield better modal comparisons with the blade test in regard to the global modes. However no breathing modes were predicted.

The research objective of the thesis, as stated in Chapter 1, was to create a set of validated modelling practices to be able to predict breathing modes in wind turbine blade structures. In this regard some progress has been made, as the conducted analyses showed that the explored changes in model topology, element configuration, and materials did not significantly effect or improve the ability of the finite element models to predict breathing modes. Based on these finding the main research question can be re-examined and answered.

> *How and to what accuracy can 'breathing', 'pumping', or 'panel' type eigenmodes of wind turbine blade structures be predicted in finite element simulation?*

It is evident that based upon of the findings of the thesis that breathing modes have not been able to be predicted in finite element simulation of the blade. This leaves an open question as to why the changes reflected in the model were unable to predict the desired behaviour, and what should be investigated further.

The analysis of the element and material effects on the sample plate clearly showed that the element type and size do not significantly affect the behaviour of the low frequency mode shapes, which are most analogous to the breathing modes of the plate. Therefore, with regard to modelling of the panels, this is unlikely to be the cause of discrepancy. With respect to the material analysis there is more ambiguity due to high variance between provided, modelled, and measured properties for the plate. Therefore there is sufficient reason to cast doubt on the validity of the material properties in stiffness but also in regard to the material density. However, as the analyses of the blade section and improved blade model showed, the differences between the properties appeared to mostly affect frequency behaviour of the vibration, and the mode shapes were relatively unaffected. Therefore it is unlikely these material and density differences are the cause for the discrepancy in prediction of the breathing mode shapes.

The analysis of the blade topology focused primarily on examination of the boundary conditions of the panels, namely the trailing edge and spar web joints. The analysis showed these areas to be the most sensitive to changes in mode shape however none of the implemented changes yielded the prediction of breathing modes, whether applied to the blade section or to the complete blade. As discussed in Section 5.2.2, there is a strong likelihood the connection of the spar web to the blade shells or glue flanges, couples the stiffness of the panel boundary to the spar web bending stiffness by assuming a rigid connection between them. As the merged T-joint approach between the spar web and shell is the most commonly employed for modelling full 3D blade shell models, this could explain why little literature examining these modes for full size blades has been made.

In addition to the spar web connection, some other causes can be hypothesised. Potentially the structure itself may be damaged or defective from the manufacturing process. However, the existence of any damage is unsubstantiated and furthermore the breathing modes were detected in all four blades from the Smart-Blades2 project so this error would have to be consistently applied to each blade which is unlikely.

The prevailing hypothesis for the cause of the breathing modes is the connection of the spar web to the shell. It is suggested that further analysis be conducted on the modelling of the spar web joint to compare the relative boundary stiffness between the current standard finite element connection method and more advanced models to quantify the existence of, or amount of error. Alternatively, an experimental approach could be taken to measure the behaviour of the joint by conducting modal tests of wind turbine blades, where the response of both panel and spar structures are measured. As the joint stiffness would affect both the panel and spar boundaries, it should be possible to compare experimental spar modes and predicted spar modes to draw conclusions regarding the stiffness of the joint. If further studies examining the modelling of breathing modes are made, the potential impact they could have on adhesive joint fatigue, acoustics, and turbine efficiency can be quantified potentially resulting in cost reductions for wind energy.

A

Composite Laminate Theory

In this thesis several calculations are carried out to estimate the mechanical properties of composite laminates. These calculations utilise composite laminate theory to obtain the ABD matrix and extracted engineering constants of these laminates. The process for this briefly is described using Voigt notation in this Appendix. For a more detailed examination of the underlying assumptions of composite laminate theory the book of Reddy is recommended [44].

The base unit of the laminate is the ply, it is defined by a set of properties describing its in plane behaviour. These are typically derived from experimental data, or estimated from data-sheet sources. The in plane properties of the laminate are shown in Equation (A.1).

$$E_1, \quad E_2, \quad G_{12}, \quad \nu_{12}, \quad \nu_{21} \tag{A.1}$$

The ply level properties can be assembled into a the Q matrix, describing the mechanical behaviour of ply relating stress to strain shown in Equation (A.2):

$$\begin{bmatrix} \sigma_1 \\ \sigma_2 \\ \sigma_6 \end{bmatrix} = \begin{bmatrix} Q_{11} & Q_{12} & 0 \\ Q_{21} & Q_{22} & 0 \\ 0 & 0 & Q_{66} \end{bmatrix} \cdot \begin{bmatrix} \epsilon_1 \\ \epsilon_2 \\ \epsilon_6 \end{bmatrix} \tag{A.2}$$

The coefficients of this Q matrix are determined by the ply mechanical properties of Equation (A.1). The components of can be calculated using the relations in Equation (A.3).

$$Q_{11} = \frac{E_1}{1 - \nu_{12} \cdot \nu_{21}} \quad , \quad Q_{22} = \frac{E_2}{1 - \nu_{12} \cdot \nu_{21}} \quad , \quad Q_{12} = Q_{21} = \frac{\nu_{12} \cdot E_2}{1 - \nu_{12} \cdot \nu_{21}} \quad , \quad Q_{66} = G_{12} \tag{A.3}$$

This description of the Q matrix of the ply is within the ply's local coordinate system, referred to with numbers 126. Alternatively the global reference system is referred to with letters xys. To analyse a laminate with multiple plies of different thickness and orientations $[\theta/.../\theta]$, the Q matrices of all the plies need to be oriented into the global reference system. This is done by using a transformation matrix T, and the use of the engineering strain to tensor strain conversion matrix R. Classical laminate theory is described using engineering strain as opposed to tensor strain, necessitating the conversion matrix. This transformation into the global reference frame requires knowledge of the relative angle θ to the local reference frame. The transformation matrices T R and global Q matrix $\left[Q_{xy}\right]$ are defined in Equations (A.4) and (A.5).

$$[T] = \begin{bmatrix} m^2 & n^2 & 2mn \\ n^2 & m^2 & -2mn \\ -mn & mn & m^2 - n^2 \end{bmatrix} \quad , \quad \begin{matrix} m = \sin\theta \\ n = \cos\theta \end{matrix} \quad , \quad [R] = \begin{bmatrix} 1 & 0 & 0 \\ 0 & 1 & 0 \\ 0 & 0 & 2 \end{bmatrix} \tag{A.4}$$

$$\left[Q_{xy}\right] = [T]^{-1} \cdot [Q_{12}] \cdot [R] \cdot [T] \cdot [R]^{-1} \tag{A.5}$$

Now with the Q matrix of every ply in the global reference system we can relate stresses and strains in a common reference frame among all plies as defined in Equation (A.6).

$$\begin{bmatrix}\sigma_x\\ \sigma_y\\ \sigma_s\end{bmatrix}=\begin{bmatrix}Q_{xx} & Q_{xy} & Q_{xs}\\ Q_{yx} & Q_{yy} & Q_{ys}\\ Q_{sx} & Q_{sy} & Q_{ss}\end{bmatrix}\begin{bmatrix}\epsilon_x\\ \epsilon_y\\ \epsilon_s\end{bmatrix} \tag{A.6}$$

Using the Q matrices for the plies in the global reference frame they can be integrated through the thickness to form the ABD matrix. The ABD matrix relates line loads and moments on a section of the laminate to the strain components for membrane and curvature as shown in Equation (A.7).

$$\begin{bmatrix}N_x\\ N_y\\ N_s\\ M_x\\ M_y\\ M_s\end{bmatrix}=\begin{bmatrix}A_{xx} & A_{xy} & A_{xs} & B_{xx} & B_{xy} & B_{xs}\\ A_{yx} & A_{yy} & A_{ys} & B_{yx} & B_{yy} & B_{ys}\\ A_{sx} & A_{sy} & A_{ss} & B_{sx} & B_{sy} & B_{ss}\\ B_{xx} & B_{xy} & B_{xs} & D_{xx} & D_{xy} & D_{xs}\\ B_{yx} & B_{yy} & B_{ys} & D_{yx} & D_{yy} & D_{ys}\\ B_{sx} & B_{sy} & B_{ss} & D_{sx} & D_{sy} & D_{ss}\end{bmatrix}\begin{bmatrix}{\epsilon_x}^0\\ {\epsilon_y}^0\\ {\epsilon_s}^0\\ \kappa_x\\ \kappa_y\\ \kappa_s\end{bmatrix} \tag{A.7}$$

The ABD matrix comprises three sub-matrices. The A matrix relates membrane loading and strain, the D matrix relates line moments to curvature, and the B matrix relates the coupling between membrane and strain. These matrices are calculated by integrating the global $Q^{(k)}$ matrices through the thickness for each layer k, where z represents the distance between the top/bottom of the ply and mid-plane of the laminate. The A, B, and D matrices are calculated using Equation (A.8).

$$\begin{aligned}A_{ij}&=\sum_{k=1}^{n}Q_{ij}^{(k)}\left(z_k-z_{k-1}\right) && \text{for} \quad i,j=x,y,s\\ B_{ij}&=\frac{1}{2}\sum_{k=1}^{n}Q_{ij}^{(k)}\left(z_k^2-z_{k-1}^2\right) && \text{for} \quad i,j=x,y,s\\ D_{ij}&=\frac{1}{3}\sum_{k=1}^{n}Q_{ij}^{(k)}\left(z_k^3-z_{k-1}^3\right) && \text{for} \quad i,j=x,y,s\end{aligned} \tag{A.8}$$

With the mechanical properties of the arbitrary laminate defined, the effective laminate moduli engineering constants can be calculated. For the purposes of this thesis, they are calculated in terms of the in-plane behaviour, but can also be derived from out-of-plane behaviour if necessary. These are derived from the inverted ABD matrix describing compliance as opposed to stiffness, referred to with lowercase letters abd and defined in Equation (A.9).

$$[abd]=[ABD]^{-1}=\begin{bmatrix}A & B\\ B & D\end{bmatrix}^{-1}=\begin{bmatrix}a & b\\ b & d\end{bmatrix} \tag{A.9}$$

The effective laminate moduli engineering constants are then calculated from the abd matrix using the relations in Equation (A.10).

$$E_x=\frac{1}{t_{lam}\cdot a_{xx}} \quad , \quad E_y=\frac{1}{t_{lam}\cdot a_{yy}} \quad , \quad G_{xy}=\frac{1}{t_{lam}\cdot a_{ss}} \quad , \quad \nu_{xy}=-\frac{a_{xy}}{a_{xx}} \quad , \quad \nu_{yx}=-\frac{a_{xy}}{a_{yy}} \tag{A.10}$$

Bibliography

[1] SmartBlades WebPage, 2016. URL `http://www.smartblades.info/English.html`.

[2] *SE 1500 Glass Datasheet.* 3B Fibreglass SPRL, 2019.

[3] *AIREX C70 Data Sheet.* Airex AG, 2011.

[4] *BALTEK SB Data Sheet.* Airex AG, 2016.

[5] C. Bak. Aerodynamic design of wind turbine rotors. In *Advances in Wind Turbine Blade Design and Materials*, pages 59–108. Woodhead Publishing Series in Energy, 2013.

[6] V. Birman and C. W. Bert. On the Choice of Shear Correction Factor in Sandwich Structures. *Journal of Sandwich Structures & Materials*, 4(1):83–95, 2002.

[7] J. P. Blasques, R. D. Bitsche, V. Fedorov, and B. S. Lazarov. Accuracy of an efficient framework for structural analysis of wind turbine blades. *Wind Energy*, 19(9):1603–1621, 2016.

[8] C. L. Bottasso, F. Campagnolo, A. Croce, S. Dilli, F. Gualdoni, and M. B. Nielsen. Structural optimization of wind turbine rotor blades by multilevel sectional/multibody/3D-FEM analysis. *Multibody System Dynamics*, 32:87–116, 2014.

[9] A. Brandt. *Noise and Vibration Analysis: Signal Analysis and Experimental Procedures.* John Wiley & Sons, Ltd, Chichester, UK, 2011. URL `http://doi.wiley.com/10.1002/9780470978160`.

[10] P. Broøndsted and R. P .L. Nijssen. *Advances in wind turbine blade design and materials.* Woodhead Publishing Limited, 2013.

[11] T. G. Carne, D. T. Griffith, and M. E. Casias. Support conditions for free boundary-condition modal testing. Technical report, Sandia National Laboratories, Albuquerque, NM, United States, 2007.

[12] P. N. Castelos and C. Balzani. The impact of geometric non-linearities on the fatigue analysis of trailing edge bond lines in wind turbine rotor blades. In *Journal of Physics: Conference Series*, volume 749, 2016.

[13] ISO Committee. Iso 14125:1998, fibre-reinforced plastic composites–determination of flexural properties, 2013.

[14] C. J. Faccio Júnior, A. C. P. Cardozo, V. Monteiro Júnior, and A. Gay Neto. Modeling wind turbine blades by geometrically-exact beam and shell elements: A comparative approach. *Engineering Structures*, 180: 357–378, 2019.

[15] A. Fathi, F. Wolff-Fabris, V. Altstädt, and R. Gätzi. An investigation on the flexural properties of balsa and polymer foam core sandwich structures: Influence of core type and contour finishing options. *Journal of Sandwich Structures and Materials*, 15(5):487–508, 2013.

[16] U. Fuellekrug, M. Boeswald, D. Goege, and Y. Govers. Measurement of FRFs and modal identification in case of correlated multi-point excitation. *Shock and Vibration*, 15:435–445, 2008.

[17] *Guideline for the Certification of Wind Turbines.* Germanischer Lloyd Industrial Services GmbH, 2010. URL `www.gl-group.com/GLRenewables`.

[18] D. Griffith and T. G. Carne. Experimental uncertainty quantification of modal test data. Technical report, Sandia National Laboratories, Albuquerque, NM, United States, 2007.

[19] D. T. Griffith. Utilization of Localized Panel Resonant Behavior in Wind Turbine Blades. In *Rotating Machinery, Structural Health Monitoring, Shock and Vibration*, volume 5, pages 93–103. 2011.

[20] D. T. Griffith and J. Paquette. Panel Resonant Behavior of Wind Turbine Blades. In *In proceedings of 51st AIAA/ASME/ASCE/AHS/ASC Structures, Structural Dynamics, and Materials Conference 18th AIAA/ASME/AHS Adaptive Structures Conference 12th*, Reston, Virigina, 2010. American Institute of Aeronautics and Astronautics. URL `http://arc.aiaa.org/doi/abs/10.2514/6.2010-2741`.

[21] D. T. Griffith, J. A. Paquette, and T. G. Carne. Development of Validated Blade Structural Models. In *46th AIAA Aerospace Sciences Meeting Exhibit*, 2008.

[22] P. Guillaume, P. Verboven, and S. Vanlanduit. Frequency-domain maximum likelihood identification of modal parameters with confidence intervals. In *Proceedings of the international seminar on modal analysis*, volume 1, pages 359–366, 1998.

[23] P. Guillaume, P. Verboven, S. Vanlanduit, H. Van Der Auweraer, and B. Peeters. A poly-reference implementation of the least-squares complex frequency-domain estimator. In *In Proceedings of IMAC* , volume 21, pages 183–192, 2003.

[24] J. Gundlach and Y. Govers. Experimental modal analysis of aeroelastic tailored rotor blades in different boundary conditions. In *Journal of Physics: Conference Series*, volume 1356, 2019. URL `https://iopscience.iop.org/article/10.1088/1742-6596/1356/1/012023`.

[25] K. Ha and J. Jeong. Stress states investigation of adhesive bonded joint between spar cap and shear webs of a large wind turbine rotor blade. *Journal of Mechanical Science and Technology*, 35(5):2107–2114, 2021.

[26] P. U. Haselbach. An advanced structural trailing edge modelling method for wind turbine blades. *Composite Structures*, 180:521–530, 2017. URL `http://dx.doi.org/10.1016/j.compstruct.2017.08.029`.

[27] P. U. Haselbach and K. Branner. Initiation of trailing edge failure in full-scale wind turbine blade test. *Engineering Fracture Mechanics*, 162:136–154, 2016.

[28] Heydlauff, W. Blade specifications of the rotor blade IWES. Technical report, Aero Dynamik Consult GmbH, 2018.

[29] Heydlauff, W. Materialspezifikation der Faserverbundwerkstoffe für das Rotorblatt IWES. Technical report, Aero Dynamik Consult GmbH, 2018.

[30] J. G. Holierhoek. Aeroelastic design of wind turbine blades. In *Advances in Wind Turbine Blade Design and Materials*, pages 151–173. Woodhead Publishing Series in Energy, 2013.

[31] F. M. Jensen, J. D. Sørensen, P. H. Nielsen, P. Berring, and S. Flores. Failures in Trailing Edge Bondlines of Wind Turbine Blades. In *Proceedings of the Risø International Symposium on Materials Science*, volume 32, pages 319–327, 2011.

[32] S. Joncas. *Thermoplastic Composite Wind Turbine Blades: An Integrated Design Approach.* PhD thesis, Delft University of Technology, 2010.

[33] M. Jureczko, M. Pawlak, and A. Mezyk. Optimisation of wind turbine blades. *Journal of Materials Processing Technology*, 167:463–471, 2005.

[34] J. Knebusch. Finite Element Model Updating of Wind Turbine Rotor Blades using Modal Data. Master's thesis, Technische Universität Berlin, 2019.

[35] I. Komusanac, D. Fraile, and G. Brindley. Wind Energy in Europe in 2019: Trends and Statistics. Technical report, Wind Europe, 2020.

[36] P. Lubrina, S. Giclais, C. Stephan, M. Boeswald, Y. Govers, and N. Botargues. AIRBUS A350 XWB GVT: State-of-the-art techniques to perform a faster and better GVT campaign. In *Topics in Modal Analysis II*, volume 8, pages 243–256, 2014.

[37] *MSC Nastran 2018.2 Quick Reference Guide.* MSC Software GmbH, 2018.

[38] *MSC Nastran 2018.2 Reference Manual.* MSC Software GmbH, 2018.

[39] M. Pastor, M. Binda, and T. Harčarik. Modal Assurance Criterion. *Procedia Engineering*, 48:543–548, 2012.

[40] B. Peeters, H. Van Der Auweraer, P. Guillaume, and J. Leuridan. The PolyMAX frequency-domain method: A new standard for modal parameter estimation? *Shock and Vibration*, 11(3-4):395–409, 2004.

[41] M. Peeters, G. Santo, J. Degroote, and W. Van Paepegem. Comparison of shell and solid finite element models for the static certification tests of a 43 m wind turbine blade. *Energies*, 11(6), 2018.

[42] M. Peeters, G. Santo, J. Degroote, and W. Van Paepegem. High-fidelity finite element models of composite wind turbine blades with shell and solid elements. *Composite Structures*, 200:521–531, 2018.

[43] S. S. Rao. *Mechanical Vibrations*. Pearson Education Limited, Six Edition in SI Units edition, 2011.

[44] J. N. Reddy. *Mechanics of Laminated Composite Plates and Shells*. CRC Press, 2004. URL `https://www.taylorfrancis.com/books/9780203502808`.

[45] K. Rohwer. Improved Transverse Shear Stiffnesses for Layered Finite Elements. Technical report, German Aerospace Center (DLR), 1988.

[46] M. Rosemeier. SMARTBLADES2: Mechanical characterization of UD glass fiber reinforced epoxy. Technical report, Fraunhofer Institute for Wind Energy and Energy System Technology IWES, 2017.

[47] *Technisches Datenblatt B-E-840g/m²-1270mm*. SAERTEX GmbH & Co. KG, 2015.

[48] *Technisches Datenblatt U-E-1182g/m²-1270mm*. SAERTEX GmbH & Co. KG, 2015.

[49] *Technisches Datenblatt X-E-810g/m²-1270mm*. SAERTEX GmbH & Co. KG, 2015.

[50] *Technisches Datenblatt Y-E-1199g/m²-1270mm*. SAERTEX GmbH & Co. KG, 2015.

[51] *Sikadur WTG-1280 Data Sheet*. Sika Schweiz AG, 2013.

[52] H. Söker. Loads on wind turbine blades. In *Advances in Wind Turbine Blade Design and Materials*, pages 29–58. Woodhead Publishing Series in Energy, 2013.

[53] E. E. Theotokoglou and T. Moan. Experimental and numerical study of composite T-joints. *Journal of Composite Materials*, 30(2):190–209, 1996.

[54] S. Vlachoutsis. Shear correction factors for plates and shells. *International Journal for Numerical Methods in Engineering*, 33(7):1537–1552, 1992. URL `http://doi.wiley.com/10.1002/nme.1620330712`.

[55] Y. Wang and C. Soutis. A Finite Element and Experimental Analysis of Composite T-Joints Used in Wind Turbine Blades. *Applied Composite Materials*, 25:953–964, 2018.

[56] C. Willberg, R. Ravi, J. Rieke, and F. Heinecke. Validation of a 20 m Wind Turbine Blade Model. *Energies*, 14(9), 2021.

[57] J. A. Wolf. The influence of mounting stiffness on frequencies measured in a vibration test. Technical report, SAE Technical Papers, 1984.

[58] Y. Zuo, J. Montesano, and C. V. Singh. Assessing progressive failure in long wind turbine blades under quasi-static and cyclic loads. *Renewable energy*, 119:754–766, 2018.